PROCEEDINGS

MMM 2008

Fourth International Conference

MULTISCALE MATERIALS MODELING

OCTOBER 27-31, 2008 ▪ TALLAHASSEE, FLORIDA, USA

Tackling Materials Complexities via Computational Science

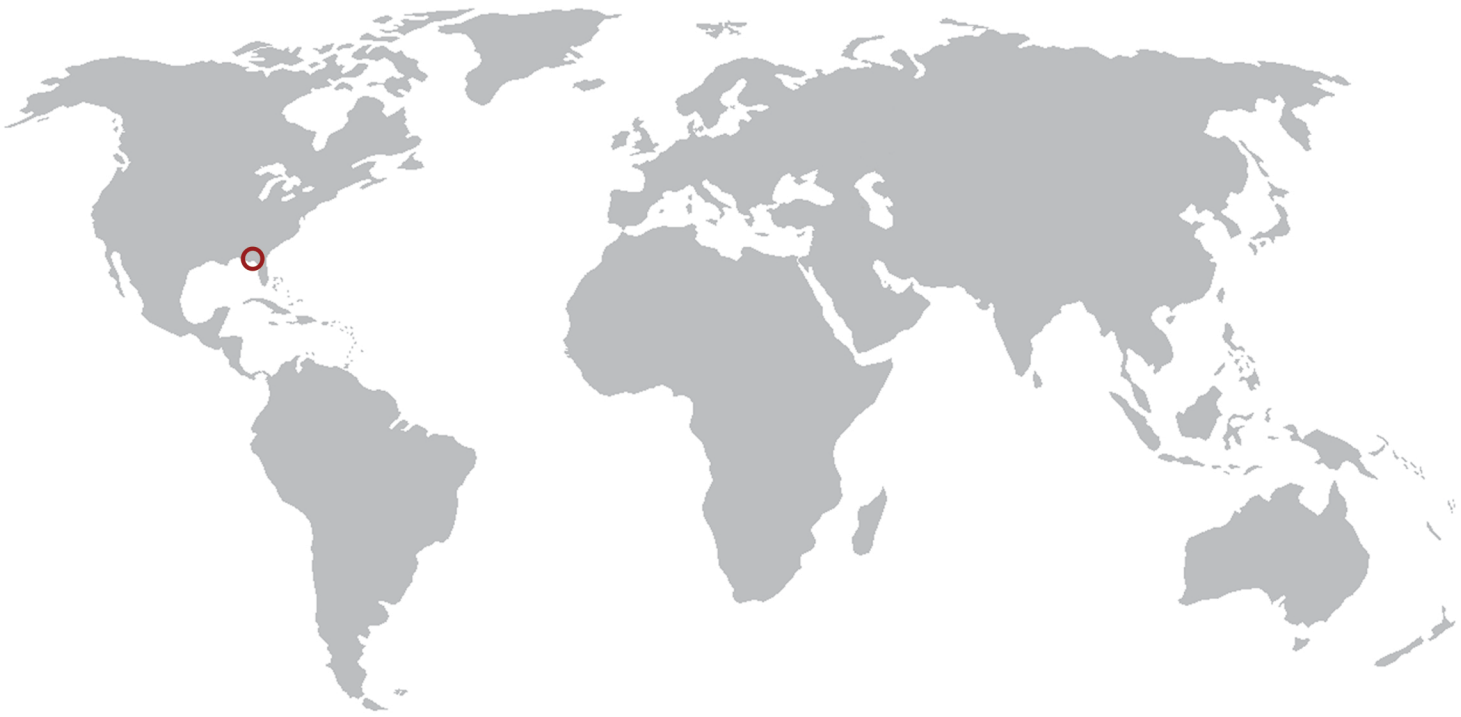

Hosted by the Department of Scientific Computing and Florida State University

DEPARTMENT OF Scientific COMPUTING

FLORIDA STATE UNIVERSITY 1851 VIRES ARTES MORES

Proceedings of

MMM 2008
Fourth International Conference
MULTISCALE MATERIALS MODELING
OCTOBER 27-31, 2008 ▪ TALLAHASSEE, FLORIDA, USA

Anter El-Azab
Editor

Organized and Hosted by
The Department of Scientific Computing and
Florida State University

DEPARTMENT OF Scientific COMPUTING

Papers published in this volume constitute the proceedings of the Fourth International Conference on Multiscale Materials Modeling (MMM-2008). Papers were selected by the program committee for oral or poster presentation. They are published as submitted, in the interest of timely dissemination.

ISBN 978-0-615-24781-6

Department of Scientific Computing
Florida State University
400 Dirac Science Library
P.O. Box 3064120
Tallahassee, FL 32306-4120

Printed in the United States of America

Forward

The field of multiscale modeling of materials promotes the development of predictive materials research tools that can be used to understand the structure and properties of materials at all scales and help us process materials with novel properties. By its very nature, this field transcends the boundaries between materials science, mechanics, and physics and chemistry of materials. The increasing interest in this field by mathematicians and computational scientists is creating opportunities for solving computational problems in the field with unprecedented levels of rigor and accuracy. Because it is a part of the wider field of materials science, multiscale materials research is intimately linked with experiments and, together, these methodologies serve the dual role of enhancing our fundamental understanding of materials and enabling materials design for improved performance.

The increasing role of multiscale modeling in materials research motivated the materials science community to start the Multiscale Materials Modeling (MMM) Conference series in 2002, with the goal of promoting new concepts in the field and fostering technical exchange within the community. Three successful conferences in this series have been already held:

- The First International Conference on Multiscale Materials Modeling (MMM-2002) at Queen Mary University of London, UK, June 17-20, 2002,
- Second International Conference on Multiscale Materials Modeling (MMM-2004) at the University of California in Los Angeles, USA, October 11-15, 2004, and
- Third International Conference on Multiscale Materials Modeling (MMM-2006) at the University of Freiburg, Germany, September 18-22, 2006.

The Fourth International Conference on Multiscale Materials Modeling (MMM-2008) held at Florida State University comes at a time when the wider computational science field is shaping up and the synergy between the materials modeling community and computational scientists and mathematicians is becoming significant. The overarching theme of the MMM-2008 conference is thus chosen to be "*Tackling Materials Complexities via Computational Science*," a theme that highlights the connection between multiscale materials modeling and the wider computational science field and also reflects the level of maturity that the field of multiscale materials research has come to. The conference covers topics ranging from basic multiscale modeling principles all the way to computational materials design. Nine symposia have been organized, which span the following topical areas:

- Mathematical basis for multiscale modeling of materials
- Statistical frameworks for multiscale materials modeling
- Mechanics of materials across time and length scales
- Multiscale modeling of microstructure evolution in materials
- Defects in materials
- Computational materials design based on multiscale and multi-level modeling principles

- Multiscale modeling of radiation effects in materials and materials response under extreme conditions
- Multiscale modeling of bio and soft matter systems

The first five topical areas are intended to cover the theoretical and computational basis for multiscale modeling of materials. The sixth topical area is intended to demonstrate the technological importance and industrial potential of multiscale materials modeling techniques, and to stimulate academia-laboratory-industrial interactions. The last two topical areas highly overlap with the earlier ones, yet they bring to the conference distinct materials phenomena and modeling problems and approaches with unique multiscale modeling aspects.

This conference would not have been possible without the help of many individuals both at Florida State University and around the world. Of those, I would like to thank the organizing team of MMM-2006, especially Professor Peter Gumbsch, for sharing their experience and much organizational material with us. I also thank all members of the International Advisory Board for their support and insight during the early organizational phase of the conference, and the members of the International Organizing Committee for the hard work in pulling the conference symposia together and for putting up with the many organization-related requests. Thanks are due to Professor Max Gunzburger, Chairman of the Department of Scientific Computing (formerly School of Computational Science) and to Florida State University for making available financial, logistical and administrative support without which the MMM-2008 would not have been possible. The following local organizing team members have devoted significant effort and time to MMM-2008 organization: Bill Burgess, Anne Johnson, Michele Locke, Jim Wilgenbusch, Christopher Cprek and Michael McDonald. Thanks are also due to my students Srujan Rokkam, Steve Henke, Jie Deng, Santosh Dubey, Mamdouh Mohamed and Jennifer Murray for helping with various organizational tasks. Special thanks are due to Bill Burgess and Srujan Rokkam for their hard work on the preparation of the proceedings volume and conference program.

I would like to thank the MMM-2008 sponsors: Lawrence Livermore National Laboratory (Dr. Tomas Diaz de la Rubia), Oak Ridge National Laboratory (Dr. Steve Zinkle) and Army Research Office (Drs. Bruce LaMattina and A.M. Rajendran) for the generous financial support, and thank TMS (Dr. Todd Osman) for the sponsorship of MMM-2008 and for advertising the conference through the TMS website and other TMS forums.

I would also like to thank all plenary speakers and panelists for accepting our invitation to give plenary lectures and/or serve on the conference panels. Lastly, I would like to thank the session chairs for managing the conference sessions.

Anter El-Azab
Conference Chair

International Advisory Board

Dr. Tomas Diaz de la Rubia	LLNL, USA
Prof. Peter Gumbsch	Fraunhofer Institute IWM, Freiburg, Germany
Dr. A.M. Rajendran	ARO, USA
Dr. Steve Zinkle	ORNL, USA
Prof. Anter El-Azab	FSU, USA
Prof. Michael Zaiser	Edinburgh, UK
Prof. Xiao Guo	Queens, London, UK
Prof. Shuichi Iwata	University of Tokyo, Japan
Prof. Jan Kratochvil	CTU, Prague, Czech Republic
Prof. Nasr Ghoniem (Chair)	UCLA, USA
Dr. Ladislas Kubin	ONERA-LEM, France
Prof. Shaker Meguid	Toronto, Canada
Prof. Alan Needleman	Brown, USA
Prof. Michael Ortiz	Caltech, USA
Prof. David Pettifor	Oxford, UK
Prof. Robert Phillips	Caltech, USA
Prof. Dierk Raabe	Max Planck Institute, Duesseldorf, Germany
Prof. Yoji Shibutani	Osaka University, Japan
Prof. Subra Suresh	MIT, Massachusetts USA
Prof. Yoshihiro Tomita	Kobe University, Japan
Prof. Erik Van der Giessen	University of Groningen, The Netherlands
Dr. Dieter Wolf	INL, USA
Prof. Sidney Yip	MIT, USA
Prof. David Bacon	Liverpool, UK
Dr. Michael Baskes	LANL, USA
Prof. Esteban Busso	Ecole des Mines, France
Prof. Timothy Cale	RPI, New York, USA
Dr. Moe Khaleel	PNNL, USA
Prof. David Srolovitz	Yeshiva, USA
Prof. Emily Carter	Priceton University, USA
Dr. Dennis Dimiduk	AFRL, USA
Prof. Rich Le Sar	Iowa State University, USA

International Organizing Committee

Weinan E	Princeton University, USA
Max Gunzburger	Florida State University, USA
Mitchell Luskin	University of Minnesota, USA
Rich Lehoucq	Sandia National Laboratories, USA
A.M. Rajendran	U.S. Army Research Office, USA
Stefano Zapperi	University of Rome, Italy
M.-Carmen Miguel	University of Barcelona, Spain
Mikko Alava	Helsinki University of Technology, Finland
Istevan Groma	Eötvös University, Hungary
Tom Arsenlis	Lawrence Livermore National Laboratory, USA
Peter Chung	Army Research Laboratory, USA

Marc Geers	Eindhoven University of Technology, The Netherlands
Yoji Shibutani	Osaka University, Japan
Dieter Wolf	Idaho National Laboratory, USA
Jeff Simmons	Air Force Research Laboratory, USA
Simon Phillpot	University of Florida, USA
Anter El-Azab (Chair)	Florida State University, USA
Daniel Weygand	University of Karlsruhe (TH), Germany
Zi-Kui Liu	Pennsylvania State University, USA
Hamid Garmestani	Georgia Institute of Technology, USA
Moe Khaleel	Pcific Northwest National Laboratory, USA
Mei Li	Ford Motor Company, USA
Fie Gao	Pacific Northwest National Laboratory, USA
Roger Stoller	Oak Ridge National Laboratory, USA
Pascal Bellon	University of Illinois, Urbana-Champaign, USA
Syo Matsumura	Kyushu University, Japan
Jeffery G. Saven	University of Pennsylvania, USA
Wei Yang	Florida State University, USA
T.P. Straatsma	Pacific Northwest National Laboratory, USA
L.P. Kubin	CNRS-ONERA, France
S.J. Zinkle	Oak Ridge National Laboratory, USA
Jaafar El-Awady	University of California, Los Angeles, USA
Shahram Sharafat	University of California, Los Angeles, USA
Hanchen Huang	Rensselaer Polytechnic Institute, USA
Yury N. Osetskiy	Oak Ridge National Laboratory, USA
Ron O. Scattergood	North Carolina State University, USA
Anna M. Serra	Universitat Politecnica de Catalunya, Spain

Local Organizing Committee (Florida State University, USA)

Prof. Anter El-Azab (Chair)
Prof. Max Gunzburger (Co-Chair)
Anne Johnson (Public relations and marketing)
Bill Burgers (Graphics and publications)
Srujan Rokkam (Proceedings and printing)
Michael McDonald (Webmaster)
Michele Locke (Finances)

Sponsors

Special thanks to the following sponsors:

- The Army Research Office
- Lawrence Livermore National Laboratory
- Oak Ridge National Laboratory

for their generous financial support, and to

- The Minerals, Metals & Materials Society (TMS)

for the sponsoring and advertising the conference through the TMS website.

Contents

Symposium 5

Symposium 5

Computational materials design

Multiscale Modeling of the Influence of Fe Content in a W319 Alloy on the Distribution of Intermetallic Phases and Micropores

Junsheng Wang[1], Mei Li[2], John Allison[2], Peter D. Lee[1*]
[1]Department of Materials, Imperial College London, South Kensington Campus, Prince Consort Road, London SW7 2AZ, UK (E-mail: p.d.lee@imperial.ac.uk)
[2]Materials Research and Advanced Engineering Department, Ford Research Laboratory, Dearborn, MI 48121-2053, US (E-mail: mli9@ford.com)

Keywords: Model, Intermetallics, Porosity, Aluminum Alloys, Casting, Tomography.

ABSTRACT

A multiscale model was developed to simulate the formation of Fe-rich intermetallics and pores. The microscale model is based on solving multicomponent diffusion equations *via* the finite difference method. The anisotropy of Fe-rich intermetallics was implemented *via* several different algorithms, ranging from phase field method to fast robust decentred octahedron/needle techniques. The macroscale temperature and pressure distributions of a laboratory wedge casting were calculated using a commercial finite element package. They were then interpreted onto a regular rectangle grid used in the micro-model, allowing the prediction of both gas porosity and shrinkage driven porosity. This allows the influence of varying casting conditions on the Fe-rich intermetallics, the pores, and their interactions to be predicted. The simulated complex morphology of Fe-rich intermetallic particle is found to have large influence on the nucleation and growth of pores. By increasing the solidification time, more needle-like β Fe-rich intermetallics are formed, which both facilitates pores to nucleate and affects pore morphology. The influence of Fe content on the formation of both α and β Fe-rich intermetallics was simulated and compared to synchrotron x-ray tomography experiments. Through coupling the microscale to macroscale models, the influence of Fe content and processing conditions on the final distribution of pores in complex shape castings can be predicted.

1. Introduction

Primary aluminium has been increasingly used in the automotive industry in recent years to reduce the weight and thus energy-consumption. For instance, many car manufacturers have replaced steel with 319-type alloys on engine block castings (e.g. *Ford V8*). However, the environmental cost of producing aluminium is 20 times higher than recycling secondary alloys (e.g. W319) [1]. The technical barrier, which prevents the foundry manufacturers from using the recycled aluminium alloys, is that impurity iron exists in those metals almost inevitably and degrades the mechanical properties of casting products by forming highly faceted plate-like intermetallics.

In order to improve the fatigue life, ductility, shock resistance, and machinability of secondary aluminium castings, two of the most important microstructure features, namely Fe-rich intermetallics and porosity, have to be controlled. This can be done by optimizing casting conditions and/or diluting iron concentration. Multiscale modeling, includes the complex physics of solidification over a wide range of spatial, temporal and energy scales, providing a powerful methodology to perform virtual aluminium casting (*VAC*) [2], and giving a number of optimized technical solutions to improving the performance of casting components while minimizing the total cost effectively.

In this paper, a multiscale model was developed to predict the shape, size, and distribution of Fe-rich intermetallics and pores together with columnar/equiaxed dendritic structures around which they form. This model was combined with a thermodynamic database for Gibbs energy calculation and coupled to a macroscale fluid flow model for pressure calculation. The resulting 3D predictions were validated qualitatively and quantitatively by comparison to high resolution synchrotron x-ray tomography analysis of a laboratory casting. Good agreements between numerical and experimental results were found, clarifying, under some conditions, the mechanisms controlling the formation of both Fe-rich intermetallics and pores and the promising benefit of applying this model to industrial scale castings.

2. Experiments

A wedge was cast from a 319-type alloy (Al-7.5 wt.%Si-3.5wt.%Cu-0.8 wt.%Fe). The SEM characterizations and EDX measurements were performed on two samples obtained from two locations at the middle of the wedge in width, and 35mm and 100 mm from the bottom chill in height respectively. Two cylindrical samples, 2 mm in diameter, were analyzed in the same locations using synchrotron x-ray tomography. The tomography experiments were carried out at the micro focusing and imaging beam line ID19 at the European Synchrotron Radiation Facility (*ESRF*). Monochromatic beam provided parallel x-ray energy of 34*KeV*, which transmitted through each cylindrical sample at different angles as the sample rotated 180° to project 900 high resolution images (1.4μm/*voxel*). Using these high contrast and signal-to- noise ratio images, a volume consisting of 1700×1700×371 voxel was reconstructed. After ring artifact removal using RingCorrection *v*0.21 provided by *ESRF*[1], a sub volume of 300×300×300 voxel was chopped and filtered by edge-preserving smoothing algorithm in ImageJ[2]. The segmented 3D morphology of Fe-rich intermetallics were then quantified and visualized using commercial tools [3, 4].

3. Mathematical Model

Primary phase & Fe-rich intermetallic model

The mathematical model developed in this paper includes a kinetic model for grain nucleation and growth, and a thermodynamic model for chemical potential calculations. They are combined through Gibbs free energy which is the driving force for grain growth in each cell. The spatial distribution of solute species on a uniform grid in a multicomponent system is calculated by solving Fick's second law using a finite difference technique. Preferential growth of primary phase in multicomponent was simulated by employing a decentred square/octahedron algorithm similar to prior works [3]. A novel approach of combining Monte Carlo (MC) and decentred needle/plate algorithms was developed to take into account the anisotropies of secondary phases similar to prior publications [4, 5]. Therefore, liquid transforms into either secondary solid phases (α/β-Fe-rich intermetallics) depending on the overall free energy (E_T):

$$E_T > E_A - E_\theta \quad , \quad E_\theta = \langle J_\theta \rangle_x + \langle J_\theta \rangle_y + \langle J_\theta \rangle_z \tag{1}$$

[1] European Synchrotron Radiation Facility, Grenoble Cedex, France
[2] ImageJ, National Institutes of Health, USA
[3] VgStudioMax, Volume Graphics GmbH Wieblinger Weg 92a 69123 Heidelberg Germany
[4] Amira, Mercury Computer Systems SAS F-33708 Merignac Cedex France

where E_A is the activation energy, and E_θ is the summary of interfacial energy flux terms from different faces $<J_\theta>_x$, $<J_\theta>_y$, and $<J_\theta>_z$.

The velocity of solidification is proportional to probability functions due to forward and backward atomic jumps [6]:

$$u(\Delta E_A, \Delta E_T) = u_0 \exp\left(-\frac{\Delta E_A}{RT}\right)\left[1 - \exp\left(-\frac{\Delta E_T}{RT}\right)\right] \quad (2)$$

where u_0 is the kinetic coefficient of solidification which is a function of the effective diffusion coefficient (D_e), the atomic diffusion length (λ), and the fraction of sites (v_s) which is a dynamic parameter determined by local orderings and crystal structures [7]. For 3D simulation, we adopted values ranging from $(1/4)^3$ to $(1/2)^3$ for Fe-rich intermetallic phases which grow either Monoclinic or BCC crystal structure.

Porosity model

The porosity models previously developed by Lee and Hunt [8] and Atwood and Lee [9] for binary alloys were enhanced to include the effect of multicomponent on the solubility of hydrogen in the liquid (S_l), given as [10, 11]:

$$\log S_l = -2760/T - 0.0119C_{Si} - 0.0269C_{Cu} \text{ (ml STP/100g)} \quad (1)$$

The effect of Fe-rich intermetallic on pore formation was implemented in two different ways: I. the fraction of Fe-rich intermetallics in each cell reduces the effective diffusion coefficient of hydrogen linearly; II. the presence of Fe-rich intermetallics lead to a lower value of *G/S* interfacial energy and thus facilitate the nucleation and growth of pores.

Coupling micromodel to macromodel

As reported previously [12], the entire microstructural model was implemented as a subroutine in *ProCast*[5], which was used to calculate the local pressure and temperature in the liquid, allowing both shrinkage and gas effects to be simultaneously solved, including the interaction with the developing multi-phase solid. Therefore, various phenomena occurring in different scales are incorporated in the current model ranging from Fe-rich intermetallic, pore and grain formation in meso-scale to heat transfer and fluid flow in macro-scale.

Simulation Methods

Two domain sizes were used for the simulations: cubes of 0.8 mm on each side, and cuboids of 0.2mm×0.4mm×0.8mm with a cell size of 12.5 μm. Statistical analysis was performed on the results from the former larger domain and several runs were done in the latter smaller domain for qualitative comparison. The initial hydrogen concentration of 0.24 ml/100g STP was used throughout the simulations while the Fe content changes from 0.2 to 0.8 wt.% in different simulations.

4. Results & Discussion

SEM/EDX characterization of Fe-rich intermetallics

As it is revealed by the SEM image in Fig. 1 (a), a plate is situated on the top of a large pore and bended during polishing to expose the internal body of this pore. The composition of this plate phase was determined by EDX measurement on a square

[5] ESI Group, Paris

region of the plate (spectrum 1). As shown in Fig. 1 (b), this plate correspond to the β-Al_5FeSi Fe-rich intermetallic phase. This finding agrees with many other authors' report which documents the possible influence of needle/plate-like Fe-rich intermetallics on the formation of pores [13]. However, the lack of qualitative 3D metallographs of plate-like Fe-rich intermetallics and explicit predictions left various hypotheses undetermined.

Comparison of synchrotron x-ray tomography with the micromodel predictions

The synchrotron x-ray tomography dataset, shown in Fig. 2 (a), was chopped into a cube with edge size of 420μm. Using level-set method, the Fe-rich intermetallics in this subvolume was then extracted slice by slice. Therefore, the final 3D morphology of plate-like Fe-rich intermetallics was successfully obtained, as shown in Fig. 2 (b). Due to the thin nature of this phase and inevitable noises in tomography scans, the real smooth surface of plates was not maintained during segmentation. However, it still provides qualitative results for 3D model validations as it is the first non-destructive discovery of plate-like Fe-rich intermetallics.

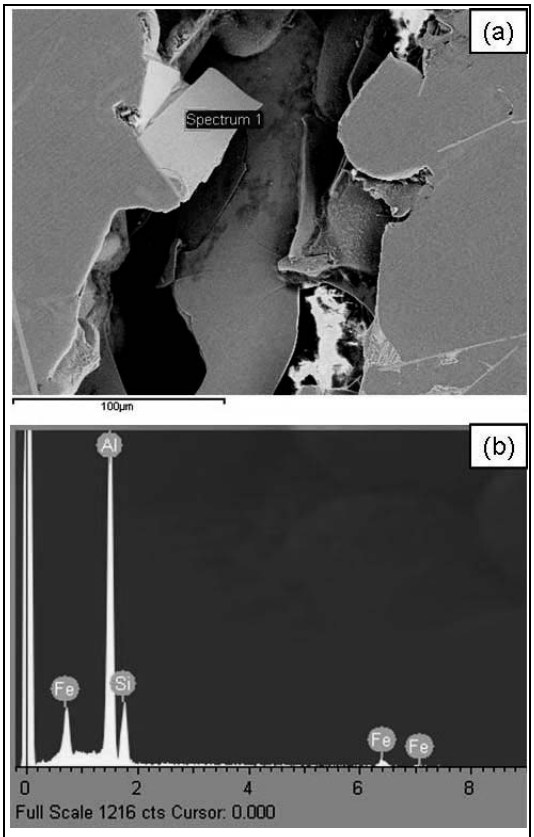

Fig. 1. (a) SEM image showing a large pore surrounded by plate-like Fe-rich intermetallics, and (b) EDX energy spectrum of the plate-like Fe-rich intermetallic phase from a wedge casting.

A simulation was performed in a cube domain with edge size of 0.8mm. The grain nucleation density was 100 mm^{-3} and the undercooling was 0.5±0.25°C. Fig. 2 (c) shows the simulated grain structure in a multicomponent Al-7.5wt.%Si-3.5wt.%Cu-0.8wt.%Fe alloy under a cooling rate of 3.5°C/s. The resulting plate-like Fe-rich intermetallics is shown in Fig. 2 (d). During solidification solute Fe keeps segregating into the interdendritic region before it freezes down to 570°C and fraction solid reaches 0.4. When the local concentrations of both Fe and Si become such a supersaturated state that produce higher total free energy for liquid to Fe-rich intermetallic transformation comparing with the activation energy, nucleation of intermetallic happens. The same nucleation density as primary phase was used in Fe-rich intermetallic nucleation. However, the relative energy barrier was kept at 2.5±0.25, allowing the nucleation occurs from the middle (570°C) until the end of solidification (510°C). This results in ~4% of this phase in total volume fraction and 20 mm^{-3} in number density similar to experimental values (~4.2%, and 40 mm^{-3} respectively). Although the domain size is smaller in experiments comparing with

simulations, the final plate-like morphology of Fe-rich intermetallic is comparable with experiments as seen in Fig. 2 (b) and (d).

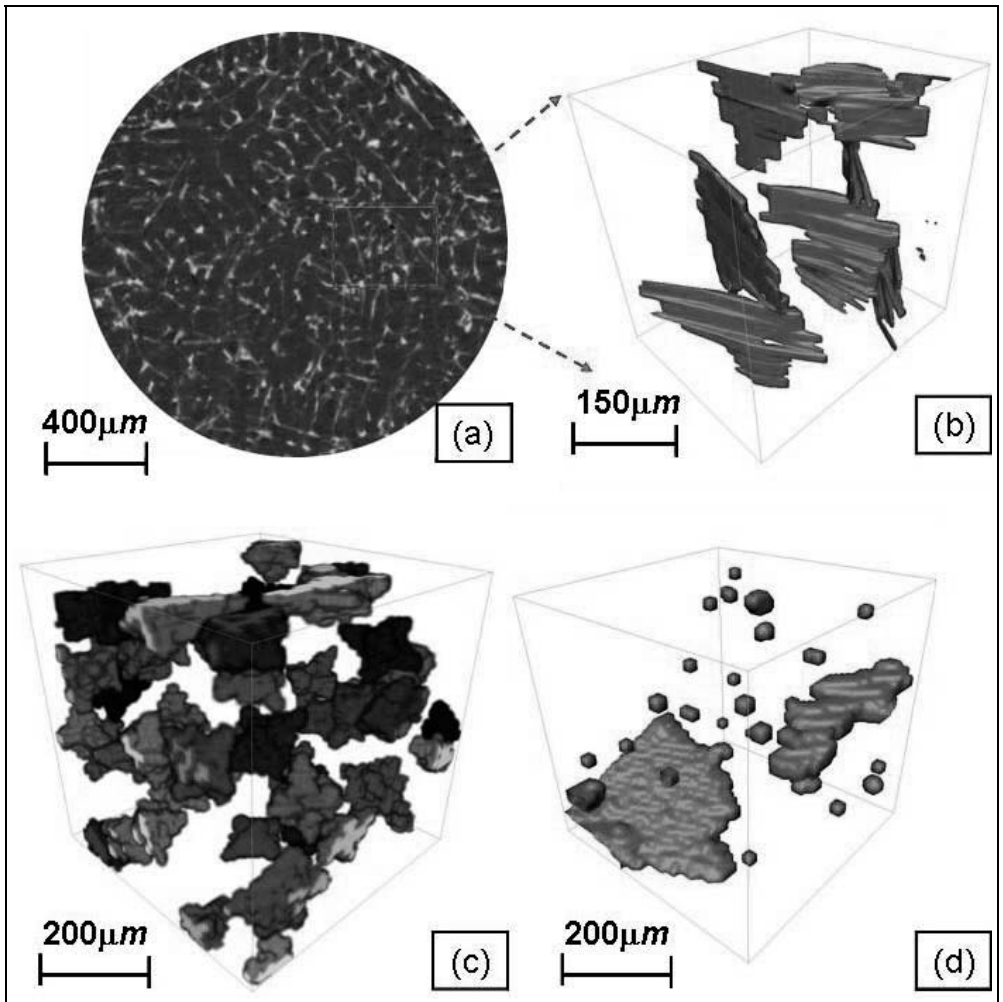

Fig. 2. Comparison of tomography experiments and simulations in an Al-7.5Si-3.5Cu-0.8Fe alloy: (a) an orthoslice of 3D tomography data set; (b) segment 3D Fe-rich intermetallic morphology from CT data; (c) simulated dendritic structure; (d) simulated plate-like Fe-rich intermetallics.

Influence of cooling conditions on microstructure formation

Using the same conditions as our laboratory sand mould wedge castings, a virtual casting was performed in the macromodel (*Procast2006*) by maintaining the same length scale and choosing the same materials properties and casting conditions. The simulated solidification time is shown by different contour levels in Fig. 3. (a). The temperature and pressure evolution at two different locations (35mm, and 100mm from the copper chill) is plotted in Fig. 3. (b). Shorter solidification time and sharper drops of both temperature and pressure are seen as the location moves closer to the relatively narrow end of the wedge where copper chill is located. The information in these two nodes has been directly used by the micromodel during solidification to calculate the local undercooling and pressure drop, which drives grain formation and pore growth. Fig. 3. (c-d) shows the predicted grain structure in different colors and

pores in green. Fe-rich intermetallic is shown in red. Comparing Fig. 3. (c) with (d), significant difference in both pore size and Fe-rich intermetallic size can be seen at different casting conditions. As the solidification time increases, larger intermetallic phases can form which promote the formation of tortuous pores by reducing hydrogen diffusivity and decrease the interfacial energy. Shorter solidification time, however, leads to their nucleation in separate fashion because of limited time for diffusion of hydrogen atoms leading to local segregation of them.

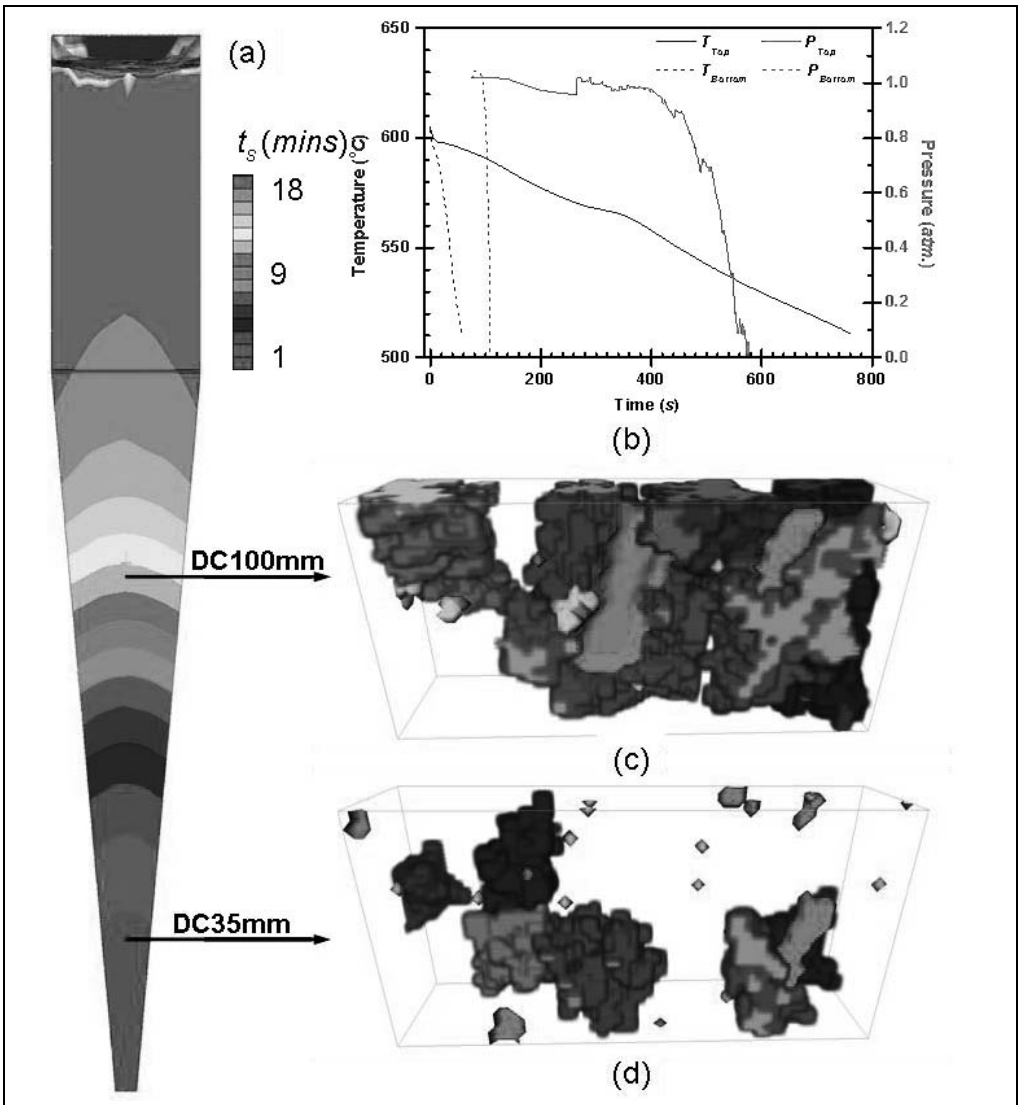

Fig. 3. Multiscale model predictions: (a) the solidification time of entire wedge mapped by different contour levels; (b) the temperature and pressure profile in the middle of the casting with different locations from the chill, DC=35mm and DC=100mm; (c) and (d) the grain structure (dark colors), pores (light green), and Fe-rich intermetallics (red) [12, 14].

In both cooling conditions, the coupled growth of primary dendrites and Fe-rich intermetallic is clearly seen. The restrictions of porosity growth by the dendritic

structure and Fe-rich intermetallics are also predicted. Therefore, the microstructure features can be designed *via* optimizing casting conditions for desired size of pores and Fe-rich intermetallics. This can be a critical step for the fatigue life predictions of casting components where the key input parameter is the quality of local microstructure [15].

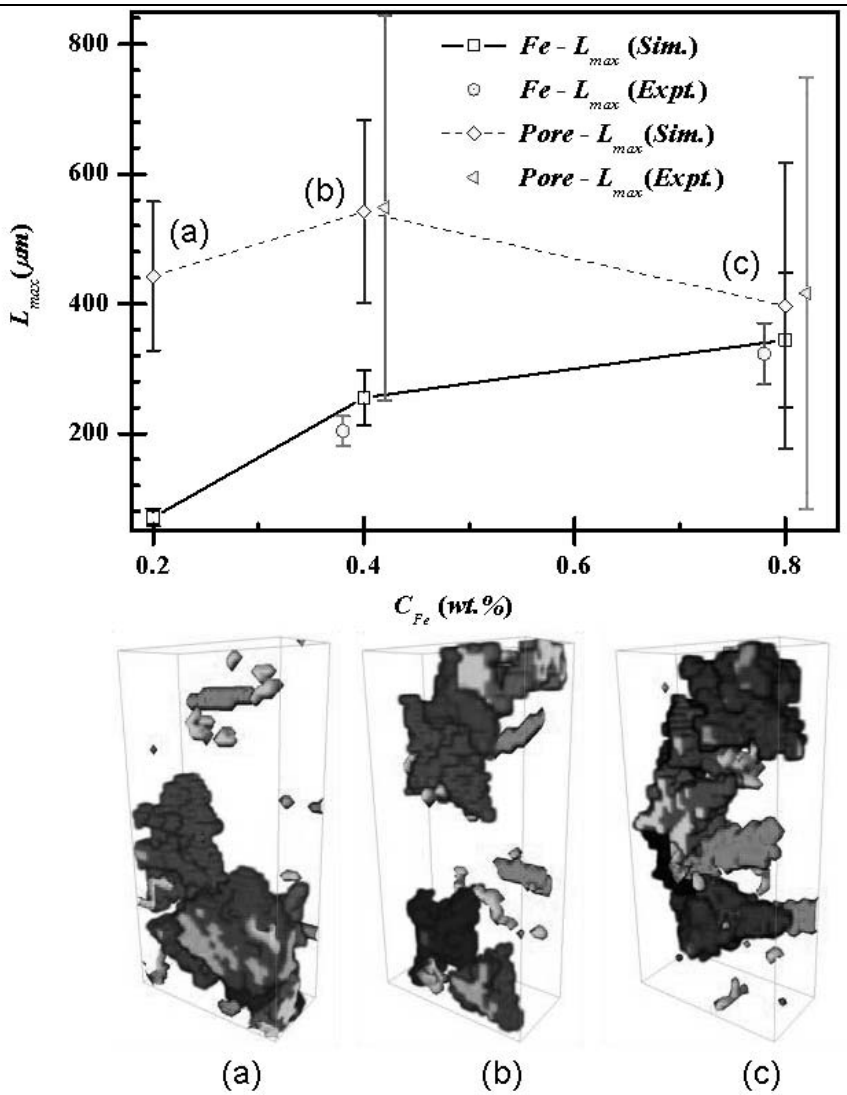

Fig. 4. Influence of Fe content on the size distribution of Fe-rich intermetallics and pores. (a) 0.2wt.%Fe, (b) 0.4wt.%Fe, (c) 0.8wt.%Fe (Note, the primary phase is rendered in different colors, pores in green and Fe-rich intermetallics in red).

Influence of Fe contents on microstructure formation

The kinetics of Fe-rich intermetallic formation can be changed by the initial Fe concentration dramatically. Therefore, simulations were done in 3 different Fe levels under the same cooling conditions (3.5°C/s). As shown in Fig 4, the Fe-rich intermetallic grows larger as Fe concentration increases from 0.2 to 0.8wt.%. However, it is not linearly increasing from 70μm to 350μm. This is probably because

Fe-rich intermetallic phases form almost at the same temperature in 0.4wt.%Fe as in 0.8wt.%Fe (570°C), while later nucleation is observed in 0.2wt.%Fe at 560°C. The segregation of Fe takes much longer in low Fe content.

Interestingly, the size of porosity does not follow the same trend of increase as the intermetallics form larger. In lower Fe content Fig 4 (a), pores tend to grow in the interdendritic regions and filling the inadequately fed spaces. Hence, Fe-rich intermetallic phases do not have much effect on pore growth, though they do promote the nucleation of small pores around it later on when some of them grow large enough. As the concentration of Fe increases form 0.2 to 0.4wt.%, large Fe-rich intermetallics form early and become large enough to slow down the effective diffusion of hydrogen and provide good subtract for pore nucleation. This results in pore size increase from $440\mu m$ to $540\mu m$ as reported by many other authors [13]. However, this influence is not maintained as higher Fe content (0.8wt.%) is used as comparing Fig 4 (b) with (c). This decrease is because the size of Fe-rich intermetallics grows as large as the primary dendrites before the nucleation of pores which leads to more hydrogen supersaturated sites in the liquid. More pores can nucleate to absorb the hydrogen locally and thus smaller pores are obtained at the end of solidification in high Fe level.

Both the size of pores and Fe-rich intermetallics were also obtained experimentally. They are slightly shifted with respect of Fe content and shown Fig 4. The simulation values agree well with experimental results at 0.4 and 0.8 wt.%Fe. A decrease of pore size is proven by experiments, when the Fe content increases from 0.4 to 0.8 wt.% although more experimental studies need to be done in order to confirm the pore and intermetallic size at 0.2wt.%Fe. Therefore, this 3D mathematical model replicates the physics of pore and Fe-rich intermetallic formation and can predict the size distribution as well as the morphology of those phases in multicomponent systems.

5. Conclusions

A multiscale model was developed to predict the formation of Fe-rich intermetallic and pores in 3D. By comparing the simulations with experiments, the following points have been successfully achieved. (1) Synchrotron X-ray tomography combined with advanced image analysis has been shown to give the 3D morphology and size of Fe-rich intermetallics. (2) The multiscale model successfully predicts the observed 3D morphology of Fe-rich intermetallics and pores qualitatively and quantitatively. (3) Good correlation between the mathematical model and experiments demonstrate that the diffusion of multicomponent and free energy of each phase determines the microstructure formation. (4) The influence of Fe-rich intermetallic on pore formation is not proportional. The model allows the prediction of large Fe-rich intermetallics and its influence on tortuous pore formation in different Fe contents.

In summary, this validated multiscale model is applicable to predict the microstructure features including Fe-rich intermetallics and pores, which can produce reliable information for fatigue life predictions. The environmentally friendly secondary aluminium alloys can be used on commercial castings if statistically optimized processing conditions are applied in industrial scale castings.

Acknowledgements

The author(s) would like to acknowledge the support from Dorothy Hodgkin Postgraduate Awards, and funding from Ford Motor Company. The authors also

acknowledge many useful discussions both with colleagues at Imperial College London and in the Ford Research Laboratory Detroit, especially Dr. Robert C. Atwood and Dr. Jake Zindel. In addition, we would like to thank the generous support from *ESI* and useful synchrotron tomography data from ESRF (Code: MA-403) and thermodynamic data from Professor Zi-Kui Liu at the Pennsylvania State University.

References

1. L. H. Van Vlack, *Elements of Materials Science and Engineering*. 1989, London: Prentice Hall.
2. John Allison, Mei Li, C. Wolverton, and XuMing Su, *Virtual Aluminum Castings: An Industrial Application of ICME.* JOM, 2006: p. 28-35.
3. W. Wang, P. D. Lee, and M. McLean, *A model of solidification microstructures in nickel-based superalloys: predicting primary dendrite spacing selection.* Acta Mater., 2003. **51**(10): p. 2971-2987.
4. J. Geiger, A. Roosz, and P. Barkoczy, *Simulation of grain coarsening in two dimensions by cellular-automaton.* Acta Mater., 2001. **49**(4): p. 623-629.
5. Wei Yang, Long-Qing Chen, and Gary L. Messing, *Computer simulation of anisotropic grain growth.* Mater. Sci. Eng. A, 1995. **195**: p. 179-187.
6. D. A. Porter and K. E. Easterling, *Phase Transformations in Metals and Alloys*. Second ed. 1992, London: Chapman & Hall. 514.
7. H. Assadi and A.L. Greer, *Site-ordering effects on element partitioning during rapid solidification of alloys.* Nature, 1996. **383**(6596): p. 150-152.
8. P. D. Lee and J. D. Hunt, *Hydrogen porosity in directionally solidified aluminium-copper alloys: A mathematical model.* Acta Mater., 2001. **49**(8): p. 1383-1398.
9. R. C. Atwood and P. D. Lee, *Simulation of the three-dimensional morphology of solidification porosity in an aluminium-silicon alloy.* Acta Mater., 2003. **51**(18): p. 5447-5466.
10. C. E. Ransley and H. Neufeld, *The solubility of Hydrogen in Liquid and Solid Aluminium.* J. Inst. Met., 1948. **74**: p. 599-620.
11. D Doutre, Alcan Int. Ltd. Internal report, 1991.
12. J. S. Wang and P. D. Lee, *Simulating tortuous 3D morphology of microporosity formed during solidification of AlSiCu alloys.* Int. J. Cast. Metals Res., 2007. **20**: p. 151-158.
13. Cameron M. Dinnis, John A. Taylor, and Arne K. Dahle, *Iron-related porosity in Al-Si-(Cu) foundry alloys.* Mater. Sci. Eng. A, 2006. **425**(1-2): p. 286-296.
14. P.D. Lee, J.S. Wang, and R.C.Atwood, *Microporosity Formation during the Solidification of Aluminum-Copper Alloys.* JOMe (USA), 2006. **(Accepted)**.
15. J. Z. Yi, Y. X. Gao, P. D. Lee, H. M. Flower, and T. C. Lindley, *Scatter in fatigue life due to effects of porosity in cast A356-T6 aluminum-silicon alloys.* Metall. Mater.Trans. A, 2003. **34A**(9): p. 1879-1890.

Material Design through Multi-Scale Simulations: Aluminum Sheet Forming Using an Anisotropic Yield Function Coupled with Crystal Plasticity Theory

Raja K. Mishra[1], **Kaan Inal**[2], **Oana Cazacu**[3]

[1]**General Motor R&D Center, Warren, MI 48090, USA (raj.k.mishra@gmotors.com)**
[2]**University of Waterloo, Waterloo, Ontario, N2L 3G1, Canada, (kinal@mecheng1.uwaterloo.ca)**
[3]**University of Florida, REEF, Shalimar, FL 32579-1163, USA (cazacu@reef.ufl.edu)**

ABSTRACT

Crystal plasticity theories have become very powerful tools in materials design since these models can account for the effects of microstructure and its evolution with deformation. Numerical modeling based on crystal plasticity theories are performed at two different scales; the microscopic scale where crystal plasticity is employed to understand the deformation mechanisms and the effects of microstructure, and at the macroscopic scale in which crystal plasticity models are employed to generate input for simpler and computationally efficient macroscopic (phenomenological) models. In this paper, information which was not available through direct mechanical testing has been generated from measured initial texture and tensile data by employing a rate-dependent crystal plasticity model and Taylor theory of polycrystal plasticity. The results of the polycrystalline calculations along with experimental data have been used for the identification of the coefficients of a macroscopic anisotropic yield criterion. Illustration of this approach is provided for AA5754CC aluminum alloy. The results of the simulations are compared with each other and, for certain cases, compared with experimental data to demonstrate the strength of this multi-scale approach.

1. Introduction

A successful strategy for increased usage of light weight materials in automotive components in spite of their limitations of low formability and anisotropic yielding will involve mathematical modeling of their forming behavior under complex strain paths. The forming simulation models necessarily are macroscopic scale models that routinely use experimental input data from mechanical tests. This is changing rapidly due to new advances in multiscale modeling capabilities.

The multiscale methodology generally requires a multidisciplinary approach to probe and simulate material response with sophisticated experimental and modeling tools. Considerable progress has been made to simulate material behavior at lower length scales – at electronic, atomic and crystal level and validate them against experiments so that it can realistically aid continuum scale engineering applications. The dream to create embedded models that bring

together theory, experiment and computation to simulate material properties at multi length scales solely from atomic and electronic structure inputs and provide engineering scale solution is still distant. The hierarchical multiscale approach where output from lower length scale simulations provide input to simulations at higher length scales, especially when experimental input data is not available or hard to generate, has begun to become a reality.

The mechanical properties of a polycrystalline metal depend on many attributes of its microstructure and considerable efforts have been made in the study of micro-mechanics at this length scale to aid macroscale modeling. These microscale studies indicate that among the factors which result in plastic deformation in single crystals and polycrystals, crystallographic slip and factors that influence slip processes are most important to simulate deformation. The crystal structure and chemical composition of alloys affect critical resolved shear stresses (CRSS) to activate slip and slip induce lattice rotations. Different grains in polycrystalline materials evolve their orientations differently, resulting in a nonrandom distribution of the crystal orientations from an initial random polycrystal. Textures have profound effects on the mechanical, thermal and other physical properties of metals. Research indicates that many metal forming processes such as drawing, extrusion, rolling and sheet metal forming produce textured materials as a result of the forming processes. Plastic anisotropy due to the texture dominates deformation behaviour up to moderately large strains [1] and microscale modeling is indispensable to account for it. The microscale studies have the added advantage that they can guide material (microstructure) design for optimum performance.

The use of polycrystal plasticity theory in deformation process simulation may be viewed as an example of applying state variable models for the constitutive description of the material. The texture, together with the strengths of the slip systems, acts as a characterisation of the material state. Evolution of the state is accomplished with equations that prescribe the reorientation of crystal lattices and the changes in slip system strength induced by deformation. A link must be established between the macroscopic properties and the crystals that define the microstructure. It is the set of assumptions used in making this link that introduces many of the complexities of this approach, but provides much insight into material behaviours as well.

A constitutive model is a combination of physics and mathematics which is used to simulate material behaviour under various loading conditions. The accuracy of any constitutive model depends on the theory that it is based on. In general a model describing the constitutive behaviour of a polycrystal can be derived from single crystal deformation models which have already included microstructures, anisotropic properties of single crystals, micromechanism (slip and/or twinning mechanisms) and lattice rotation caused by slip. The point is how microstructural mechanisms of deformation operating on the single crystal level determine polycrystal behaviours, that is, how to establish a relation (realistic, physically-based assumptions) between these two kinds of models.

Advances in theory, microstructure quantification, smart algorithms, and fast computers have made it possible to perform embedded simulations at the macroscopic scale with crystal plasticity model that incorporate subscale behaviors capturing the microstructure effects. This paper presents a multi-scale methodology for developing such models that is based on crystal plasticity and continuum mechanics. After briefly presenting the crystal plasticity model and the macroscopic anisotropic yield function, an illustrative example of application of this methodology to the description of the strong anisotropy of a commercial grade continuous cast (CC) AA5754 aluminum alloy is presented.

2. Crystal Plasticity Constitutive Model

A rigorous framework for the kinematics of the finite plastic deformation of a crystal has been firmly established for some time. This basic formulation has been incorporated into a rate-dependent description of crystal plasticity constitutive relations (see [2], [3]). Within a FCC crystal, plastic deformation occurs by crystallographic slip on 12 distinct slip systems. In the rate-sensitive crystal plasticity model employed, the elastic constitutive equation for each crystal is specified by:

$$\overset{\nabla}{\boldsymbol{\sigma}} = \boldsymbol{L}\boldsymbol{D} - \dot{\boldsymbol{\sigma}}^{0} - \boldsymbol{\sigma}\mathrm{tr}\boldsymbol{D} \tag{1}$$

where $\overset{\nabla}{\boldsymbol{\sigma}}$ is the Jaumann rate of Cauchy stress, $\boldsymbol{D}$ represents the strain-rate tensor and $\boldsymbol{L}$ is the tensor of elastic moduli. The term $\dot{\boldsymbol{\sigma}}^{0}$ is a viscoplastic type stress rate that is determined by the slip rates on the 12 slip systems of a FCC crystal. The slip rates are taken to be governed by the power law expression

$$\dot{\gamma}_{(\alpha)} = \dot{\gamma}_{(0)}\,\mathrm{sgn}\tau_{(\alpha)}\left|\frac{\tau_{(\alpha)}}{g_{(\alpha)}}\right|^{1/m} \tag{2}$$

where $\dot{\gamma}_{(0)}$ is a reference shear rate taken to be the same for all the slip systems, $\tau_{(\alpha)}$ is the resolved shear stress on slip system α (α ranging from 1 to 12), $g_{(\alpha)}$ is its hardness and m is the strain-rate sensitivity index. The single slip hardening law employed in this paper takes the following power-law form:

$$h_{(\beta)} = h_0\left(\frac{h_0\gamma_\alpha}{\tau_0 n} + 1\right)^{n-1} \tag{3}$$

where h_0 is the system's initial hardening rate, n is the hardening exponent and γ_a is the accumulated slip. The response of a polycrystal comprised of many grains is obtained by invoking the Taylor assumption. Thus, at a material point representing a polycrystal of N grains, the deformation in each grain is taken to be identical to the macroscopic deformation of the continuum. Furthermore, the macroscopic values of all quantities, such as stresses, stress-rates, and elastic moduli are obtained by averaging their respective values over the total number of grains at the particular material point.

3. Orthotropic Yield Function

To describe the anisotropic plastic response of textured metals, a 3-D orthotropic yield criterion described by Plunkett Cazacu and Barlat [4] is employed. This criterion is applicable to materials that exhibit strength differential effects (e.g. Mg) as well as to materials for which there is no

noticeable difference between the behavior in tension and compression during monotonic loading. The criterion is an extension to orthotropy of the isotropic yield function

$$\Phi\left(S_1,S_2,S_3,k,a\right) = \left|S_1\right| - kS_1\Big|^a + \left|S_2\right| - kS_2\Big|^a + \left|S_3\right| - kS_3\Big|^a \tag{4}$$

where S_1, S_2, and S_3 are the principal values of the stress deviator while a and k are material parameters. For a fixed value of the degree of homogeneity a, the parameter k involved in (4) is expressible solely in terms of the ratio between the uniaxial yield in tension and the uniaxial yield in compression, respectively. Irrespective of the value of a, if the yield stresses in tension and compression are equal then $k = 0$. In particular, for $k = 0$ and $a = 2$, the yield criterion (4) reduces to the Von Mises yield criterion. Starting from the isotropic function (4), anisotropy is then introduced through two orthotropic linear fourth-order tensors $\mathbf{C}$ and $\mathbf{C}'$ operating on the Cauchy stress deviator $\mathbf{S}$. The general form of the anisotropic criterion is:

$$F\left(\boldsymbol{\Sigma},\boldsymbol{\Sigma}'\right) = \Phi\left(\Sigma_1,\Sigma_2,\Sigma_3,k,a\right) + \Phi\left(\Sigma_1',\Sigma_2',\Sigma_3',k',a\right) \tag{5}$$

In Eqn (5), k and k' are material parameters that allow for the description of strength differential effects, a is the degree of homogeneity, while $(\Sigma_1,\Sigma_2,\Sigma_3)$ and $(\Sigma_1',\Sigma_2',\Sigma_3')$ are the principal values of the transformed tensor $\boldsymbol{\Sigma} = \mathbf{C}:\mathbf{S}$ and $\boldsymbol{\Sigma}' = \mathbf{C}':\mathbf{S}$. Thus, for full 3-D stress conditions, the orthotropic criterion (5) involves 18 anisotropy coefficients. When both tensors $\mathbf{C}$ and $\mathbf{C}'$ are equal to the 4th order identity tensor and $k = k'$, the yield function (5) reduces to the isotropic yield function (4). If the yield in tension is equal to the yield in compression, the parameters k and k' associated with strength differential effects are automatically zero.

4. Application of the Proposed Methodology to AA5754 Aluminium Alloy

In this section, we present the application of the proposed methodology to the description of the anisotropy in tension of commercial grade continuous cast (CC) AA5754 aluminum sheets. The initial texture for this alloy is shown in Fig. 1, where RD and TD correspond to the rolling and transverse direction of the sheet respectively. Uniaxial tensile tests were conducted along seven

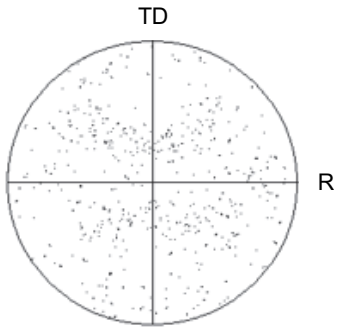

Figure 1. Initial texture represented by {111} stereographic pole figure

orientations in the plane of the sheet (i.e. from rolling to transverse directions in 15° increments). Both tensile yield tresses and Lanckford coefficients were measured. The parameters involved in the crystal plasticity model were obtained by fitting the uniaxial stress−strain curve along RD obtained by crystal plasticity to the uniaxial stress−strain curve measured experimentally using the single slip hardening law discussed above. For this material $\dot{\gamma}_0 = 0.001\text{s}^{-1}$, m = 0.002, $h_0 / \tau_0 = 20$, $\tau_0 = 38$ MPa, n = 0.31 and q = 1. Further, numerical simulations of uniaxial tension and simple shear were performed with the crystal plasticity model. For uniaxial tension simulations, the initial texture was rotated so that the stress-strain curves were predicted at orientations 0^o, 45^0 and 90^0 to the RD. For simple shear simulations, shearing within the RD-TD and RD-ND planes were considered. It should be mentioned that, homogeneous deformation was considered in all the crystal plasticity simulations since the main goal was to generate material data for the analytic yield function (5).

Next, using the experimental in-plane flow stresses and r-values, and out-of-plane data obtained with the crystal plasticity model, the coefficients involved in the analytic yield function (5) were determined by minimization of an error function. Fig. 2 shows the theoretical variation of the strain ratios and yield stresses obtained using the yield function (5) with this set of coefficients (solid line). The r-values and flow stress values at 0^o, 45^0 and 90^0 (purple symbols) obtained with the crystal plasticity model and, the results from the mechanical tests (diamonds) are also plotted in the same figure for comparison. The very good agreement between the theoretical and experimental results shows the accuracy and efficacy of the proposed methodology.

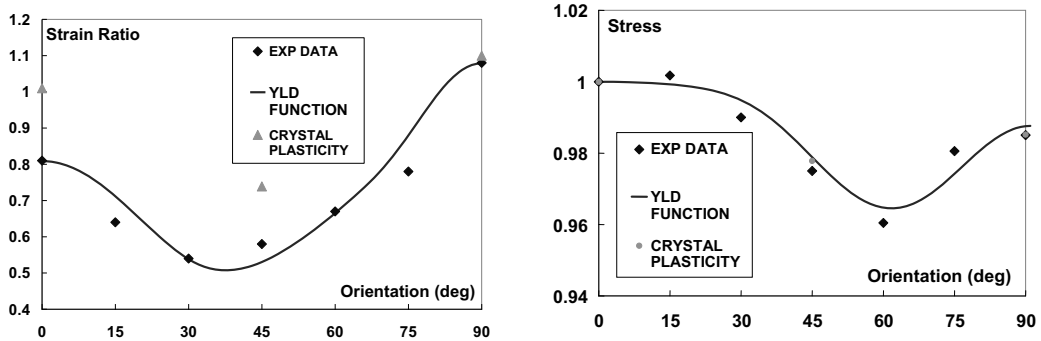

(a) (b)

Figure 2. (a) Anisotropy of the Lankford coefficients and flow stresses (b) according to the crystal plasticity model, yield function (5) and experimental data.

It must be emphasized that it is essential to identify the shear components of the linear transformation tensors **C** and **C**' in order to describe with accuracy the strong anisotropy in r-values and flow stresses simultaneously. The values of these coefficients can be obtained only based on out-of-plane flow data (see [4]). Crystal plasticity simulations are thus essential, since out-of-plane shear data is not readily accessible through direct testing.

Acknowledgements

Financial support provided by **General Motor R&D Center** is gratefully acknowledged.

References

[1] Kocks, U. F., Tom´e, C. N., Wenk, H. R., Mecking, h., 2001. *Texture and Anisotropy,* Cambridge University Press.
[2] Asaro, R.J., Needleman, A., 1985. Texture development and strain hardening in rate dependent polycrystals. Acta Metallurgica 33, 923-953.
[3] Inal, K., Wu, P. D., Neale, K. W., 2002. Instability and localized deformation in polycrystalline solids under plane strain tension. International Journal of Solids and Structures, 39, 983-1002.
[4] B. Plunkett, O. Cazacu and F. Barlat, "Orthotropic yield criteria for description of the anisotropy in tension and compression of sheet metals" Int. J. Plasticity, **24**, 847 (2008).

Computational Design of Magnesium Alloys for Improved Deformability

Young-Min Kim, Byeong-Joo Lee

Department of Materials Science and Engineering,
Pohang University of Science and Technology, Pohang 790-784, Korea
(E-mails: ymfrog@postech.ac.kr , calphad@postech.ac.kr)

ABSTRACT

The possibility of improving formability of magnesium alloys by changing the *c*/*a* ratio through the addition of alloying elements has been examined by computing the critical resolved shear stress (CRSS) for basal and non-basal slip systems. As the alloying elements, Al and Li were selected since they change the *c*/*a* ratio of Mg into the opposite directions. As the method to compute the CRSS, a molecular dynamics simulation based on the modified embedded-atom method (MEAM) interatomic potentials was used. Fundamental information for the design of magnesium alloys for improved deformability could be obtained.

1. Introduction

Magnesium alloys have a great potential as structural components due to their light-weight, excellent recycle-ability, high specific strength and damping characteristics. However, the poor ductility at room temperature gives a limitation to the wide application. The poor formability of magnesium alloys originates from the limited slip system. Since the slip system of hcp structures is believed to be related with the *c*/*a* ratio, besides the high temperature deformation to activate non-basal slip systems, changing the *c*/*a* ratio by addition of alloying elements can be considered as a means to improve the formability. The purpose of this work is to investigate the possibility of improving formability of magnesium alloys by changing the *c*/*a* ratio through the addition of alloying elements and by computing the CRSS for basal and non-basal slip systems. As the alloying elements, Al and Li were selected because it was reported experimentally that Al raises and Li reduces the *c*/*a* ratio of Mg. MEAM potentials for pure Mg, Li and Mg-Al, Mg-Li alloys were developed and the CRSSs for basal and non-basal slip systems were calculated by using a molecular dynamics simulation. Based on the simulation results, the direction of alloy design of magnesium alloys for improved deformability could be proposed.

2. Simulation Methods

2.1 Interatomic potential

To obtain physically meaningful results from atomistic simulations based on (semi-) empirical interatomic potentials, the interatomic potential should be able to reproduce various physical properties of relevant elements and alloys. Moreover, to deal with multicomponent

systems composed of elements with different equilibrium structures, one should describe individual elements using a common potential formalism. From this point of view, the MEAM interatomic potential created by Baskes [1] by modifying the EAM , can be a best candidate because of its applicability to a wide range of elements (bcc, fcc, hcp, diamond structures and even gaseous elements). The MEAM potentials for pure Mg [2], Al [3], Li [2] and binary Mg-Al [2], Mg-Li [2] were developed by the present authors. The MEAM formalism for pure elements and binary systems is fully documented in the literature [1,3] and will not be repeated here.

2.2 Calculation of CRSS

The samples of pure Mg, Mg-5at.%Al and Mg-10at.%Li binary alloys with 75,000 ~ 87,000 atoms were prepared by inserting the edge and screw dislocation in the basal, prism and pyramidal planes at the center of the each samples. The size of samples is about 24nm × 24nm × 3nm (length of dislocation). Periodic boundary conditions are applied in the direction of Burgers vector and dislocation line for edge and screw dislocation. To calculate the CRSS for basal slip and non-basal slip systems at a given temperature, MD simulations are performed at constant strain rate [4]. In order to apply strain, blocks of atoms in rigid coordination are created at the top and bottom of the atomic cell. The lower and upper box can be displaced rigidly to apply a shear strain to the cell of mobile atoms. The corresponding applied stress is computed from the force on individual atoms in the box.

3. Results

3.1 The change of *c*/*a* ratio of Mg

Tab. 1 shows the calculated lattice parameters and change of *c*/*a* ratio of Mg with the addition of alloying elements, Al and Li, at 0K. According to the present calculation, Al raises the *c*/*a* ratio of Mg and Li reduces the *c*/*a* ratio of Mg, as was reported experimentally [5].

Table 1. Calculated effect of alloying elements, Al and Li, on the lattice parameters and *c*/*a* ratio of Mg at 0 K.

	MEAM		MEAM		MEAM
Pure Mg	a = 3.2103	Mg-2at.% Al	a = 3.2043	Mg-10at.% Li	a = 3.1998
	c = 5.1924		c = 5.1864		c = 5.1705
	c/a = 1.6174		c/a = 1.6186		c/a = 1.6159
		Mg-5at.% Al	a = 3.1946	Mg-20at.% Li	a = 3.1890
			c = 5.1769		c = 5.1443
			c/a = 1.6205		c/a = 1.6131

3.2 CRSS for basal slip system

According to the present simulation, edge and screw dislocations on the basal plane dissociate into two Shockley partials whereas those on the prism and pyramidal planes do not. Fig. 1 shows the calculated CRSS for the edge and screw dislocations in the basal slip system.

As shown in Fig.1, the CRSS in basal slip system decreases with increasing temperature and is almost constant for T ≥ 300K. The CRSS for a screw dislocation is larger than that for an edge dislocation. In the case of the edge dislocation, the CRSS in Mg-Al and Mg-Li alloys are larger than that of pure Mg. However, in the case of a screw dislocation, the strengthening effect of the alloy elements is not clear. This can be explained by the fact that the stress field around a substitutional solute atom is spherically symmetric and therefore a substitutional solute atom does not interact with the shear stress field characteristic of screw dislocations.

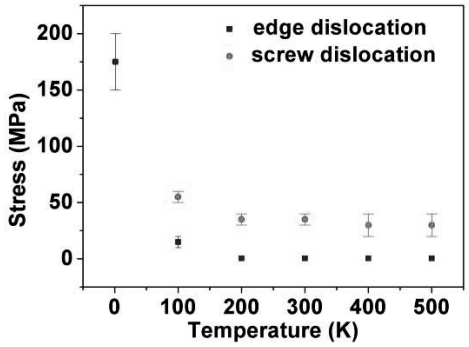

Fig. 1 Calculated CRSS for an edge and a screw dislocation in the basal plane by the MD simulation.

3.3 CRSS for non-basal slip system

Two non-basal slip systems, prism and pyramidal systems, were examined. According to the present simulation, screw dislocations are not stable on the prism and pyramidal planes in pure Mg and in the alloys at finite temperatures. During MD runs, dislocations on the prism and pyramidal planes disappear, and stacking faults are formed on the basal plane or other deformations occur. This means that prism and pyramidal slip systems cannot easily operate and the deformation on the basal plane is easier than that on non-basal planes. In the case of prism slip system, the CRSS for an edge dislocation in pure Mg (20~30 MPa at 100 K) is larger than that of the basal slip system. However, the strengthening effect of alloying elements in the prism slip system is smaller than that in the basal slip system. For example, the CRSS of a Mg-5at.% Al alloy is about 100 MPa in the prism slip system at 100K, while it is about 200 MPa in the basal slip system. In the case of pyramidal slip system, the strengthening effect of alloying elements is also smaller than that in the basal slip system. A similar tendency was observed in Mg-Li alloys. The present results indicate that the strengthening effect of alloying elements depends on the type of dislocation and slip plane.

4. Discussion

The effects of alloying elements on the CRSS in different slip systems of Mg are listed in Tab. 2. It is shown that the CRSS of magnesium would not be reduced by changing the *c*/*a* ratio through the addition of alloying elements. Fortunately however, the effects of alloying elements on the CRSS for the screw dislocation which is higher than that of the edge

dislocation and is therefore believed to have a decisive effect on the deformability of the alloys are not significant. Since the effects of alloying elements on the CRSS are different on different slip planes, it would be possible to adjust the anisotropy of CRSS depending on the type of slip plane by controlling the alloy contents of solute atoms. Further, it should be noted here that other deformation mechanisms (stacking faults, twins, etc.) were also observed during the present MD runs. Since the stacking fault energy is an important parameter closely related to the above-mentioned deformation behavior, it would be necessary to consider the change of stacking fault energy with addition of alloying elements in future studies.

Table 2. Calculated effects of alloying elements on the CRSS in different slip systems of Mg.

	edge dislocation		screw dislocation	
	Al	Li	Al	Li
basal	○	○	×	×
prism	○	○	N/A	N/A
pyramidal	○	○	N/A	N/A

*N/A : not available

5. Conclusions

Among the three potential slip planes (basal, prism and pyramidal) of hcp Mg alloys, the present MEAM simulation shows that the basal plane is the most favorable slip plane. The prism and pyramidal planes can also be active slip planes for edge dislocations, but not for screw dislocations. Addition of an alloying element, Al or Li, clearly increases the CRSS on all active slip planes of the edge dislocation, while the effect is not significant for the screw dislocation. The effect of alloying element on the CRSS depends on the type of slip plane, being larger on the basal plane than on the non-basal planes. The calculated change of the CRSS and the stacking fault energy with addition of alloying elements can be utilized simultaneously for designing Mg alloys with improved deformability.

References

[1] M.I. Baskes, “Modified embedded-atom potentials for cubic materials and impurities”, Physical Review B, **46**, 2727 (1992).
[2] Y.-M. Kim, B.J. Lee, Unpublished Work (2008)
[3] B.-J. Lee, J.-H. Shim and M.I. Baskes, “Semi-empirical atomic potentials for the FCC metals Cu, Ag, Au, Ni, Pd, Pt, Al and Pb based on first and second nearest-neighbor modified embedded atom method”, Physical Review B, **68**, 144112 (2003).
[4] Yu.N. Osetsky and D. J. Bacon, “An atomic-level model for studying the dynamics of edge dislocations in metals”, Modelling and Simulation in Materials Science and Engineering, **11**, 427 (2003)
[5] J.S. Park and Y.W. Chang, “The effect of Alloying Elements on the c/a Ratio of Magnesium Binary Alloys”, Advanced Materials Research, **26-28**, 95 (2007).

A model tight-binding Hamiltonian treatment of magnetic Fe-Cr alloys

Duc Nguyen-Manh, **Sergei L. Dudarev**

UKAEA Culham Science Centre, Abingdon, Oxfordshire, OX14 3DB
(E-mails: duc.nguyen@ukaea.org.uk, sergei.dudarev@ukaea.org.uk)

ABSTRACT

A model tight-binding Hamiltonian treatment of magnetic Fe-Cr alloys D. Nguyen-Manh and S.L. Dudarev EURATOM/UKAEA Fusion Association, Culham Science Centre, Oxfordshire, OX14 3DB, United Kingdom Fe-Cr binary alloys are representative model materials that exhibit a number of features, particularly those related to phase stability and microstructural evolution under irradiation, that are similar to those characterising ferritic-martensitic steels. Modelling Fe-Cr alloys presents a number of challenges since magnetism of both constituting elements of the alloy affects its behaviour in a complex way. This highlights the role played by electron exchange and correlations, giving rise to the spin polarization of 3d electrons, and to the observed anomalous magnetic properties of the alloy. In this presentation we propose a simple and physically transparent model for the Fe-Cr binary alloy based on a LSDA+U-like multi-orbital Hamiltonian [1], which we investigate using the mean-field Stoner approximation [2,3]. We show that a tight-binding local charge neutral model treatment of Fe-Cr that takes the total number of electrons occupying the 3d orbitals of Fe and Cr atoms as the only adjustable parameters, leads to the choice of numerical values for the exchange parameters J for Fe and Cr in very good agreement with ab-initio calculations. The model is able to describe all the significant aspects of the behaviour of the alloy found previously in full-scale density functional simulations, including not only the anomalous phase stability of the bcc binary system [4] but also the complex magnetic configuration of the Fe-Cr σ-phase [5] and the Bain transformation between bcc and fcc phases at low Cr concentrations.

This work, supported by the UK Engineering Physical Scientific Research Council and European Union under the contract of association between EURATOM and UKAEA, was carried out within the framework of European Fusion Development Agreement (Task No. TW6-TTMS-007).

[1] S.L. Dudarev, D. Nguyen-Manh and A.P. Sutton, Phil. Mag. B, 75 (1997) 613-628; S.L. Dudarev and P.M. Derlet, in Proceedings of MMM 2006, pp. 713-720; Scientific Modelling and Simulation (2008), doi 10.1007/s10820-008-9091-3
[2] D. Nguyen-Manh, V. Vitek and A.P. Horsfield, Prog. Mater. Sci. 52 (2007) 255-298.
[3] A. T. Paxton and M. W. Finnis, Phys. Rev. B77 (2008) 024428
[4] D. Nguyen-Manh, M.Yu. Lavrentiev and S.L. Dudarev, J. Nucl. Mater., (2008).
[5] D. Nguyen-Manh, M.Yu. Lavrentiev and S.L. Dudarev, Comp. Mater. Sci., (2008), http://dx.doi.org/10.1016/j.commatsci.2008.01.035.

Cohesion at Clean and Doped Grain Boundaries in bcc Iron

Adam Kiejna, Elwira Wachowicz

Institute of Experimental Physics, University of Wrocław, Plac M. Borna 9, 50-204 Wrocław, Poland
(E-mails: kiejna@ifd.uni.wroc.pl, elwira@ifd.uni.wroc.pl)

ABSTRACT

Impurities segregated at the grain boundary can drastically modify its properties. The effect of boron, nitrogen, oxygen, and phosphorus impurities on cohesive properties of Σ5 (210) and Σ3 (111) grain boundaries in ferromagnetic iron is studied from first principles, using density functional theory and the projector-augmented-wave method. This research supplements our previous study [1], by considering lower concentrations (larger supercells) and different impurities placed in interstitial and substitutional positions at the Fe Σ5 (210) grain boundary, and extends it by considering cohesive properties of the Fe Σ3 (111). It is found that full relaxation of the shape and volume of supercell, and relaxation of all atomic positions lead to stable asymmetric grain boundaries, which result from the relatively large parallel shifts of the grains with respect to each other. The variations of the grains shift and their separation are investigated as functions of the impurity concentration. The equilibrium distance between the grains is decreased for the impurities in substitutional positions and is increased for atoms in interstitial sites with respect to the relaxed, clean grain boundary. We discuss the energetics of the grain boundary cohesion and demonstrate that the embrittling or strengthening effect of a given impurity can be reversed depending on the impurity concentration. The chemical and mechanical contributions to the cohesive energy, related respectively to the bonding character of the impurity species, and to the atomic size of the impurity are extracted and discussed.

[1] E. Wachowicz and A. Kiejna, "Effect of Impurities on Grain Boundary Cohesion in bcc Iron", Computational Materials Science (2008), doi:10.1016/j.commatsci.2008.01.063.

This research was financially supported by the Polish Ministry of Science and Higher Education in the years 2006-09 under Grant No COST/201/2006.

Phase-field Prediction of Critical Nucleus Morphology in Solids

Lei Zhang[1], Long-Qing Chen[2] and Qiang Du[1,2]

[1]Department of Mathematics, Penn State University, University Park, PA 16802; [2]Department of Materials Science and Engineering, Penn State University, University Park, PA 16802 (E-mail: qdu@math.psu.edu)

ABSTRACT

One of the most efficient approaches to design the properties of a material is through the control of its phase transformations and microstructure evolution. The processes involved in a phase transformation are inherently multiscale. It starts with the nucleation of nanoscale nuclei of new phase particles, followed by growth and particle impingement or coarsening. In our recent works, we have developed a computational tool based on the phase-field description to predict the morphology of critical nuclei in solids under the influence of both interfacial energy anisotropy and long-range elastic interactions. Examples include cubic to cubic and cubic to tetragonal transformations. It is demonstrated that the morphology of critical nuclei in cubically anisotropic solids can be efficiently predicted without *a priori* assumptions. It is shown that strong elastic energy interactions may lead to critical nuclei with a wide variety of shapes including plates, needles, and cuboids with non-convex interfaces.

1. Nucleation

One of the most efficient approaches to design the properties of a material is through the control of its phase transformations and microstructure evolution. The processes involved in a phase transformation are inherently multiscale. It starts with the nucleation of nanoscale nuclei of new phase particles, followed by growth and particle impingement or coarsening.

Nucleation takes place when a material becomes thermodynamically meta-stable with respect to its transformation to a new state (solid, liquid and gas) or new crystal structure. Some common nucleation phenomena include formation of liquid droplets in a saturated vapor, appearance of ordered domains in a disordered solid, or nucleation of tetragonal variants in a cubic matrix, etc. Very often, it is the nucleation process that dictates the microstructure of a material. Predicting the shape of a critical nucleus in solids has been a long-standing problem in solid-state phase transformations. It is generally believed that nucleation in solid is by far the most difficult process to model and predict. Nucleation in a solid typically involves not only composition changes but also structural changes. Moreover, interfacial energy is usually anisotropic, and the elastic energy contribution arising from the lattice mismatch between nuclei and matrix plays an important role in determining the morphology of critical nuclei.

2. Existing Nucleation Theory

Early nucleation theories mostly considered phase changes in fluids, e.g. a liquid droplet in a vapor phase, and naturally assumed spherical shapes for the critical nuclei. In the classical theory

of nucleation, the thermodynamic properties of a nucleus are assumed to be uniform and the same as in the corresponding bulk phase at equilibrium. The interface between a nucleus and the parent phase is considered to be sharp. The calculation of a critical nucleus size is then determined by the competition between the bulk free energy reduction and interfacial energy increase. A nucleation event takes place by overcoming the minimum energy barrier which leads to the critical size of the nucleus obtained as a stationary point of the energy. Despite the assumption of spherical shapes for critical nuclei, the same classical theories have been utilized to interpret kinetics of many phase transformations involving solids including solid to solid transformations. For some systems, the classical nucleation theory has been shown to provide a good description on the nucleation kinetics.

While it is reasonable to assume spherical shapes for nuclei during fluid-fluid phase transitions, the morphology of critical nuclei in solids is expected to be strongly influenced by anisotropic interfacial energy and anisotropic elastic interactions. For example, nuclei for γ' precipitates in Ni-alloys can be cuboidal or spherical depending the lattice mismatch between the precipitate and matrix, θ' precipitates in A1-Cu are plates, and the β' precipitates in Al-Mg-Si alloys are needle-shaped. The morphology of a critical nucleus in the presence of interfacial energy anisotropy alone can be deduced from the well-known Wulff construction. However, pre Dicting the shape of a critical nucleus in the presence of both elastic energy and surface energy anisotropy is particularly challenging since elastic energy contribution depends on the morphology of a nucleus and lattice mismatch between the nucleus and the matrix. As a result, prior applications of the classical nucleation theory to solid state transformations typically make assumptions on the shape of a nucleus as an *a priori*, and the elastic energy contribution to nucleation is included as an extra barrier for nucleation.

Another theoretical approach to nucleation is based on the diffuse-interface description, also called the non-classical nucleation theory. In this approach, the properties within a nucleus are inhomogeneous and the interface between the nucleus and parent matrix is diffuse. Following the seminal work of Cahn and Hilliard [1], the diffuse-interface approach has been previously applied to nucleation in solids (see [2] for a long list of references).

3. Phase Field Approach and Variational Calculation

In a series of recent works, we reported a computational approach for predicting the morphology of a critical nucleus as an extreme state in two dimensions by considering the presence of both interfacial energy anisotropy and elastic interactions [2-6]. The computation is based on a very general phase field framework with a diffuse interface description of the phase transformation for which the total energy incorporates the bulk energy, interfacial energy, chemical driving force and the contributions of the elastic energy.

3.1 Diffuse interface framework

The non-classical theory was pioneered by Cahn and Hilliard [1]. Since then, generalization and application to nucleation in solids have also been made. It should be pointed out that these

existing diffuse interface theories for nucleation in solids have largely ignored the anisotropic interfacial energy and anisotropic long-range elastic interactions until recently [2].

In the letter [2], we reported a computational approach for predicting the morphology of a critical nucleus as an extreme state in two dimensions by considering the presence of both interfacial energy anisotropy and elastic interactions. Two dimensional examples indicate that the morphology of a critical nucleus, or a critical fluctuation in elastically anisotropic solids can be predicted by a combination of the diffuse-interface approach and the minimax algorithm. Our calculations reveal the fascinating possibility of nuclei with non-convex shapes, as well as the phenomenon of shape-bifurcation and the formation of critical nuclei whose symmetry is lower than both the new phase and the original parent matrix.

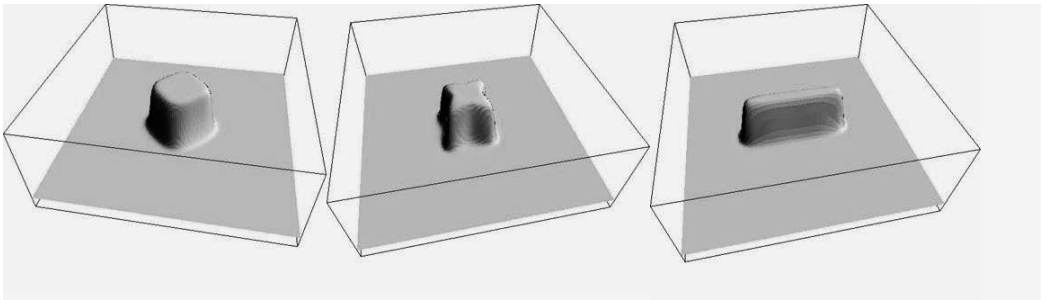

Figure 1. The change in two dimensional critical nuclei with different contributions from the anisotropic elastic energy

3.2 Rigorous mathematical theory

In a subsequent work [3], some rigorous mathematical and numerical analysis of the underlying diffuse interface framework for the nucleation in solid state phase transformations are discussed. The mathematical formulation of the diffuse-interface description of a critical nucleus is analyzed within the context of critical point theory for nonlinear variational problems [4]. In particular, the well-known Palais-Smale condition is verified which leads to the existence of saddle points for the free energy functional that includes the contributions of the anisotropic elastic energy in the form derived in [5].

In [3], we also described the numerical algorithms used to search for the saddle points of the free energy functional based on a minimax technique and the Fourier spectral implementation. A detailed presentation of the minimax algorithm based on the mountain path theorem in the calculus of variation is provided., The effect of Fourier spectral approximations is examined.

3.3 Other generalizations.

Further three dimensional computational results are reported in [6] for a particular example of cubic to cubic transformation within the homogeneous modulus approximation. Three dimensional examples are given, see Fig.2 for an illustration. In more recent works, the framework developed in [2] was extended to the case of critical nucleus in the conserved field in [7]. Following the idea giving in [9], a constrained string method is developed in [7] for the minimum energy path calculation in the conserved field case which has been shown to have

many nice approximation features. Generalizations to the case of the cubic to tetragonal transformations have been made in [8].

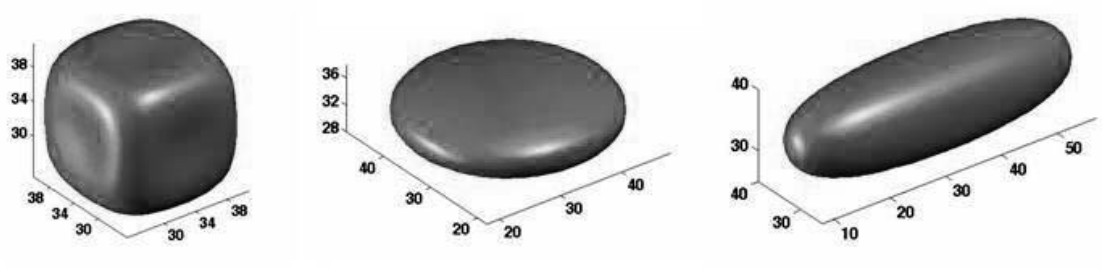

Figure 2. Three dimensional critical nuclei with non-convex, plate and needle shapes.

Acknowledgements

This work is supported in part by SF-DMR ITR 0205232, NSF-DMS 0712744, NSF-IIP 541674 and the NSF PSU/GT Center for Computational Materials Design (CCMD).

References

[1] J. Cahn and J. Hilliard, "Free energy of a nonuniform system, III. Nucleation in a two-component incompressible fluid," J. Chem. Phys. **31** (1959), 688-699.
[2] L. Zhang, L. Chen and Q. Du, "Morphology of critical nuclei in solid state phase transformations", **Physical Review Letters**, **98**, 265703, (2007),
[3] L. Zhang, L. Chen and Q. Du, "Mathematical and Numerical Aspects of Phase-field Approach to Critical Morphology in Solids". Journal of Scientific Computing, to appear, (2008).

[4] P. Rabinowitz, Minimax Methods in Critical Point Theory (AMS, Provindence, 1986).
[5] A. Khachaturyan, Theory of Structural Transformations in Solids, (Wiley, New York, 1983).
[6] L. Zhang, L. Chen and Q. Du,"Diffuse-interface description of strain-dominated morphology of critical nuclei in phase transformations", **Acta Materialia**, 56, pp.3568-3576, (2008).
[7] L. Zhang, L. Chen and Q. Du, "Predicting critical nucleus in the conserved solid field by the constrained string method, preprint, (2008).
[8] L. Zhang, L. Chen, Q. Du, "Effect of elastic energy to critical nucleus in cubic to tetragonal system, preprint, (2008) .
[9] W. E, W. Ren and E. Vanden-Eijnden, "String method for the study of rare events", Physical Review B, **66** (2002), 052301.

Rapid And Accurate Estimate Of Alloy Phase Transition Temperatures

Teck L. Tan[1], Duane D. Johnson

[1] University of Illinois Urbana-Champaign, Dept. of Materials Science and Engineering, 1304 W. Green St., Urbana, IL 61801, USA, (E-mail: tecktan2@uiuc.edu)

ABSTRACT

To aid in rapid materials assessment, we use improved mean-field estimates(s) for rapid but accurate prediction of alloy order-disorder temperatures (T_c) and phase boundaries via the cluster expansion (CE). In the CE, $E(\sigma) = \Sigma_i V_i \langle \Phi_i \rangle$ is the energy for any structure σ, where V_i and $\langle \Phi_i \rangle$ are, respectively, the *i*-th cluster interaction and correlation function. The V_i are derived from a database of structural energies obtained from density functional theory (DFT). Typically, Monte Carlo is used to construct T vs. c phase diagrams, which involves CPU days. However, the boundaries can be accurately and "instantly" depicted from mean-field approximations using the CE Hamiltonian that follows conservation sum rules, which go beyond Bragg-Williams and are significantly less complicated than the popular cluster variation method. We demonstrate rapid estimates of T_c at stochiometric compositions with phase boundaries, and their accuracy for several alloy systems vis-à-vis Monte Carlo simulations. The above is implemented in our multiscale thermodynamic toolkit, TTK, which will be made available for public use.

We acknowledge support from the CSE Fellowship at University of Illinois Urbana-Champaign and NSF DMR-07-05089, DMR-03-12448 and computational resources from DMR-03-25939.

Modeling and simulations of polycrystalline SiC thin film through a coupled atomistic continuum theory

Liming Xiong, Youping Chen

Department of Mechanical and Aerospace Engineering, Gainesville, FL 32611
(E-mails: lmxiong@ufl.edu, ypchen2@ufl.edu)

ABSTRACT

This paper presents the application of a coupled atomistic continuum theory (CACT) in multiscale modeling and simulation of boron- , boron/nitrogen and silicon/nitrogen-doped polycrystalline silicon carbide with average grain size . Intergranular glassy films (IGFs) and nano-sized pores are obtained in triple junctions of the grains in polycrystalline SiC. Under uniaxial tension, the constitutive responses of polycrystalline SiC are reproduced from the simulations. Intergranular fracture is observed. Results show that the mechanical properties of polycrystalline SiC are dependent on grain size, thickness and compositions of grain boundaries (GBs). In summary, CACT has been proved to be more efficient than fully molecular dynamics (MD) simulations. Beyond the reach of classical continuum filed theory, with atomic resolution on the GBs and coarse resolution in the grains, CACT has been successfully employed to simulate large deformation and failure of polycrystalline ceramics without any numerical treatments or failure criteria.

High-Throughput Measurements for High-Fidelity Materials Databases for Accelerated Materials Design

J.-C. Zhao[1], Xuan Zheng[2], David Cahill[2]

[1]The Ohio State University
[2]University of Illinois at Urbana-Champaign
(E-mails: zhao.199@osu.edu, xzheng2@uiuc.edu, d-cahill@uiuc.edu)

ABSTRACT

This talk will illustrate high-throughput measurements for fast establishment of materials databases for accelerated materials design and discovery. The methodology is based on a simple idea of taking advantage of the compositional gradients and phase formation in diffusion couples and diffusion multiples to perform localized property measurements. Such measurements require a new suite of materials property microscopy tools with micron-scale resolution, but would greatly accelerate the efficiency of data gathering as compared to traditional measurements on individual alloys. The local equilibrium at the phase interfaces allows fast evaluation of phase diagrams which are essential input to CALPHAD modeling. Micron-scale resolution tools were developed in recent years to measure thermal conductivity, elastic modulus, and coefficients of thermal expansion (CTE). The power of application of these tools on diffusion multiple samples to establish materials property databases will be illustrated using several examples. For instance, a micro-scale thermal conductivity technique can be used to study order-disorder transformation, site preference in intermetallic compounds, solid-solution effect on conductivity, and compositional point defect formation. These tools can be applied not only to accelerate the development of structural materials, but also to discover new functional materials.

Incorporating Grain Size Effects into Microstructure Design

Brent L. Adams, Bradley S. Fromm and Sadegh Ahmadi

**Department of Mechanical Engineering, Brigham Young University,
455 CTB, Provo, UT 84602 USA (E-mail: b_l_adams@byu.edu)**

ABSTRACT

A method to incorporate grain size effects into crystal plasticity is presented. The classical Hall-Petch equation inaccurately predicts the macroscopic yield strength for materials with non-equiaxed grains or materials that contain unequal grain size distributions. These deficiencies can be overcome by incorporating both grain size and orientation characteristics into crystal plasticity theory. Homogenization relationships based on a viscoplastic Taylor-like approach are introduced along with a new function, the grain size and orientation distribution function (GSODF). Estimates of the GSODF for high purity α-titanium are recovered through orientation imaging microscopy coupled with chord length measurements. A comparison between the new method and the traditional viscoplastic Taylor approach is made by evaluating yield surface plots. The implications of adding grain size to the list of local state variables, in the context of microstructure design, are considered.

Computational Design of Advanced Nuclear Fuels

Marius Stan[1], Bogdan Mihaila[1], David Korzekwa[1], Petrica Cristea[2], Juan Ramirez[3]

[1]Los Alamos National Laboratory, Los Alamos, New Mexico, USA
(E-mails: mastan@lanl.gov, bmihaila@lanl.gov, dak@lanl.gov)
[2]Univ. of Bucharest, Romania (E-mail: pcristea@gmail.com)
[3]Exponent, Inc., USA (E-mail: jramirez@exponent.com)

ABSTRACT

In nuclear reactors fuels and structural materials are subject to severe radiation fluxes that induce changes in material's properties such as in micro-structure, density, thermal conductivity, specific heat, and species diffusivity. The presentation starts with a review of the major challenges encountered in the design of advance nuclear fuels that can withstand fast reactor environments and continues with recent results obtained at Los Alamos National Laboratory. Special attention is given to multi-scale models that relate the fuel properties to microstructure, defect concentration, composition, and temperature and assist the design of fuels with specific, targeted properties. Furthermore, finite element simulations of coupled heat transfer, oxygen diffusion, and thermal expansion in U-Pu-O fuels include the effect of temperature and local composition, leading to evaluation of fuel performance and providing feedback to the oxide fuel design and manufacturing. The phase stability of U-Pu-Zr metallic fuels is evaluated in the context of casting simulations that guide fuel development and optimization. For both fuel types, the consequences of the presence of minor actinides and fission products is discussed

The Virtual Turbine Blade: Multi-Length Scale Characterization of a Single-Crystal Turbine Blade

Christopher Woodward, Michael Groeber, Mark Tschopp, Andrew Rosenberger, Dennis Dimiduk, Stephan Russ

Air Force Research Laboratory, Ohio, USA
(E-mail: christopher.woodward@wpafb.af.mil)

ABSTRACT

Single crystal Ni-base superalloys were developed primarily for turbine blade applications, where creep properties have been a major concern. Due to the increasingly complex cooling configurations used in advanced turbine blade designs thermally driven stresses, and thermo-mechanical fatigue (TMF), have become major concerns as well. In order to meet the demands of higher performance applications we are exploring a microstructure sensitive design approach. The ultimate goal is a multi-length scale statistical representation of the blade microstructure which will allow the generation of equivalent synthetic microstructures of a virtual turbine blade. This materials representation will be used to inform property prediction tools (design tools) of single-crystal Ni-base superalloy turbine blades. The first step toward that end is a multi-length scale characterization of actual turbine blades. Emphasis has been placed on characterizing distributions - to include number density, size, and spatial relationship - of microstructural features that are thought to be critical drivers for strength, creep, fatigue, and TMF properties. Microstructural features of immediate interest include dendrite orientation and size, gamma prime "stringers", eutectic phases, porosity, carbides, and gamma prime. Attention to microstructural spatial relationships relative to geometric features of an actual blade is also addressed. This presentation will discuss recent quantitative characterization of a commercial turbine blade fabricated from PWA1484 and outline an approach for the multi-length scale representation of the material.

Ab Initio Based Modeling of Engineering Materials: From a Predictive Thermodynamic Description to Tailored Mechanical Properties

Jörg Neugebauer

Max-Planck-Institut für Eisenforschung GmbH, Computational Materials Design, Max-Planck-Straße 1, D-40237 Düsseldorf
(E-mail: neugebauer@mpie.de)

ABSTRACT

Density functional theory (DFT) has emerged as a versatile and powerful tool to predict a wide range of materials and properties. While originally developed and used as a ground state T=0K theory there a rapidly growing interest in using it for the computation of finite temperature properties as crucial e.g. to design engineering materials. In the talk I will discuss how a combination of ab initio methods with thermodynamic concepts [1,2] and including all relevant mechanisms such as harmonic and anharmonic vibrations, electronic and magnetic excitations, point defects and configurational disorder, allows a reliable and accurate determination of free energies. The possibilities and the predictive power which this approach offers will be discussed for the following examples: determination of solubility limits in alloys, identification of metallurgical trends, and tailoring mechanical properties [3].

[1] B. Grabowski, T. Hickel and J. Neugebauer: "Ab initio study of the thermodynamic properties of nonmagnetic elementary fcc metals: Exchange-correlation-related error bars and chemical trends", Phys. Rev. B 76, 024309 (2007)

[2] F. Körmann, A. Dick, B. Grabowski, B. Hallstedt, T. Hickel and J. Neugebauer: „The free energy of bcc iron: Integrated ab initio derivation of vibrational, electronic, and magnetic contributions, Phys. Rev. B 78, 033102, (2008)

[3] D. Raabe, B. Sander, M. Friak, D. Ma, J. Neugebauer: "Theory-guided bottom-up design of b-titanium alloys as biomaterials based on first principles calculations: Theory and experiments", Acta Mat. **55**, 4475–4487 (2007)

Electronic Excitations in Branched Conjugated Molecules Using Exciton Scattering Approach

Chao Wu[1], Sergey V. Malinin [1], Sergei Tretiak [2] and Vladimir Y. Chernyak [1]

[1] Department of Chemistry, Wayne State University, 5101 Cass Ave, Detroit, MI 48202
[2] Theoretical Division, Center for Nonlinear Studies, and Center for Integrated Nanotechnologies, Los Alamos National Laboratory, Los Alamos, NM 87545
(E-mail: chaowu@chem.wayne.edu)

ABSTRACT

The exciton scattering (ES) theory attributes excited electronic states to standing waves in quasi one-dimensional materials, assuming quasi-particle picture of optical excitations [1]. Using quantum chemical calculations (time-dependent Hartree-Fock and density functional theory (TDHF and TDDFT)) we extract all relevant parameters of the ES model for π-conjugated phenylacetylene molecular structures [2]. The resulting frequency dependent dispersion spectra and scattering matrices of termini and joints allow calculations of electronic spectrum for any arbitrary structure within considered molecular structure library with trivial numerical expense. An agreement within 10-20 m*eV* is observed for all test cases when comparing the ES results with direct quantum-chemical calculations.

[1] C. Wu, S.V. Malinin, S. Tretiak, V.Y. Chernyak, "*Exciton Scattering and Localization in Branched Dendrimeric Structures*", Nature Physics, **2**, 631 (2006).
[2] C. Wu, S.V. Malinin, S. Tretiak, V.Y. Chernyak, "*Multiscale Modeling of Electronic Excitations in Branched Conjugated Molecules Using an Exciton Scattering Approach*", Physical Review Letters, **100**, 057405 (2008).

This work is supported by the National Science Foundation under Grant No. CHE-0808910. Los Alamos National Laboratory is operated by Los Alamos National Security, LLC, for the National Nuclear Security Administration of the U.S. Department of Energy under contract DE-AC52-06NA25396. We acknowledge support of Center for Integrated Nanotechnology (CINT) and Center for Nonlinear Studies (CNLS).

Mechanically Altered Carbon Nanotubes

Yaroslav V. Shtogun and Lilia M. Woods

Department of Physics, University of South Florida, 4202 E Fowler Ave, Tampa FL, 33620
(E-mail: yshtogun@cas.usf.edu)

ABSTRACT

Ab initio calculations are presented for the electronic structure of radially deformed and defective (8,0) single walled carbon nanotube. The considered defects are a Stone-Wales defect, a Nitrogen impuriry and a mono-vacancy. The combined effect of radial deformation and a single mechanical defect is analyzed in terms of band gap, formation energy and total density of states changes.

1. Introduction

Carbon nanotubes (CNT) are quasi-one dimensional seamlessly rolled cylindrical graphite sheets. They can display metallic or semiconducting properties depending on their chirality index *(n,m)*, which determines the particular way the graphene is rolled [1]. Recent studies have shown that mechanical alterations can cause singificant changes in the nanotube properties [2]. These results have been considered to be important with respect to achieving different carbon nanotube based functional devices. Experiments, such as squashing the nanotubes with an AFM tip or between two hard walls, can probe their electromechanical response as metal-semiconductor transitions can occur [3]. Similar effect can be achieved if external hydrostatic pressure is applied [4]. In addition, the presence of various types of mechanical defects can also change the CNT properties. The defects can appear at the stage of synthesis, purification, or device production. Moreover, defects can be created deliberately by chemical treatments or irradiation [5].

Most theoretical works so far report studies of radially deformed *or* defective CNTs [6]. Here we investigate theoretically additional ways of changing the CNT structure and properties by applying radial squashing *and* a mechanical defect on the carbon nanotube. The calculated electronic structure for the various cases reveals how the CNT electronic characteristics can be modified if defects and radial deformation are applied.

2. Method of Calculations

The results are obtained by self-consistent density functional theory (DFT) calculations using the Vienna Ab Initio Simulation Package (VASP) within the local density approximation (LDA) for the exchange-correlation energy functional [7]. $(1\times1\times7)$ Monkhorst-Pack *k*-grid sampling of the Brillouin zone was taken with an energy cutoff of 420 eV. The convergence

criteria for relaxation are10^{-5} eV for the total energy and 0.005 eV/Å for the force. We take (8,0) single walled CNT (one graphene) to illustrate our calculations. A super-cell is constructed with dimensions of 17.3 Å in axial and 22.12 Å in transverse directions (after relaxation).

The radially deformed (8,0) CNT was calculated first. The deformation is obtained by squeezing in the *y*-direction and elongating in the *x*-direction, and it is characterized by a dimensionless parameter $\eta=(R - R_y)/R$, where R is the radius of the perfect CNT and R_y is the semi-minor axis connecting the CNT lowest curvature regions – Fig. 1a) and 1b). For all η the system is relaxed by freezing only the *y*-coordinate of the atoms on the top and bottom rows of the flattened regions while all others are let free.

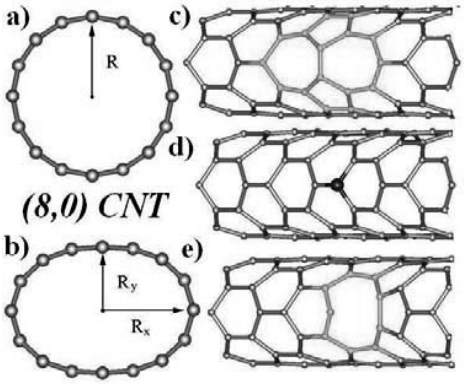

Figure 1. a) Perfect undeformed; b) Radially squeezed; and radially squeezed with c) a SW defect; d) a *N* impurity; and e) a mono-vacancy.

After this relaxation, a single defect on the highest curvature regions in the supercell is created – Stone-Wales (SW) defect (Fig. 1c), a *N* substitional impurity (Fig. 1d), and a mono-vacancy (Fig. 1d). For the *N* and vacancy defects, spin-polarized calculations are done because of the open electron shell structure, while the others are non-spin-polarized calculations. Relaxation of the deformed and defective CNT is also performed with the constraint as in the case for the deformed CNT. Such procedure corresponds to first deforming the nanotube and then introducing the defect in its structure.

3. Results and Discussion

The electronic structure of the defect-free deformed (8,0) CNT is calculated first. The perfect, undeformed (8,0) CNT is semiconducting with relatively large band gap – E_g = 0.55 eV. Applying radial deformation causes a decrease of the band gap - Fig. 2a). At η=0.25 E_g is closed, thus (8,0) CNT becomes metallic. We find that if the constraint on the *y*-coordinates is removed the CNT returns to its original circular form.

Next, we simulate the single defects on the highest curvature sides of the deformed and relaxed (8,0) CNT. The SW bond rotation and the mono-vacancy induce local "buldging" of the CNT structure, which becomes more pronounced as η is increased. The *N* atom substitution does not change the physical structure of the deformed CNT significantly. We also find that the deformed and defective CNT returns to its original form (undeformed CNT with a defect) if all atoms are allowed

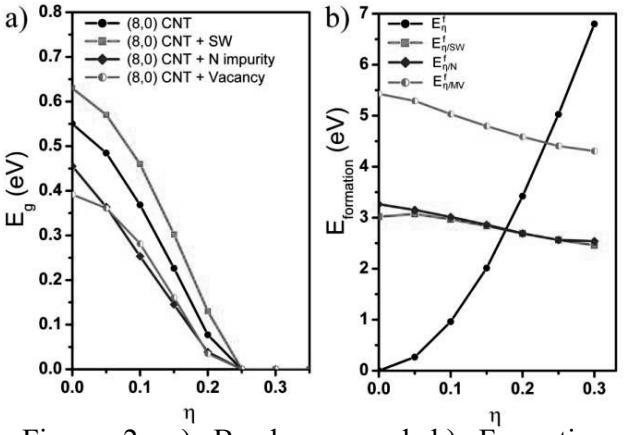

Figure 2. a) Band gap and b) Formation energies for deformation and defects on (8,0) CNT vs. radial deformation.

to relax.

The evolution of the band gap as a function of η - Fig. 2a) – shows that E_g closes at η = 0.25 for all three defects. However, the band gap is larger for the nanotube with the SW defect for $\eta < 0.25$ as compared to the perfect-deformed CNT. There is little difference between the band gaps for the deformed CNT with *N* and mono-vacancy defects. These E_gs are smaller than E_g for the perfect-deformed CNT. We also show the formation energy needed to deform the circular (8,0) tube, as well as the formation energy for each defect on the deformed nanotube – Fig. 2b). These are calculated as:

$$E^f_\eta = E_\eta - E \quad (1)$$

$$E^f_{\eta/SW} = E_{\eta/SW} - E_\eta \quad (2)$$

$$E^f_{\eta/N} = E_{\eta/N} - E_\eta - \mu_N + \mu_C \quad (3)$$

$$E^f_{\eta/MV} = E_{\eta/MV} - E_\eta - \mu_N + \mu \quad (4)$$

where E^f_η is the energy for deformation, $E^f_{\eta/SW,N,MV}$ – formation energy for a SW defect, N impurity and mono-vacancy (MV), respectively, E_η - total energy for the deformed CNT, $E_{\eta/SW,N,MV}$ - total energies for the appropriate deformed-defective CNT, E - total energy for undeformed CNT, $\mu_{N,C}$ - chemical potentials for free nitrogen and carbon atoms, respectively, and μ - chemical potential of carbon atom from the CNT. Fig. 2b) shows that E^f_η increases in a non-linearly as a function of η indicating that more energy is needed to squeeze the nanotube. However, $E^f_{\eta/SW,N,MV}$ decreases as a function of η, thus less energy is needed to create a defect on the deformed nanotube. The figure also shows that there is little difference between $E^f_{\eta/SW}$ and $E^f_{\eta/N}$ and it is more difficult to create a vacancy rather than SW or *N* defect on the CNT side.

The combined effect of the different defects and degrees of deformation can be further revealed by analyzing the electronic structure of the (8,0) CNT – Fig. 3. We consider the SW defect. The calculation did not include spin-polarization effects. The radial squeezing brings the conduction energy bands closer to the Fermi level as η is increased, while the valence bands are not affected as much – Fig. 3e). Thus E_g is decreased. The SW defect affects the deeper valence region (~-5.4 eV) for both *η=0* and *η=0.2* cases – Fig. b,f), where a sharp peak is found. The valence bands are lowered leading to an increase in the band gap - from E_g =0.08 eV for the deformed nanotube to E_g = 0.13 eV for the deformed CNT with SW.

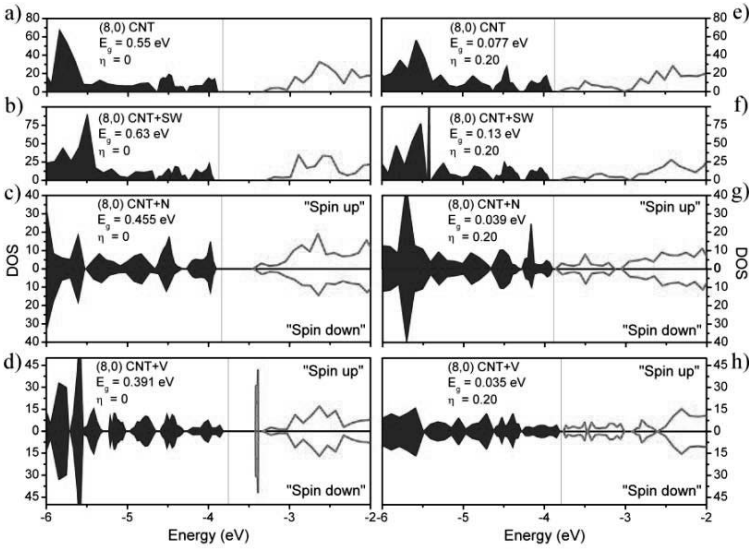

Figure 3. Total DOS for a) perfect CNT; with b) SW defect; c) *N* impurity; d) mono-vacancy at η = 0.0; e) deformed CNT; with f) SW defect; g) *N* impurity; h) mono-vacancy at η = 0.20.

For the *N* impurity, the electron shell system is partially filled since the *N* atom has an extra *e* as compared to *C*. The spin-polarized calculations show that the total DOS for spin-up and spin-down carriers is different for undeformed and deformed CNT. For *η=0* (Fig.3c), there are additional features at

~-4.5 eV in the DOS valence region as compared to DOS for the deformed CNT (Fig.3g). For $\eta=0.2$ there is larger difference between spin-up and spin-down for the peak at ~ -4.2 eV. The difference in the spin-up and spin-down in the total DOS implies that the undeformed and deformed CNT with *N* substitutional impurities can have magnetic properties.

The results for a mono-vacancy are also shown – Fig. 3d) and 3h). The spin-polarized DOS shows that there is no difference in the spin-up and spin-down states for the (8,0) CNT at η= 0.0 and η = 0.20. Thus no magnetism can be induced in a defective CNT with a mono-vacancy even though the CNT. Peak-like features attributed to the vacancy are found at ~-3.4 eV and ~-5.5 eV regions for the undeformed nanotube, and they are pushed further up in the conduction region and down in the valence region, respectively, as η is increased.

4. Conclusions

We have shown that combined application of mechanical defects and deformation can lead to various changes in the electronic structure of carbon nanotubes. Our results show that the complete closure of the gap for the studied CNT is mainly due to the radial squeezing. However, the gap can be increased or decreased before the closure depending on the type of defect. In addition, CNT can exhibit magnetic properties if a substitutional impurity is present.

Acknowledgements

Financial support from the Petroleum Research Fund is acknowledged. L.M.W. was also partially supported by the Center for Integrated Functional Materials (CIFM) through Grant No. USAMRMC-07355004. We also acknowledge the services of the Research Computing Core at the University of South Florida.

References

[1] R. Saito, G. Dresselhaus, and M. S. Dresselhaus, “Physical Properties of Carbon Nanotubes” (Imperial College Press, London, 1998).

[2] D. Qian, G. J. Wagner, W. K. Liu, M. F. Yu, and R. S. Ruoff, ”Mechanics of carbon nanotubes”, Appl. Mech. Rev. **55**, 495 (2002).

[3] B. Shan, G.W. Lakatos, S. Peng, and K. Cho, ”First-principles study of band-gap changes in deformed nanotubes”, Appl. Phys. Lett. **87**, 173109 (2005).

[4] L.Vitali, M. Burghard, P. Wahl, M. A. Scheider, and K.Kern, “Local Pressure-Induced Metallization of a Semiconducting Carbon Nanotube in Crossed Junction”, Phys. Rev. Lett. **96**, 086804 (2006).

[5] P.M. Ajayan, V. Ravikumar, and J.-C. Charlier, ” Surface Reconstructions and Dimensional Changes in Single-Walled Carbon Nanotubes”, Phys.Rev. Lett. **81**, 1437 (1998).

[6] Y.He, C. Zhang, C. Cao, and H. Cheng, “Effects of strain and defects on the electron conductance of metallic carbon nanotubes“, Phys. Rev. B **75**, 235429 (2007).

[7] G. Kressen and J. Futhmuller, “Efficient iterative schemes for *ab initio* total-energy calculations using a plane-wave basis set”, Phys. Rev. B **54**, 11169 (1996).

Quantum, Statistic and Continuum Thermodynamics of Material

Zi-Kui Liu

The Pennsylvania State University, University Park, PA 16802, USA
(E-mail : zikui@psu.edu)

ABSTRACT

From the viewpoint of engineering design, materials design is a process to determine optimal combinations of controllable quantities such as material chemistry, processing routes, and processing parameters to robustly meet specific performance requirements through measurable quantities such as ferroelectric/ferromagnetic properties, mechanical properties and corrosion resistance. This process is iterative by nature due to the incompleteness of design knowledgebase, which has been created predominantly by experiments. The computational community still faces challenges in predicting accurately the most fundamental properties of materials, i.e. thermodynamics and diffusion coefficients, which dictate phase stability and phase transformation in materials. In this presentation, we will discuss our recent progresses in predicting a number important properties for metals and oxides through quantum mechanics, statistic mechanics, and classic thermodynamics.

Vacancy Segregation in the Initial Oxidation Stages of the TiN(100) Surface

Janina Zimmermann[1], Mike W. Finnis[2], Lucio Colombi Ciacchi[1, 3]

[1]Fraunhofer Institute for Mechanics of Materials IWM, Wöhlerstr. 11, 79108 Freiburg, Germany (E-mail: janina.zimmermann@iwm.fhg.de)
[2]Imperial College London, Department of Materials, London SW7 2AZ, United Kingdom (E-mail: m.finnis@imperial.ac.uk)
[3]Institute for Reliability of Systems and Devices IZBS, University of Karlsruhe, 76131 Karlsruhe, Germany (E-mail: lucio@izbs.uni-karlsruhe.de)

ABSTRACT

The realistic modeling of biomaterials interfaces to biological systems requires the use of a range of simulation techniques spanning from fully quantum to fully classical. Quantum mechanical simulations provide accurate information about atomistic structure, charge distribution, electronic structure and surface stress of materials surfaces. These data are the basis for the development of classical potentials that model the interactions between surfaces and external environments on a larger scale. In particular, the well-known biocompatibility of TiN (often used as a coating material for Ti-based medical implants [1]) depends on the structural and chemical properties of the stable oxide film which forms spontaneously on its surface after exposure to air. In the present work, we focus on the atomistic structure and the stability of a TiN(100) surface in contact with an oxidizing atmosphere. The early oxidation stages of TiN(100) are investigated by means of first-principles molecular dynamics (FPMD). We observe selective oxidation of Ti atoms and formation of an ultrathin Ti oxide layer, while Ti vacancies are left behind at the metal/oxide interface. Within the formalism of ab-initio thermodynamics [2] we study the driving forces for vacancy diffusion from the metal/oxide interface to the bulk (and vice versa) and for the formation of vacancy clusters. This is accompanied by an accurate study of surface stability of the system obtained directly by FPMD simulations with respect to reconstructed defect-free model systems. While ideally reconstructed systems can be thermodynamically more stable, only systems obtained by FPMD can account for the early formation of nitrogenous gases, as observed in room-temperature oxidation experiments. We suggest that superficial oxidation may proceed along a pathway of metastable intermediate structures which form due to the large heat developed during the reactions with molecular oxygen and are stabilized by vacancy clustering at the metal/oxide interface.

[1] P. A. Dearnley, “A Review of Metallic, Ceramic and Surface-treated Metals Used for Bearing Surfaces in Human Joint Replacements”, Proceedings of the Institution of Mechanical Engineers, Part H: Journal of Engineering in Medicine, **213,** 107 (1999).
[2] M. W. Finnis, A. Y. Lozovoi, and A. Alavi, “The Oxidation of NiAl: What Can We Learn from Ab Initio Calculations?”, Annual Review of Materials Research, **35,** 167 (2005).

This work is supported by the Deutsche Forschungsgemeinschaft and partially funded by the HPC-EUROPA Project and the Thomas Young Centre (TYC).

Crystal Construction Based On Periodic Surfaces

Cheng Qi and Yan Wang

**Department of Industrial Engineering & Management Systems,
University of Central Florida, Orlando, FL 32816
(E-mail: cqi@mail.ucf.edu, wangyan@mail.ucf.edu)**

ABSTRACT

Providing nano engineers and scientists efficient and easy-to-use tools to create geometry conformations that have minimum energies is highly desirable in material design. Recently we developed a periodic surface model to assist the construction of nano structures parametrically for computer-aided nano-design. In this paper, we present a feature-based approach for crystal construction. The proposed approach starts the model creation with basic features by the aid of periodic surfaces, followed by operations between the basic features. The goal is to introduce a rapid construction method for complex crystal structures.

1. Introduction

Computer-aided nano-design (CAND) is an extension of computer based engineering design traditionally at bulk scales to nano scales. In this paper, we proposed a new feature-based approach to create crystal structures based on a periodic surface (PS) model [1, 2]. Feature has been extensively used in traditional computer-aided design (CAD) systems. It is the basic operational unit that has engineering or functional implications. Here we define nanoscale features to represent some commonly used crystal structures and patterns in material design. This new feature-based crystal modeling approach is to increase the efficiency of crystal model construction, which is particularly important to design complex nano material systems in the future. In the remainder of the paper, Section 2 describes the basis of the periodic surface model. Section 3 defines some basic features of PS models for crystals, and Section 4 presents methods of feature operations.

2. Periodic Surface

A periodic surface (PS) is an implicit surface model, which is generally defined as [1, 2]

$$\psi(\mathbf{r}) = \sum_{l=1}^{L}\sum_{m=1}^{M} \mu_{lm} \cos\left(2\pi\kappa_l(\mathbf{p}_m^T \cdot \mathbf{r})\right) = 0 \tag{1}$$

where κ_l is the scale parameter, $\mathbf{p}_m = [a_m, b_m, c_m, \theta_m]^T$ is a *basis vector*, which represents a *basis plane* in the Euclidean 3-space E^3, $\mathbf{r} = [x, y, z, w]^T$ is the location vector with homogeneous coordinates, and μ_{lm} is the *periodic moment*. We usually assume $w = 1$ if not explicitly

specified. Each basis vector can be regarded as a set of parallel 2D subspaces in E^3, which plays an important role in interactive manipulation of PS models.

The locations of atoms or particles in the E^3 space can be determined by their simultaneous appearances in three or more subspaces defined by periodic surfaces, which we call loci surfaces. Finding the intersections among $\psi_1(\mathbf{r}) = 0$, $\psi_2(\mathbf{r}) = 0$, and $\psi_3(\mathbf{r}) = 0$ is to solve the constraint $\psi(\mathbf{r}) = \psi_1^2(\mathbf{r}) + \psi_2^2(\mathbf{r}) + \psi_3^2(\mathbf{r}) = 0$.

3. Basic Features

The basic features are the fundamental building blocks for complex structures. In crystallography, it is well known that there are fourteen unique Bravais lattices in three dimensions to represent basic crystal structures. All crystalline materials recognized until now (not including quasicrystals) fit in one of these arrangements. We consider these fourteen unique space lattices as basic features. By means of the intersection operation among three periodic surfaces, all of the fourteen basic features can be efficiently built.

The fourteen basic features are then grouped into seven categories which are cubic, orthorhombic, tetragonal, monoclinic, triclinic, rhombohedral and hexagonal. All of these basic features could be represented by intersections among three periodic planes in E^3 space, as illustrated in Fig 1. Transformation operations [3] on a single periodic surface, such as rotation, translation and scaling, can be applied to adjust positions.

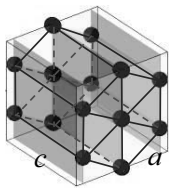

$$\cos^2(\pi(2x/\sqrt{3}a + 0.5)) + \cos^2(\pi y/c) + \cos^2(\pi(x/\sqrt{3}a + z/a + 0.5)) = 0, \quad a \neq c$$

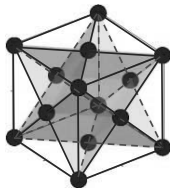

$$\cos^2(\pi(x+y+z)) + \cos^2(\pi(-x+y+z)) + \cos^2(\pi(-x-y+z)) = 0$$

Figure 1. Examples of basic feature created by the PS model

4. Feature Operations

In this section, we introduce some feature operations that allow us to rapidly locate particles and create complex crystal structures. The operations that are described here include masking, demasking, imposing and union.

4.1 Masking

It is known in crystallography that each lattice point of a Bravais lattice represents the same group of atoms which fit in one of fourteen Bravais lattices in a smaller scale. That is, each lattice point of Bravais lattices can be further expanded and becomes a unit of lattice itself. Therefore, we propose a masking operation to support such structure expansion.

Given basic features $\psi_{\mathrm{A}}(\mathbf{r}') = \psi_{11}^2(\mathbf{r}') + \psi_{12}^2(\mathbf{r}') + \psi_{13}^2(\mathbf{r}') = 0$ and $\psi_{\mathrm{B}}(\mathbf{r}') = \psi_{21}^2(\mathbf{r}') + \psi_{22}^2(\mathbf{r}') + \psi_{23}^2(\mathbf{r}') = 0$, the masking operation T_{mask} is defined as

$$T_{mask}[\psi_A(\mathbf{r}'), \psi_B(\mathbf{r}'), m](\mathbf{r}) := \psi_A(\mathbf{r}') + T_{sym}[T_{tran}[T_{scal}[\psi_B(\mathbf{r}'), m, m, m], \mathbf{r}]] \tag{2}$$

where m is the *mask index*. Masking operation expands each lattice point of basic feature $\psi_{\mathrm{A}}(\mathbf{r}')$ to the basic feature $\psi_{\mathrm{B}}(\mathbf{r}')$. Fig 2(a) illustrates the effect of masking operation. The operations of center symmetry T_{sym}, translation T_{tran}, and scaling T_{scal} are defined as

$$T_{sym}\left[\psi(\mathbf{r})\right] := \psi(\mathbf{S}_{sym}^{-1} \cdot \mathbf{r}) \tag{3}$$

$$T_{tran}[\psi(\mathbf{r}), \mathbf{r}_1] := \psi(\mathbf{r} - \mathbf{r}_1) = \psi(\mathbf{T}^{-1} \cdot \mathbf{r}) \tag{4}$$

$$T_{scal}[\psi(\mathbf{r}), s_x, s_y, s_z] := \psi(\mathbf{S}^{-1} \cdot \mathbf{r}) \tag{5}$$

where the 4×4 transformation matrices are $\mathbf{S}_{sym} = [-1,0,0,0;0,-1,0,0;0,0,-1,0;0,0,0,1]$ for symmetry, $\mathbf{T} = [1,0,0,t_x;0,1,0,t_y;0,0,1,t_z;0,0,0,1]$ with $\mathbf{r}_1 = [t_x \quad t_y \quad t_z \quad 1]$ for translation, and $\mathbf{S} = [s_x,0,0,0;0,s_y,0,0;0,0,s_z,0;0,0,0,1]$ for scaling.

4.2 Demasking

Given an original structure $\psi_{\mathrm{A}}(\mathbf{r}')$ and a mask feature $\psi_{\mathrm{B}}(\mathbf{r}') = \psi_{21}^2(\mathbf{r}') + \psi_{22}^2(\mathbf{r}') + \psi_{23}^2(\mathbf{r}') = 0$, a demasking operation is defined as

$$T_{dem}[\psi_{\mathrm{A}}(\mathbf{r}'), \psi_{\mathrm{B}}(\mathbf{r}'), m](\mathbf{r}) := \left\{\mathbf{r} \middle| \forall \mathbf{r}',\ T_{tran}[T_{scal}[\psi_{\mathrm{B}}(\mathbf{r}'), m, m, m], \mathbf{r}] = 0,\ \psi_{\mathrm{A}}(\mathbf{r}') = 0\right\} \tag{6}$$

where m is the demasking index. The operation of demasking collapses any of the feature $\psi_{\mathrm{B}}(\mathbf{r}')$ which is available in the structure $\psi_{\mathrm{A}}(\mathbf{r}')$ into a single lattice point. The demasking operation can be looked as the inverse operation of the masking operation. Fig 2(b) illustrates the effect of demasking operation.

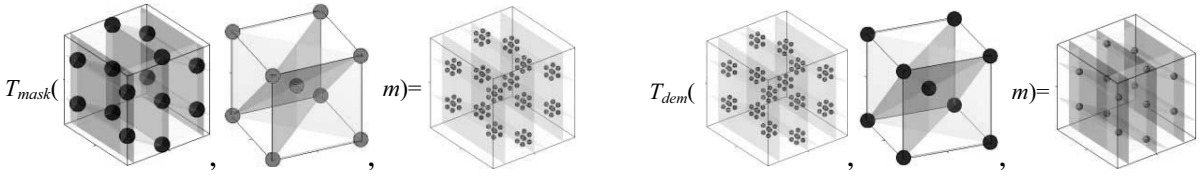

(a) (b)

Figure 2. Illustrations of masking and demasking operations. (a) Masking; (b) Demasking.

4.3 Impose

Given two basic features $\psi_{\mathrm{A}}(\mathbf{r}) = \psi_{11}^2(\mathbf{r}) + \psi_{12}^2(\mathbf{r}) + \psi_{13}^2(\mathbf{r}) = 0$ and $\psi_{\mathrm{B}}(\mathbf{r}) = \psi_{21}^2(\mathbf{r}) + \psi_{22}^2(\mathbf{r}) + \psi_{23}^2(\mathbf{r}) = 0$, the impose operation is defined as

$$T_{imp}[\psi_{\mathrm{A}}(\mathbf{r}), \psi_{\mathrm{B}}(\mathbf{r})] := \psi_{\mathrm{A}}(\mathbf{r}) \cdot \psi_{\mathrm{B}}(\mathbf{r}) \tag{7}$$

The impose operation overlaps one feature onto another. Fig 3 illustrates the construction of the diamond lattice by imposing a fcc feature onto a translated fcc feature.

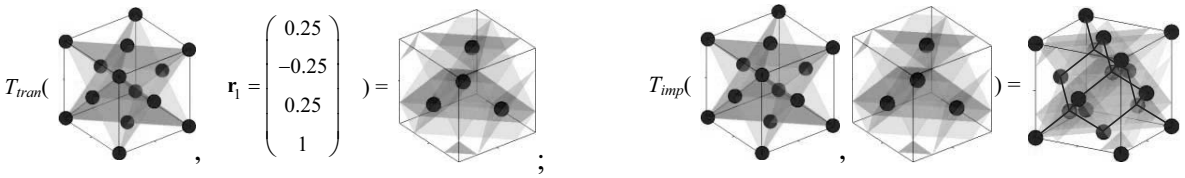

Figure 3. An illustration of construction of diamond structure based on fcc features

4.4 Union

If $\psi_C(\mathbf{r})$ is the face-centered basic feature in the same category as the basic features $\psi_A(\mathbf{r})$ and $\psi_B(\mathbf{r})$ ($\psi_A(\mathbf{r}) \neq \psi_B(\mathbf{r})$), the union operation is defined as

$$T_{un}[\psi_A(\mathbf{r}), \psi_B(\mathbf{r})] := T_{mask}[\psi_C(\mathbf{r}), T_{imp}[\psi_A(\mathbf{r}), \psi_B(\mathbf{r})], 2] \quad (8)$$

The union operation joins two basic features in the same category in a 3D periodic pattern, as illustrated in Fig 4(a). By union of two basic features, the two are joined together by sharing lattice positions on their edge cut surfaces. Fig 4(b) illustrates the effect of the union operation.

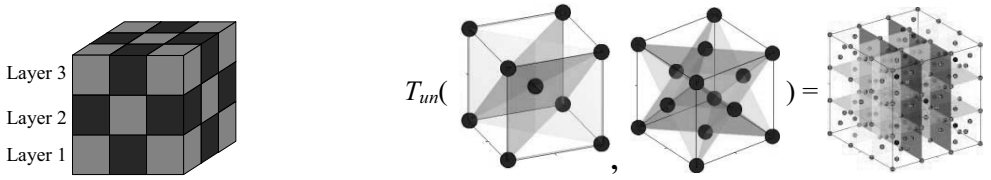

(a) (b)

Figure 4. An illustration of union. (a) Periodic 3D layout; (b) A bcc is unioned with a fcc

5. Summary

In this paper, we propose a rapid construction approach for crystal structures based on features. The basic features can be created by the aid of implicit PS models. Feature operations are defined to construct complex crystals from the basic features. The feature-based approach can help us to generate complex systems efficiently in an interactive CAND environment.

Acknowledgements

This work is supported in part by the NSF grant CMMI-0645070.

References

[1] Wang, Y., "Geometric modeling of nano structures with periodic surfaces", Lecture Notes in Computer Science, Vol.4077, 343-356, (2006)
[2] Wang, Y., "Periodic surface modeling for Computer Aided Nano Design", Computer-Aided Design, 39(3): 179-189, (2007)
[3] Wang, Y., "Loci periodic surface reconstruction from crystals", Computer-Aided Design & Applications, 4(1-4): 437-447, (2007)

Computational modeling of materials for electrical insulations

B. Singh and O. Fritz

ABB Switzerland Ltd. Corporate Research, Baden-Dättwil, CH 5405, Switzerland.
Bandeep Singh, Insulation and Polymer Technologies, Scientist,
(E-mail: bandeep.singh@ch.abb.com)
Oliver Fritz, Theoretical Physics, Group Leader, (E-mail: oliver.fritz@ch.abb.com)

ABSTRACT

With ever increasing demand from the market for performance and lower delivery times of electrical insulation materials, computational modeling is of great relevance. In the following, polymeric electrical insulation materials simulations by Quantitative Structure Property Relationship (QSPR), Molecular Dynamics (MD) and Density Functional Theory (DFT) are discussed. Commercially available codes like Synthia and Dmol3 from Accelrys Software Inc. were used to define and simulate polymeric systems. Experimental results were used to compare the results obtained by simulations. As a first step, variations of physical properties (like glass transition temperature (T_g), dielectric constants (ε), coefficient of thermal expansion (α), Young's Modulus (E) and thermal conductivity (k)) of Bisphenol A based epoxy, its mixture with Bisphenol F and their reacted states with hardeners and flexibilizers were simulated with Synthia (QSPR [1, 2]). These results showed good agreement with experimental observations. MD was used to calculate diffusivity coefficients of oxygen molecules through silicone rubber. Finally, a study by quantum mechanical DFT simulations of epoxy [3] reaction using different catalyst molecules was carried out to understand the effectiveness of different catalyst (for the same resin system). This was done by analysing heights of energy barriers of different polymeric reaction steps.

Keywords: Epoxy; QSPR; Synthia; Dmol3; Density functional theory (DFT)

[1]. A. Liu, X. Wang, L. Wang, H. Wang, and H. Wang, Prediction of dielectric constants and glass transition temperatures of polymers by quantitative structure property relationships. European Polymer Journal, 2007. **43**: p. 989.
[2]. X. Yu, Z. Xie, B. Yi, X. Wang, and F. Liu, Prediction of the thermal decomposition property of polymers using quantum chemical descriptors. European Polymer Journal, 2006. **43**: p. 818.
[3]. I. Yarovsky and E. Evans, Computer Simulation of Structure and properties of crosslinked polymers: application to epoxy resins. Polymer, 2002. **43**: p. 963.

Density Matrix Treatment of Confinement-Facilitated Photovoltage in Thin Films of Silicon

Dmitri Kilin[1], David Micha[1], David Micha[2]

[1]QTP, University of Florida, FL, USA (E-mail: dkilin@gmail.com)
[2]Dept of Physics, University of Florida, FL, USA

ABSTRACT

The time dependent reduced density matrix (TDRDM) method provides a rigorous description of the evolution of electronic densi- ties and optical response at a surface of a semiconductor thin film. Here, a TDRDM-based computational procedure is applied to calculate the voltage between the surface and inner layers of a nano-width semiconductor (Si) thin film elec- tronically excited absorption of light at different frequencies. We use the steady state solution of the equation of motion for the TDRDM. The surface of the film is formed by (111) face of Silicon with H-terminated dangling bonds. We have found that a change in the thickness of the film changes the the frequency at which the photovoltage reaches maximal value. We attribute this effect to the quantization of Kohn-Sham orbitals along the direction perpendicular to the film surface. Our treatment can be implemented for a wide class of photo-electronic materials relevant to solar energy capture. For example, applications to clusters of Ag atoms on Si(111):H changes the sign of the calculated photovoltage versus incident photon energies

Nucleation Rate Surfaces for Modeling of Nanomaterial Generation from Crystals under Short Pulses of Energy

Michael P. Anisimov, Anatoly M. Baklanov, and Artyom V. Trilis

Institute of Chemical Kinetics&Combustion SB RAS, 3 Institutskaja Street, 630090 Novosibirsk, Russia
(E-mail: anisimovmp@mail.ru)

ABSTRACT

The nucleation rate surface using is a new promissing tool for computer modeling of nanomaterial generation from crystals under short pulses of energy. A nucleation rate surface design over a diagram of phase equilibria is used for geometrical presenting of nanosize particle generation under short pulses of energy. Nanoaerosol which is appeared from melted wire under powerful electric pulse or laser ablation, milling of crystals, etc can be mentioned as examples. Particle generation kinetics are investigated experimentally and theoretically. Nevertheless one might say that nucleation rate surface topologies for the gas and liquid embryo generation kinetics are not fully understood up to now. The nucleation rate surface topologies for metastable crystal relaxation kinetics are considered in the present research.

1. Introduction

Computer modeling of the nanosize particles generation kinetics can be realized using any parametric model. These kinds of models can be applied for the frames of the parameterization areas as a rule. A model using beyond the parameterization intervals can be successful in the case of physically true parameterization only. Using the nucleation rate surface topologies gives chance to raise the modeling reliability. There are a lot of the experimental and theoretical investigations of melting and boiling kinetics in application to solid (crystalline or glassy) materials with evaporation and aerosol formation following then. As examples can be mentioned the conducted wires which can blow up under electrical current [1], the laser ablation of crystals [2], *etc*. Nevertheless the nucleation rate surface topologies for the gas and liquid embryo production from metastable crystals are do not enough understood up-to now. Case of topologies for metastable crystal relaxation kinetics is considered in the present research.

2. Nucleation Rate Surface Semiempirical Design. Results and Discussion

The nucleation rate surface topology for embryo-forming under the laser ablation is considered on the base of simplified PT phase diagram with triple point shown in Fig. 1, following article [3]. Where P is total pressure, T is temperature, and J is nucleation rate. The nucleation rate surfaces for droplet and vapor embryos are shown schematically. Surfaces overlap each other in

interval between metastable critical points which are signed by c_1 and c_2. Several assumptions are used to design of the nucleation rate surfaces, i.e. nucleation rate along the phase equilibrium

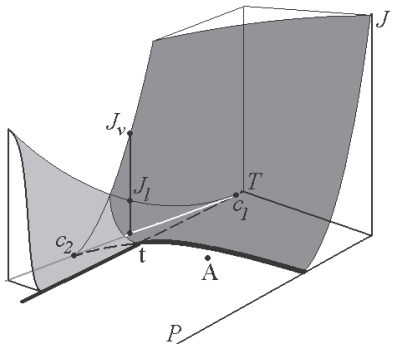

Fig. 1. Topology of nucleation rate surfaces over *PT* phase diagram for droplet formation (gray) and vapor embryo formation (dark gray) from crystal or glass. Point, **t,** is triple one.

lines has zero values. The maximum nucleation rates are achieved at the spinodal conditions. It is assumed that nucleation rate surface is represented by continuous and monotonous function for one given phase state. Nucleation rate at the critical points has zero value because these points are representing the second order phase transitions where two different phase coexistence is impossible.

The initial state of crystal is marked schematically by letter A. In case of a crystal-vapor or crystal-liquid equilibria the initial state point is located on the appropriate line of phase equilibria. A laser pulse produces temperature and pressure growth at the spotlight crystal layer. Crystal under fast heating may reach the spinodal conditions where droplets and vapor embryos have barrier less nucleation. The droplet nucleation rate is associated with surface which arises from line for crystal melting. The spinodal droplet nucleation rate, J_l, in Fig. 1 is shown at condition governing by the total energy of laser beam pulse. Nucleation rate, J_v, is associated with the vapor embryo generation at the crystal-vapor spinodal condition.

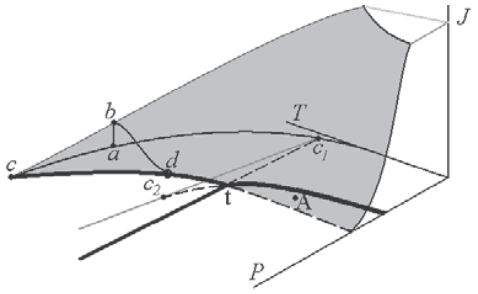

Fig. 2. The simplified PT phase diagram following article by Anisimov *et al*. [3].

One can find in Fig. 1 that the vapor embryos generation can be detected only at low enough pressure within a spot of laser beam pulses. Droplets generation can be found in addition to vapor generation at more powerful laser radiation and lower total pressure. Energy growth for laser beam pulses result pressure growth as well as the relative droplet contains following the

nucleation rate surface topology for liquid embryos. Sublimation mechanism disappears at some high enough density of laser pulse energy. I.e. the vapor generation becomes the ability to be produced in that case in the result of droplet evaporation only. The schematic topology for the vapor nucleation rates in liquid (or droplets) is presented in Fig. 2. Droplets can reach the spinodal conditions for liquid when laser pulse energy is enough. That case is discussed in review [1]. The vapor nucleation rate gets the maximum value at the spinodal conditions, when the laser pulse radiation become over then vapor gets supercooled and generates droplets, nanocrystals and nanoglasses. For example, Buckle at al. [4] gets the amorphous and crystal particles from Zn vapors. Non-evaporated droplets should grow under the vapor cooling then freeze to the crystal or glassy particles. Seemingly the nucleation surface topology for glasses should continue a surface for droplet nucleation which is shown in Fig. 3.

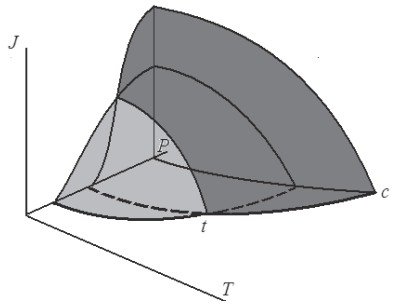

Fig. 3. Topology for droplet (dark gray) and crystal (gray) particles nucleation.

The particle size distributions as function of the power of laser pulse is measured on the example of Polymethyl Methacrylate laser ablation. We used here a rate difference for size gain in a supersaturated vapor media for the different particle phase states.

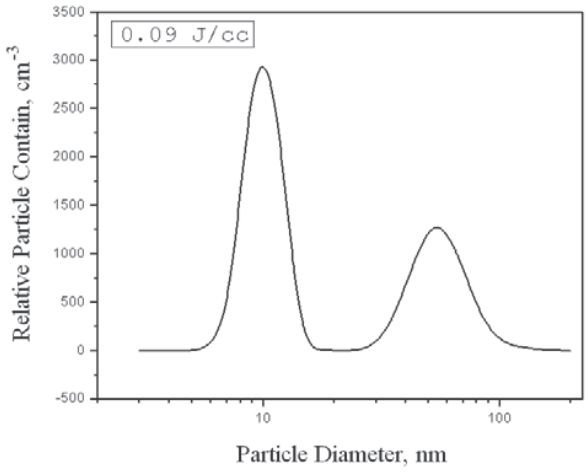

Fig. 4 The particle size distribution at laser beam intensity of 0.09 J/cc.

In Fig. 4 one can see the typical particle size distribution which are observed at three values of the power of laser pulse, i.e. 0.03; 0.09, and 0.13 Joule per cc. A clear bimodal particle size distribution is observed. That result illustrates qualitatively true bridging with topologies shown

in Fig. 1. Each size distribution is measured by means of Diffusion Aerosol Spectrometer [5]. It is apeared that low energy (0.03 j/cm^2) beam produce one mode size distribution. It is reasonable to assume that the mode is associated with supersaturated vapor nucleation which generates near 10 nm (solid) particles the result of solid Polymethyl Methacrylate sublimation under laser pulse. The bigger in energy laser pulse have chance to create the pressure in the light spot area which is enough to make phase transition from solid to liquid states in detectable quantity. Well known that according the phase state diagram at temperature which is upper the triple point the target substance has chance to be in the vicinity of parameters associated with transition of solid to liquid. That situation can be seen in Fig. 1 and it is reason to get melted Polymethyl Methacrylate as well as the mode for droplets at higher energy density for laser beam. One can see in Fig. 4 the second mode associated with droplets.

3. Conclusions

According the nucleation rate surface topology (shown in Fig. 1) the simultaneous vapor and liquid phase formation under laser ablation of crystalline matter is possible at pressures between metastable critical points for vapor-crystal and negative pressure crystal-liquid equilibria. Only vapor phase can be generated down in pressure from the crystal-liquid critical point at negative pressures. Only droplets can be formed under laser ablation at pressure over vapor-crystal critical point. The droplets can be evaporated at that conditions than, i.e. vapor phase can be generated in two-step process in that case. Experiments on laser ablation of Polymethyl Methacrylate illustrate the reasonable agreement with semiempirical consideration.

4. Acknowledgements

Research is under support of the Russian Foundation for Basic Research through grant numbers of 07-08-13529-ofi and 07-03-00587-a.

5. References

[1] M.M. Martynyuk, “Phase explosion of a metastable liquid”, Phys. Combust. Explosions, **13**(1), 178 -184 (1977).
[2] Q. Lu, S.S. Mao, X. Mao, and R.E. Russo, “Delayed phase explosion during high-power nanosecond laser ablation of silicon”, Appl. Phys. Letters, **80**(17), 3072-3074 (2002).
[3] M.P. Anisimov, P.K. Hopke, D.H. Rasmussen, “Relation of phase state diagrams and surfaces of new phase nucleation rates”, J. Chem. Phys., **109**(4), 1435-1444 (1998).
[4] E.R. Buckle, K.J.A. Mawella, P. Tsakiropolous, “Particle condensation in the vapor emitted by a heated source“, J. Colloid Interface Sci. **112**, 42 (1986).
[5] R.A. Mavliev, A.N. Ankilov, A.M. Baklanov, B.Z. Gorbunov, N.A. Kakutkina, K.P. Kutsenogiy, S.E. Paschenko, V.I. Makarov, Kolloidn. Zh. (Russian), “Application of screen diffusion battery for determination of the aerosol dispersity“, **46**(6), 1136-1138 (1984).

Computational Design of Refractory Alloys for Fossil Energy Applications

Michael C. Gao[1,2], Ömer N. Doğan[1], Paul King[1]

[1]National Energy Technology Laboratory, Albany, OR 97321, USA
[2]Parsons, P.O. Box 618, South Park, PA 15129, USA
(E-mails: mcgao07@gmail.com, Omer.Dogan@netl.doe.gov, Paul.King@netl.doe.gov)

ABSTRACT

There is an urgent need to develop structural alloys with desirable properties (e.g. high strength, good ductility, excellent creep and corrosion resistance) using refractory elements of high melting points for applications of new technologies such as oxy-fuel gas turbines, hydrogen turbines, syngas turbines, etc. The purpose of this work is to develop next-generation structural alloys for high-temperature applications ($\geq$1150^{o}C) in fossil energy systems. Cr is selected as a model system to demonstrate our integrated design methodology because Cr based alloys show considerable promises due to (i) the relatively low cost, (ii) the relatively low density and (iii) good high temperature strength. However, there are important challenges with use of Cr and other refractory metals: low ductility and fracture toughness at room temperature are the most significant issues that need to be dealt for important structural applications. Our strategy is to perform extensive first-principles calculations to identify ductilizing elements [1] and appropriate strengthening 2nd phase to guide experiments. Gibbs energy data computed from first principles calcualtions will be used as inout to CALPHAD modeling.

[1] M.C. Gao, Ö.N. Doğan, P. King, A.D. Rollett, and M. Widom, JOM , **60**, 61 (2008).

This technical effort was performed in support of the National Energy Technology Laboratory's on-going program in advanced materials research under the In-House Project 220691 and the RDS contract DE-AC26-04NT41817, and Pittsburgh Supercomputing Center with Grant No. DMR070016P and Teragrid Grant No. DMR070065N.

Multi-scale sensitivity analysis for design of polycrystalline materials with tailored properties

Veera Sundararaghavan

Department of Aerospace Engineering
3025 FXB building, 1320 Beal Ave, University of MichiganAnn Arbor, MI 48109
(Ph: 734 6157242, E-mail: veeras@umich.edu)

ABSTRACT

Material property evolution during processing is governed by the evolution of the underlying microstructure. We present an efficient technique for tailoring texture development and thus, optimizing properties in forming processes involving polycrystalline materials. The deformation process simulator allows simulation of texture formation using a continuum representation of the orientation distribution function. An efficient multi-scale sensitivity analysis technique is then introduced that allows computation of the sensitivity of microstructure field variables such as slip resistances and texture with respect to perturbations in macro-scale forming parameters such as forging rates, die shapes and preform shapes. These sensitivities are used within a gradient-based optimization framework for computational design of material property distribution during metal forming processes. Effectiveness of the developed computational scheme is demonstrated through an example that addresses control of yield strength in a closed-die forging process.

1. Introduction

Current practice in materials-by-design has evolved from trial and error approaches to physically-based approaches where computational techniques are used extensively in the design of new materials. A technique for optimizing properties of polycrystalline alloys involve tailoring of preferred orientation of crystals manifested as a first order property of the microstructure, namely the crystallographic texture. Several applications exist where certain textures are desirable to improve properties of materials. For example, a Goss texture is desirable in transformer cores to reduce power losses during magnetization. During forming processes, mechanisms such as crystallographic slip and lattice rotation drive the formation of texture and variability in property distributions in such materials. An useful method for designing materials is hence, through control of deformation processes leading to formation of textures that yield desired property distributions. This inherently is a computationally complex multi-scale problem requiring extensive use of parallel computing. This paper presents an efficient sensitivity analysis technique to design materials through control of process variables such as die and preform shapes. The framework developed in our earlier publications [1] is extended to address optimization problems for polycrystalline materials. Evolution of the micro-scale during forming is modeled using continuum representation of texture [2] and incorporates crystal elasto-viscoplasticity through the constitutive equations of Kothari and Anand [3].

2. Overview of the Multiscale Problem

In the multiscale problem, the texture evolution is modeled by an orientation distribution function (ODF) at each of the material points of the macro-continuum (see Fig. 1).

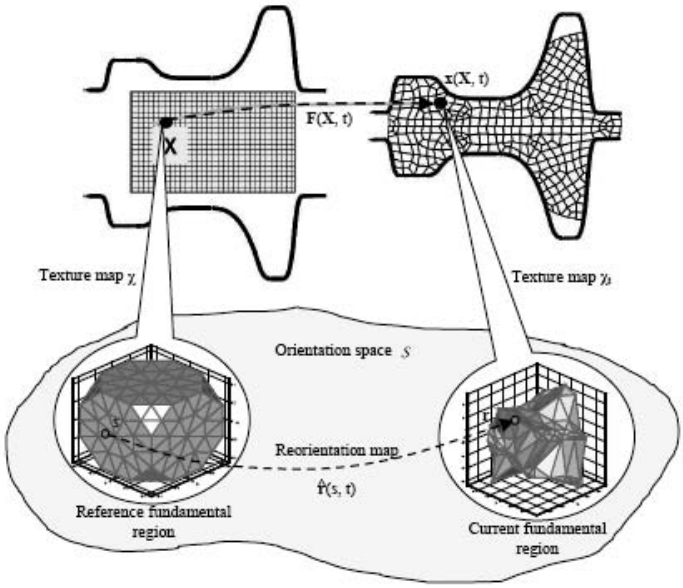

Figure 1. A Multi-scale Lagrangian Framework for describing polycrystalline texture evolution at a material point

The ODF, represented as $A(r)$, describes the crystal density over the fundamental region (***r***). The Lagrangian version of the conservation equation is used to model the micro-scale texture evolution, and is defined as

$$\hat{A}(s,t)J(s,t) = \hat{A}(s,0) = A_o(s) \qquad (1)$$

where $J(s,t) = \det(\nabla \hat{r}(s,t))$ is the Jacobian determinant of the re-orientation of the crystals and $\hat{A}(s,0) = A_o(s)$ is the ODF associated with the reference fundamental region (***s***) and can be thought of as the initial texturing of the material. The polycrystal average of an orientation dependent property, $\gamma(r,t)$, is determined as:

$$< \gamma >= \int_{R_t} \gamma(r,t)A(r,t)dv_t = \int_{R} \gamma(\hat{r}(s,t),t)A_o(s)dv \qquad (2)$$

where dv_t is defined as the volume element on the current Rodrigues fundamental region. The slip and re-orientation occur in an ordered manner such that a preferential orientation or texture develops. In the macro-scale, the equilibrium equation is expressed on the reference configuration as:

$$\nabla_o . < P > + f = 0 \qquad (3)$$

where $\nabla_o .$ represents the divergence in the reference/initial configuration (total Lagrangian approach). The polycrystal average Piola-Kirchhoff-I stress, $< P >$ is computed using the Taylor hypothesis for the macro-micro linking assumption. A Newton-Raphson iterative scheme along with a line search procedure is employed in the finite element solver to compute the macro-deformation.

3. Multiscale Design Problem

The objective function for the design problems are minimized using a gradient optimization framework where the gradients of the objective function are calculated from the sensitivities computed in the sensitivity problem. We compute these sensitivities by direct differentiation of the multiscale model described in the previous section, using the continuum sensitivity method. The sensitivities of deformation fields expressed in an updated Lagrangian (UL) framework as described in detail in [2]. The process of evaluating the sensitivities of fields on the micro-scale due to perturbations on the macro-scale requires a macro-sensitivity problem where the interest is to compute how perturbations on the macro-design variables β affect the deformation gradient F at the micro scale. The micro-sensitivity problem computes the resulting variation of the ODF and other microstructural properties from the perturbation ΔF of F. Sensitivities at the macro- and micro- scales are linked using the Taylor hypothesis. The polycrystal average of micro-scale sensitivity fields are determined as follows

$$< \overset{o}{\gamma} >= \int_R \overset{\hat{}}{\overset{o}{\gamma}}(s,t;\beta) A_o(s) dv \qquad (4)$$

where dv is defined as the volume element on the reference fundamental region and it is assumed that the initial texture is fixed (i.e. $\overset{o}{A}_o = 0$). Described below is the analysis for the development of a total Lagrangian sensitivity formulation for the kinematic problem. The design differentiation of the equilibrium equation (for the macro-scale problem) results in:

$$\overline{\nabla_o . \overset{o}{< P >}} + \overset{o}{f} = 0 \qquad (5)$$

The finite element discretization of the weak form of the above equation results in a linear system that can be efficiently solved (computational aspects explained in Ref [2]). In order to solve the weak form, relationship between $\overset{o}{< P >}$ and $[\overset{o}{F}, \overset{o}{\theta}]$ is required and is obtained by differentiating the constitutive equations in [3] with respect to the design variable.

4. Numerical Examples

In this problem, the simulation of forging of a OFHC copper preform with a slip system hardening model [3] is considered. The primary objective is to design the preform for a final forged product (with fixed stroke) such that the die cavity is fully filled. The secondary objective in this problem is to minimize the variation of yield strength on the curved surface of the final product.

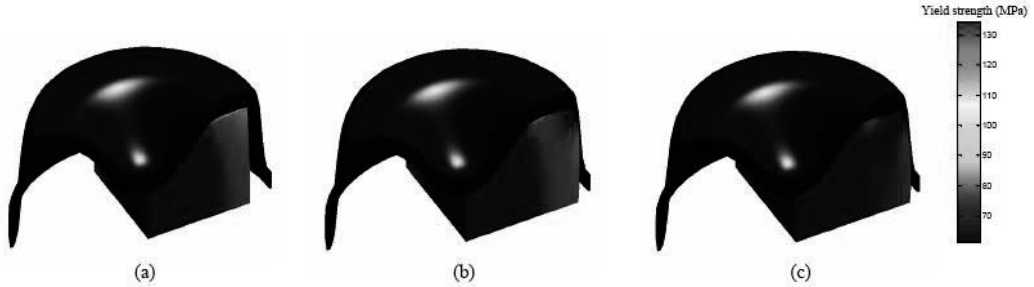

Figure 2. Final configuration at the end of forging in the (a) first iteration (b) second iteration (c) final iteration

Initial surface of the preform is represented with a degree 6 Bezier curve defined with 6 independent design variables. Mathematical model of the die/preform shapes and problem parameters are taken from [2]. The efficiency of the algorithm is exemplified by the realization of design objectives (complete die cavity fill and uniform yield strength) within 7 iterations. The amount of filling of die cavity and yield strength distribution on the curved surface at the end of forging at the first, second and final iteration are shown in Fig. 3 and Fig. 4 respectively.

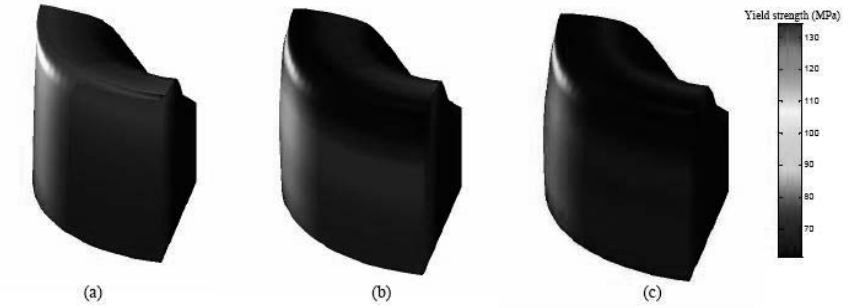

Figure 3. Yield strength distribution on the curved surface at the end of forging at the (a) first iteration (b) second iteration (c) final iteration

Acknowledgements
The work was completed in the Materials Process Design and Control Laboratory, Cornell University (Director: Prof Nicholas Zabaras) with financial support from the Army Research Office (Dr. David Stepp, Program Manager).

References

[1] V. Sundararaghavan and N. Zabaras, "Design of Microstructure-sensitive Properties in Elasto-viscoplastic Polycrystals using Multi-scale Homogenization", International Journal of Plasticity, **22**, 1799(2006).
[2] V. Sundararaghavan and N. Zabaras, "A Multi-length Scale Continuum Sensitivity Analysis for the Control of Texture-dependent Properties in Deformation Processing", International Journal of Plasticity, **24**, 1581(2008).
[3] L. Anand, M. Kothari, „A computational procedure for rate-independent crystal plasticity“, Journal of the Mechanics and Physics of Solids, **44(4)**, 525(1996).

Multiphase Material Modelling by Multiscale Particle-In-Cell Method

S. Alireza Asgari[1], Chunhui Yang[2], Peter D. Hodgson[1], Bernard F. Rolfe[2]

[1]Centre for Material and Fibre Innovation, Deakin University, Waurn Ponds 3217, Australia (E-mail: asgari@deakin.edu.au)
[2]School of Engineering and IT, Deakin University, Waurn Ponds 3217, Australia.

ABSTRACT

A particle-based method for multiscale modeling of multiphase materials such as Dual Phase (DP) and Transformation Induced Plasticity (TRIP) steels has been developed. The multiscale Particle-In-Cell (PIC) method benefits from the many advantages of the FEM and mesh-free methods, and to bridge the micro and macro scales through homogenization. The conventional mesh-based modeling methods fail to give reasonable and accurate predictions for materials with complex microstructures. Alternatively in the multiscale PIC method, the Lagrangian particles moving in an Eulerian grid represent the material deformation at both the micro and macro scales. The uniaxial tension test of two phase and three-phase materials was simulated and compared with FE based simulations. The predictions using multiscale PIC method showed that accuracy of field variables could be improved by up to 7%. This can lead to more accurate forming and springback predictions for materials with important multiphase microstructural effects.

1. Introduction

Research on Advanced High Strength Steels (AHSS) has been stimulated by the need to understand how their complex microstructures affect what happens at a larger scale, particularly in a metal forming or a crash scenario. At present the AHSS grades of most interest to the automotive industry are the Dual Phase (DP) and TRansformation Induced Plasticity (TRIP) steels. However, there are difficulties in predicting the behaviors of these multiphase steels, which has led to hurdles in their implementation. The Finite Element (FE) method has proven to be successful in predicting strain and thickness after forming [1].

However, when a stress history dependent process, such as springback phenomenon is studied, the conventional FE methods do not provide an accurate prediction, particularly for complex shapes. The main disadvantage of the FEM, when formulated in a Lagrangian frame, arises from mesh related problems. For large deformations, the mesh can distort and severely affect the accuracy of the calculations. Remeshing restores the proper shape of the elements, but it may introduce additional errors due to the mapping of the distorted mesh to the newly generated one. All of these problems are inherently carried over when a multiscale analysis is performed by the multilevel finite element technique. In such cases, the mesh related issues will be more significant in the microscale analyses where localized large deformations are involved.

The particle-based methods have been developed to offer on an alternative approach to model the large deformation problems of multiphase materials. Among the particle-based or meshless methods, the Particle-In-Cell (PIC) method, also known as the Material Point Method (MPM), has been applied successfully to problems in solid mechanics by Sulsky *et al.* [2]. The PIC method takes the advantages of the Lagrangian FE method and combines it with the advantages of the Eulerian description of motion. The computational mesh can be defined in an arbitrary manner. Therefore, the problem of mesh distortion can be avoided. The material points carry the material history while the equations of motion are formulated and solved on a regular grid.

With the many advantages offered by the PIC method, this research aims to develop and examine a multi level PIC framework, similar to the so-called multi-level FEM. The purpose of formulating the multiscale particle-based method was to model the mechanical response of the multiphase materials such as the DP and TRIP steels both at the micro and macro scales. The main difference between the multiscale PIC and FEM is the integration approach to build the macroscale global stiffness matrices. In this paper, the adaptive and iterative approach outlined in the numerical implementation of Moresi *et al.*[3] was used.

2. Unit cell setup

Some observations of the performance of the multiscale PIC method are presented in the following sections. Two geometrically different unit cells were created and used to model a tensile test with both the multiscale PIC and FEM (see Fig. 1). The material properties for the constituent phases, as shown in Fig. 1, were taken from the literature [4]. The constitutive relations were calculated by the inverse approach to produce less than 1% error in the prediction of the effective initial yield stress of the DP and TRIP steels with the multiscale FE method. The volume fractions of phases were calculated from image processing of several micrographs of the steels at a magnification of 2000X. Periodic boundary conditions (BC) were applied on the side walls of the unit cells. The convergent unit cell size was found from comparison of the periodic BC with the displacement and traction BCs (10 μm).

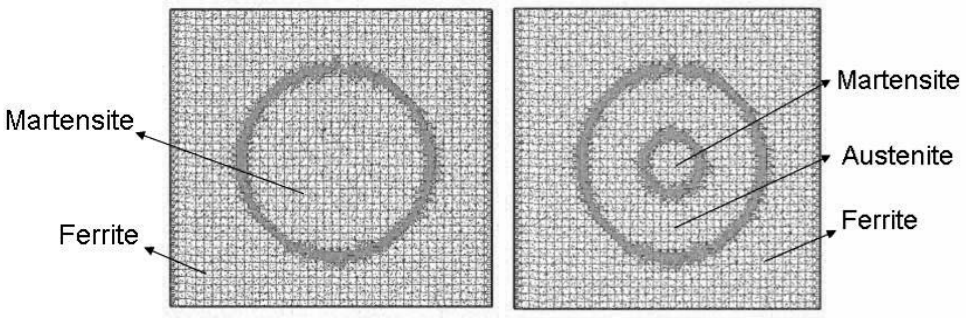

Figure 1. Mesh and particle overlay in the unit cell models for the DP (left) and the TRIP steels (right).

3. Results and discussion

The per-phase stress and strain distribution predicted by the multiscale PIC method is shown in Fig. 2 for the DP and TRIP steel microstructures. The predicted effective stresses were normalized by the initial yield stress of the soft ferrite phase for comparison with the FEM. In both cases of the dual phase and triple phase microstructure, the soft ferrite phase strained to much higher values whereas the harder phases (martensite and austenite) had higher stress localization at lower localized strain.

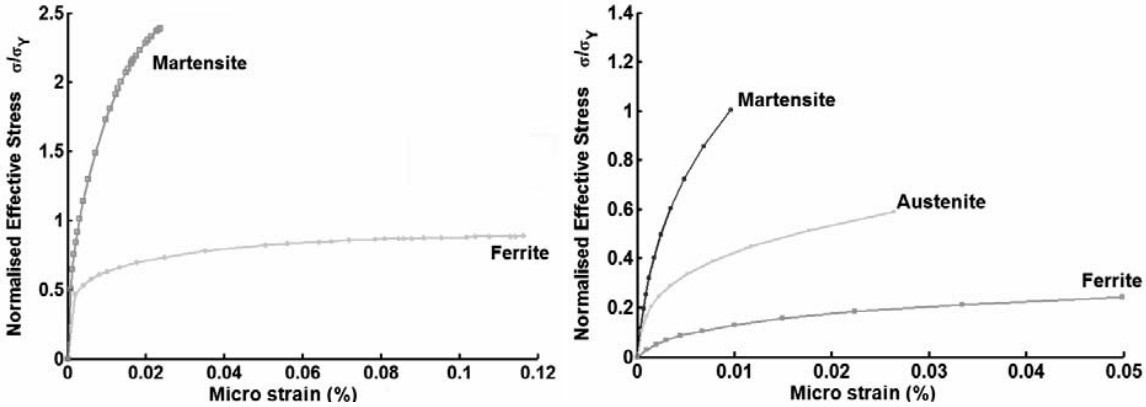

Figure 2. Stress and strain partitioning in the unit cell models for the DP (left) and TRIP steels (right) from the PIC method at microscale.

The effective plastic stress at the macroscale was found from the volume averaging of the unit cells from both the FE and the PIC methods and plotted against the experimental values from tensile tests. This is shown in Fig. 3 for the TRIP steel. The errors in the prediction of effective stress from multiscale PIC and FEM were computed with respect to the experimental yield stress of the steels (see Fig. 3).

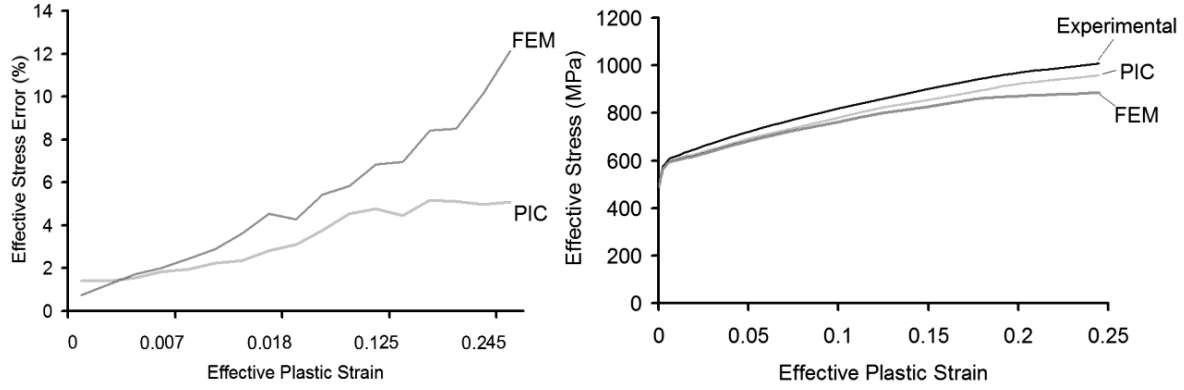

Figure 3. Effective stress prediction of the FEM and PIC method (left) and corresponding error with respect to the experimental target values (right).

The overall predictions of PIC and FEM were in close agreement in the elastic region. In the initial stages of the plastic deformation FEM outperformed PIC, giving lower error in the

effective stress prediction. However, as the deformation increased to higher strains, the error in effective stress predictions increased at a greater rate in the FE model. At the largest possible deformation, the multiscale FEM produced up to 12% error in stress predictions, whereas multiscale PIC method had only up to 5% error. Therefore, the multiscale PIC method proved to be more robust and accurate than the FE method for large plastic deformations. Such improvement in the performance has been observed by Więckowski [5] for single macro scale large strain engineering problems. Nonetheless, the improved accuracy of the PIC method comes at a higher computational time requirement compared to FEM. This is the greatest disadvantage of the multiscale PIC method, which needs further improvement and enhancement in the future.

4. Conclusion

The stress and strain partitioning in the microstructure of multiphase materials were modeled by the Particle-In-Cell (PIC) method in a multiscale framework. In the plastic region the per-phase stress and strain partitioning predicted by the two methods were in close agreement. However, there was a 7% improvement in the accuracy of the PIC predictions at large deformations. This is particularly important in subsequent simulations such as the springback process, where material and stress history dependent predictions are of interest. In such cases, any small amount of improved accuracy, as achieved by the PIC method, could contribute in improving the final predictions of the simulations of multiphase materials.

Acknowledgements

The authors acknowledge the financial support from the Australian Research Council (ARC) through the Federation Fellowship of P. D. Hodgson.

References

[1] S.A. Asgari, M. Pereira, B.F. Rolfe, M. Dingle, P. Hodgson, “Statistical analysis of finite element modelling sheet metal forming and springback analysis”, J. of Mat. Proc. Tech., 203 (2008) 129-136.

[2] D. Sulsky, S.J. Zhou, H.L. Schreyer, “Application of a particle-in-cell method to solid mechanics”, Comp. Physics Comm., 87 (1995) 236-252.

[3] L. Moresi, F. Dufour, H.B. Muhlhaus, “A Lagrangian integration point finite element method for large deformation modeling of viscoelastic geomaterials”, J. Comp. Physics, 184 (2003) 476-497.

[4] P.J. Jacques, Q. Furnemont, S. Godet, T. Pardoen, K. Conlon, F. Delannay, “Micromechanical characterisation of TRIP-assisted multiphase steels by in situ neutron diffraction”, Phil. Mag., 86 (2006) 2371-2392.

[5] Z. Więckowski, “The material point method in large strain engineering problems”, Comput. Methods Appl. Mech. Engrg., 193 (2004) 4417-4438.

Robust Simulation-Based Design of Materials

David McDowell

Georgia Institute of Technology, Altanta, GA, USA
(E-mail: david.mcdowell@me.gatech.edu)

ABSTRACT

Design has traditionally involved selecting a suitable material for a given application. Presently, a materials design revolution is underway in which the classical materials selection approach is replaced by design of material microstructure or mesostructure to achieve certain performance requirements, subject to constraints on other properties such as density, strength, conductivity, etc. Computational materials science and multiscale mechanics models play key roles in evaluating performance metrics necessary to support materials design. The interplay of hierarchical systems-based design of materials with multiscale modeling methodologies is at the core of materials design. Components of a practical approach for designing materials to achieve specified functionality are presented. In high performance alloys and composite materials, maximum performance is often achieved within a relatively narrow window of processing and resulting microstructures. The notion of mappings of accessible states of microstructures that link microstructure configuration to resulting properties is considered, and is further augmented with the notion of feasible states, which relates to thermodynamic microstructure admissibility via nonequilibrium processes and kinetics. An hierarchical approach is suggested in which subsystems (e.g., microstructure attributes) are identified and simulated using models at various levels of idealization to undertake parametric calculations that establish sensitivity of performance to microstructure. The need for multiscale models of microstructure-property relations (in space and time) will be discussed, with some discussion of model utility. Various schemes for multiscale modeling are considered, with distinction between needs and goals of hierarchical and concurrent multiscale models. The materials design approach advocated here invokes the notion of robust design, which is related to sensitivity of the desired response to various sources of uncertainty (material stochasticitiy, models and model parameters, process and loading histories, etc.) rather than seeking to optimize a single objective function. This is motivated as well by the need to consider multiple, conflicting performance requirements, often in different physical regimes of behavior. We discuss elements of suitable frameworks of decision-based design theory and examples of microstructure-sensitive hierarchical models for material structure-property relations that can effectively support preliminary design exploration.

Systems Computational Design of Hierarchically Structured Materials

G.B.Olson

Northwestern University, Department of Materials Science & Engineering, 2220 Campus Drive, Suite 2019, Evanston, IL 60208
(E-mail: g-olson@northwestern.edu)

ABSTRACT

A systems approach integrates processing/structure/property/performance relations in the conceptual design of multilevel-structured materials. Using examples of high performance alloys, numerical implementation of materials science principles provides a hierarchy of computational models defining subsystem design parameters which are integrated via computational thermodynamics in the comprehensive design of materials as interactive systems. Recent initiatives integrate materials science with quantum physics and applied mechanics, and address the acceleration of the full materials design, development and qualification cycle. The ongoing ONR/DARPA "D3D" Digital Structure Consortium initiative combines a suite of multiscale 3D tomographic characterization tools supporting higher fidelity 3D microstructural simulators for greater accuracy of predictive-science-based design in Fe-based and Ti-based alloy systems. Our latest design features a precipitation-strengthened austenitic TRIP steel demonstrating exceptional blast protection performance.

Design and Performance Modeling Tools for Solid Oxide Fuel Cells

Moe Khaleel

Pacific Northwest National Laboratory, Richland, WA, USA
(E-mail: moe.khaleel@pnl.gov)

ABSTRACT

The presentation focuses on a unique new software product developed at Pacific Northwest National Laboratory (PNNL) for accelerating the development cycle of Solid Oxide Fuel Cells (SOFC). SOFC-MP™ (Solid Oxide Fuel Cell-Multi-Physics) is the first fuel cell design software that allows engineers to "build, test, break, and fix" virtual fuel cells on their desktop computers. SOFC-MP makes it possible to simulate the fuel flow, electrochemical reactions, heat, and stress that solid oxide fuel cells (SOFCs) experience during actual operation. The "virtual prototype" generated using this ingenious tool will save manufacturers millions of dollars and incalculable amounts of time because it accelerates the design process by orders of magnitude and drastically reduces the need to build and test physical prototypes. SOFC-MP simulates exactly the complex relationships among flow, temperature, and mechanical components so that reliable, efficient SOFCs can be developed to generate power for industry, homes, automobiles, military fighting vehicles, and other potential applications.

Computational Materials Design of Solid State Fuel Cell Electrodes

Dongsheng Li, Hamid Garmestani

School of Materials Science and Engineering, Georgia Institute of Technology
(E-mails: dongsheng.li@mse.gatech.edu, hamid.garmestani@mse.gatech.edu)

ABSTRACT

This research work concentrated on materials design of solid state fuel cell electrodes to achieve better performance. Multiple requirements, which sometimes are conflict to each other, require understanding on the relationship between microstructure, properties and processing. Transport property and electrical property were investigated in fuel cell fabricated by spray pyrolysis. Statistical continuum mechanics was applied to model the properties from a gradient porous microstructure. It is applied in inverse materials design to guide the processing of fuel cell electrodes.

Computing electrochemical impedance of solid electrolyte from fluctuations

Eunseok Lee[1], Wei Cai[1], and Fritz B. Prinz[1,2]

[1]Mechanical Engineering Department, Stanford University, Stanford CA 94305;
[2]Materials Science and Engineering Department, Stanford University, Stanford CA 94305
(E-mail: euniv@stanford.edu)

ABSTRACT

We present a new method for computing the electrochemical impedance of solid electrolyte from kinetic Monte Carlo (kMC) simulations of charge diffusion. In the conventional approach, the impedance at a given frequency is obtained by a non-equilibrium kMC simulation subjected to an AC voltage at this frequency. Using the fluctuation-dissipation theorem, the impedance at all frequencies can be obtained from the correlation function of microscopic current fluctuations through a single equilibrium simulation. Our efficient method enables us to obtain the overall impedance and infer the governing mechanisms of ionic diffusion by analysis of the equivalent circuit. We observe the existence of optimal doping concentration to provide maximum conductivity and quantify two competing factors which determine the total conductivity. The effect of local microstructure on the impedance is also discussed.

Computational Investigation of Bi Containing Pyrochlores

Beverly Brooks-Hinojosa[1], Juan C. Nino[2] and Aravind Asthagiri[1]

[1]Chemical Engineering Department, University of Florida, Gainesville, FL 32611-6005
(E-mail: aasthagiri@che.ufl.edu)
[2]Materials Science and Engineering, University of Florida, Gainesville, FL

ABSTRACT

There is considerable interest in pyrochlore systems ($A_2B_2O_7$) for use in high-permittivity dielectrics, capacitors, and high-frequency filter applications. The properties of these materials can be tuned through substitutions on the A and B cation sites, resulting in an extensive parameter space. Better understanding of the role of the local atomic structure and dynamics on the macroscopic properties will enable rational design within the vast number of possibilities. Using density functional theory (DFT), quantum mechanical calculations were performed to examine several Bi-containing pyrochlores with the Fd-3m (No. 227) space group to determine the role of chemical substitutions on the local geometric and electronic structure. We considered six simple bismuth pyrochlores ($Bi_2B^{4+}{}_2O_7$ with B^{4+} = Ti, Ru, Rh, Ir, Os, and Pt) [1] and four pyrochlores with cation substitution selected based on availability of experimental IR and Raman spectroscopy ($Bi_{3/2}M^{2+}Nb_{3/2}O_7$ and $Bi_{3/2}M^{2+}Ta_{3/2}O_7$ with M^{2+} = Zn, Mg). We will present DFT results on the structural properties of the simple pyrochlores including equilibrium lattice constants, oxygen positional parameters, and atomic displacement patterns. For the pyrochlores with cation substitution, energetics related to cation ordering will be presented, as well as atomic displacement magnitudes and pathways. Where possible, our DFT results will be compared to available experimental studies to understand the role of the atomic substitutions on the material properties. We will also discuss our efforts to extend the length and time-scales for simulations of these systems. We have developed a shell model potential for $Bi_2Ti_2O_7$ based on fitting to extensive first-principles data. Molecular dynamics (MD) results for $Bi_2Ti_2O_7$ will be presented and compared to experimental IR and Raman spectra. In addition, pair distribution functions derived from the MD simulations will be used to understand the correlation and dynamics of atomic displacement in $Bi_2Ti_2O_7$. Preliminary efforts to reproduce the temperature phase behavior of $Bi_2Ti_2O_7$ will be also presented.

[1] B. Brooks-Hinojosa, J.C. Nino, and A. Asthagir, "A First-Principles Study of Cubic Bismuth Pyrochlores", Physical Review B, 75**,** 104123 (2008).

Lithium and Zinc Composite Ceramic Powders

Xinghua Xie

Anhui University of Science and Technology, Huainan, Anhui 232001, Republic of China
(E-mail: xxh1963@163.com)

ABSTRACT

The present situation of detonation synthesis and emulsion explosives both at home and abroad is summarized in this paper. To solve the problems in research for lithium ion batteries, we suggested that zinc and lithium oxides should be used as cathode materials for lithium ion batteries. So, we design special emulsion explosives, and synthesize zinc and lithium oxides from an emulsion explosive. It is concluded that nanoparticles of lithium zincate can be synthesized from the unconventional emulsion explosive. Unconventional emulsion explosives for synthesis of zinc and lithium oxides are designed firstly. Furthermore, we succeeded in synthesizing nano-powders of zinc and lithium oxides by explosion at the fist time in the final analysis. Zinc and lithium nanooxides are successfully collected and validated by XRD, FTIR, and TEM

A Numerical Simulation to Relate the Shot Peening Operation to the Induced Residual Stresses of 15-5PH Steel

Reza Jalili Saffar

Tehran Polytechnic/Amirkabir University, Ashrafi Esfehani HW., Tehran, Iran
(E-mail: hsnjll@yahoo.com)

ABSTRACT

This paper presents a computational modelling of the shot peening process, in which the finite element method (FEM) was employed to study the elastic-plastic dynamic process of shots impacting on a metallic target (15-5PH). The results demonstrated the capability of the method to capture realistic behaviour including the interaction between incoming shots and rebounding shots. In order to verify accuracy of simulation, results were compared with those obtained experimentally by X-ray diffraction analyses

Structural Stability of Hydrogen Storage Materials

Masahiko Katagiri[1], Hidehiro Onodera[1] and Hiroshi Ogawa[2]

[1]Computational Materials Science Center, National Institute for Materials Science, 1-2-1 Sengen, Tsukuba 305-0047, Japan (E-mail: katagiri.masahiko@nims.go.jp)
[2] Research Institute for Computational Sciences, National Institute of Advanced Industrial Science and Technology,1-1-1 Umezono, Tsukuba, Ibaraki 305-8568, Japan

ABSTRACT

The microscopic mechanism of Hydrogen-Induced Amorphization (HIA) in AB_2 C15 Laves phase compound is studied. We investigate the role of the size effect by static and molecular Dynamics (MD) methods using Lennard-Jones pair-wise potentials.

1 INTRODUCTION

Hydrogen-Induced Amorphization (HIA) is a phase transformation from crystalline to amorphous induced by hydrogenation. HIA is a potential method for preparing amorphous alloys since hydrogenation and dehydrogenation can be done easily and rapidly. In addition, HIA has a close relation with the structural change of hydrogen-storage alloys which determines their performance [1]. For effective materials design using HIA, it is important to understand the atomistic mechanism of this process. For this purpose, computer simulation is a powerful tool.

Aoki et al. [2] studied HIA of C15 Laves phase AB_2 compounds experimentally. They reported that the relative atomic size is the controlling factor of the occurrence of HIA. HIA does not occur when the ratio of the Goldschmidt radii of A and B atoms, R_A / R_B, is less than 1.37 (A = rare earth, B = Al). In this ratio, the internuclear distances between both AA and BB atoms contract compared to those in the pure crystals [2]. On the other hand, HIA occurs when the ratio is larger than 1.37 (A = rare earth, B = Fe, Co, Ni). In this ratio, the AA internuclear distance contracts and BB internuclear distance expands. Thus it is known that the size effect is essential. Our goal is to reveal the role of the size effect at the trigger of HIA [2-5].

2 METHOD

2.1 Model

YAl_2 and $CeNi_2$ were modeled. YAl_2 is a non-HIA material and $CeNi_2$ is a HIA material. We used pair-wise Lennard-Jones (L-J) 12-6 potential to reveal the size effect. For different species pairs, the geometric combination rule was used. As for hydrogen, only repulsion was taken into account [4]. By the analysis of the equation of state using our potential, it is known that *both the YY and AlAl internuclear distances contract in YAl_2, while CeCe internuclear distance contracts and NiNi internuclear distance expands in $CeNi_2$.* This corresponds to experimental results

reported by Aoki et al. [2]. The ratio R_Y/R_{Al} is 1.27 and R_{Ce}/R_{Ni} is 1.46 in our model. Details of the interatomic potentials are in a reference [2]. We compared non-hydrogenated systems under isotropic tensile load and hydrogenated systems at zero pressure.

2.2 Elastic Stability

We treat homogeneous systems which do not contain any surface or defect. The dynamical stability of homogeneous lattice can be discussed by elastic stability [6]. We calculated elastic constants C^{ijkl} by fluctuation formula [7] from microcanonical molecular dynamics data.

$$c^{ijkl} = -\frac{\Omega_0}{kT}\delta(P^{ij}P^{kl}) + \frac{2MkT}{\Omega_0}(\delta^{il}\delta^{jk} + \delta^{ik}\delta^{jl}) + \frac{1}{\Omega_0}\langle\sum_a\sum_{b(>a)}(\frac{u''-u'/r_{ab}}{r_{ab}^2})r_{ab}^i r_{ab}^j r_{ab}^k r_{ab}^l\rangle \quad (1)$$

Each term shows the pressure-fluctuation, kinetic and potential contributions, respectively. Ω_0 is the total volume, T the temperature, k the Boltzmann factor and M the number of metal atoms. The superscripts i, j, k and l are the Cartesian indices. P^{ij} is the pressure tensor, <> the ensemble average and $\delta(P^{ij}P^{kl})$ the ensemble fluctuation. Note that the summations are taken over the metal atoms excluding hydrogen. By using the elastic constants obtained here, we calculated the elastic stability criteria for cubic symmetry at external pressure P [6].

$$B = \frac{1}{3}(C_{11} + 2C_{12} + \quad (2)$$

$$G' = \frac{1}{2}(C_{11} - 2C_{12} - \quad (3)$$

$$G = 4(C_{44} - \quad (4)$$

Here, $P < 0$ for tension. All are finite and positive so that crystal lattice is elastically stable [6].

3 ELASTIC INSTABILITY BY ISOTROPIC TENSILE LOAD

Figures 1 shows the MD snapshots of *non-hydrogenated* YAl_2 and $CeNi_2$ caused by an isotropic tensile load. YAl_2 shows a kind of cleavage-like structural change by decohesion with maintaining the local lattice structure. On the other hand, $CeNi_2$ shows the amorphous-like structural change. By examining snapshots during the amorphization process it can be seen that the trigger of the amorphization is the movement of the expanded Ni atoms rather than the contracted Ce atoms, as also seen in the HIA modeled by the embedded-atom potential [3]. A discontinuous potential-energy decrease is observed [4]. It suggests that the structural change is a kind of mechanical melting and should be distinguishing from solid-liquid melting.

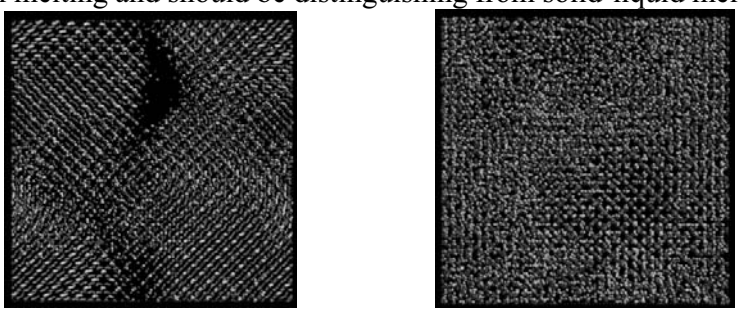

Figure 1: MD result of the cleavage-like structural change by isotropic tensile load for YAl_2 (left) and the amorphous-like structural change by isotropic tensile load for $CeNi_2$ (right).

4 ELASTIC INSTABILITY BY HYDROGENATION

We consider the elastic response of lattice to hydrogenation. Figures 2 shows the elastic stability by hydrogenation. In figures, x denotes bulk-modulus B-stability and + denotes the shear-modulus G'-stability. For comparison, B and G'-stabilities of non-hydrogenated systems under isotropic tensile load are also shown by ○ and □, respectively. In $CeNi_2$, B is reduced by hydrogenation (denoted by x), leading to a lattice instability: Unlike B, G' does not soften. The elastic constants C_{11} and C_{12} decrease with hydrogenation, but for G' which is the difference between C_{11} and C_{12}, the softenings are canceled. In YAl_2, we did not observe any evidence of such a softening effect. We found that hydrogenation and isotropic tensile loading gave similar elastic stability changes. This suggests that hydrogenation simply causes a volume expansion, and the softening due to the volume expansion is observed. On the other hand, the softening by hydrogenation in $CeNi_2$ is caused by negative increase of the fluctuation term. The softening in a simple volume expansion of $CeNi_2$ is caused by the decrease of the potential term in the elastic constant. Such a softening by volume expansion needs a large expansion to reach the elastic instability for amorphization. However, amorphization by hydrogenation occurs at a lower volume. The reason for the reduction in fluctuation term is that metal in the neighborhood of hydrogen deviate locally from their equilibrium positions. Even if such a relaxation is energetically small, the change in the pressure fluctuations is large.

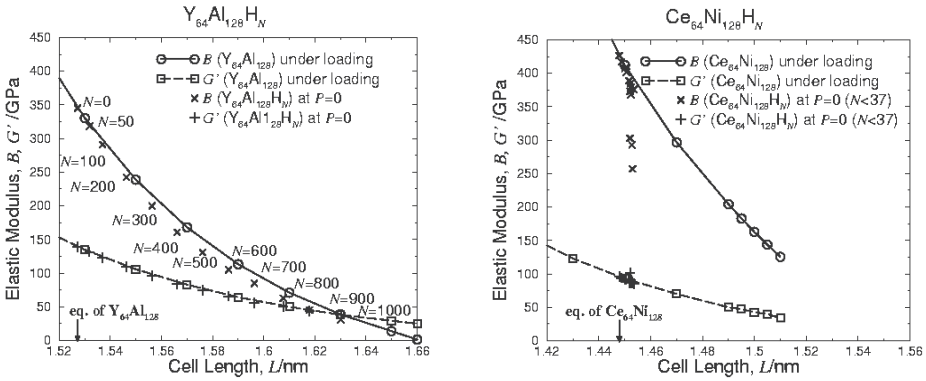

Figure 2: Elastic stability under isotropic tensile loading or by hydrogenation for YAl_2(left) and $CeNi_2$ (right).

5 CONCLUSIONS

Hydrogen-Induced Amorphization (HIA) was simulated by molecular dynamics (MD) methods. We compared non-HIA and HIA materials, YAl_2 and $CeNi_2$, respectively. The lattice fractured at the cell length where the bulk modulus falls to zero. In YAl_2, the bulk moduli of total lattice and sublattices fall to zero at a similar volume, and a cleavage surface is created. On the other hand, in $CeNi_2$, the bulk modulus of Ni sublattice is relatively small and falls to zero first. The amorphous-like structure is obtained. Such a difference in the mode of fracture is caused by the size effect. Compared to the pure states, Y and Al distances contract, while Ce distances contract and Ni distances expand in Laves phase. In $CeNi_2$, the bulk-modulus stability of Ni sublattice is low due to the expansion of the internuclear distances and falls to zero first. We incorporated hydrogen into the systems. YAl_2 did not show HIA. On the other hand, once the amount of

hydrogen atoms exceeds a critical value, $CeNi_2$ showed HIA [4]. In YAl_2, hydrogenation simply increases the volume and the bulk modulus is reduced because of the non-linearity of the interatomic potentials. A similar reduction is observed under an isotropic tensile load. The main cause of the reduction is the potential term in the elastic constant. On the other hand, in $CeNi_2$, hydrogenation greatly reduces the bulk modulus. This reduction is mainly caused by the negative increase of the pressure-fluctuation term in the elastic constant. As a result, hydrogenation leads to the amorphization at a much smaller volume than under a load. The increase of the pressure-fluctuation is the result of the atomic relaxation induced by hydrogenation. In $CeNi_2$, the contraction and expansion are realized simultaneously, and relaxation can occur by hydrogenation. Even if the potential-energy change resulting from the relaxation is small, the change in pressure fluctuation is high. These features can also be understood by the consideration of the equation of state for these compounds. When the size ratio exceeds 1.37, the bulk-modulus stability of the sublattice of B-atoms becomes low compared to that of A-atoms. However, there is no evidence that the ratio of 1.37 gives the critical ratio for HIA. The stability changes continuously as the ratio increases. This suggests that the mechanism of HIA cannot be understood by simple volume expansion and the atomic relaxations play an important role in it. When the internuclear distances of one sublattice expand and the other contract relative to pure crystals, relaxation occurs. It is concluded that the role of the size effect in HIA is to allow the atomic relaxation on hydrogenation and to facilitate the elastic instability by the increase of pressure fluctuations. It is necessary to consider the dynamical feature to understand the role of the atomic size ratio in the amorphization. Classical molecular dynamics gives a good example to reveal the role of the size effect from viewpoint of the parameter physics.

ACKNOWLEDGEMENT

This work has been supported by New Energy and Industrial Technology Development Organization (NEDO) under "Advanced Fundamental Research Project on Hydrogen Storage Materials.

REFERENCES

[1] K. Aoki and K. Masumoto, Materia Japan **34**, 126 (1995).
[2] K. Aoki, X. G. Li and T. Masumoto, Acta Metall. Mater. **40**, 1717 (1992).
[3] M. Katagiri and H. Onodera, Trans. MRS-J, **24**, 245 (1999).
[4] M. Katagiri and H. Onodera, Mater. Trans., JIM, **40**, 1274 (1999).
[5] M. Katagiri and H. Onodera, J. Phase Equilibria, **22**, 418 (2001).
[6] J. Wang, J. Li, S. Yip, S. Phillpot and D. Wolf, Phys. Rev. B, 52, 12627 (1995).
[7] J. R. Ray, M. C. Moody and A. Rahman, Phys. Rev. B, **32**, 733 (1985).

Multiscale Simulations Combined With Experimental Study of Barium/Strontium Ferrate/Cobaltate (BSCF) as a Promising Material For Solid Oxide Fuel Cell (SOFC)

Shruba Ganopadhyay,[1] Talgat Inerbaev,[1] Artëm E. Masunov,[1, 2,3] Deanna Altilio,[4] Nina Orlovskaya,[4] Jaruwan Mesit,[5] Ratan Guha,[5] Ahmed Sleiti,[4] Jayanta Kapat[4]

[1]Nanoscience Technology Center, [2]Department of Chemistry, [3]Department of Physics, [4]Department of Mechanical, Materials, and Aerospace Engineering; [5]School of Electrical Engineering and Computer Science, University of Central Florida, 12424 Research Parkway, Suite 400, Orlando, FL 32826; (E-mail: amasunov@mail.ucf.edu)

ABSTRACT

Mixed oxides of the general formula ABO_3 which crystallize in perovskite structures often have large mobility of the oxygen vacancies and exhibit strong ionic conductivityand used for several practical applications, including Solid Oxide Fuel Cells (SOFC). Barium/Strontium Ferrate/Cobaltate (BSCF) was recently identified as a promising candidate for cathode material in intermediate temperature SOFCs. We apply multiscale technique to determine its vacancy diffusion coefficient. At the small (atomic) scale Density Functional theory (DFT) is used to calculate activation energy barriers for oxygen migration in different local cation distribution. Activation barriers are used in Arrhenius equation to predict the rates for elementary steps in diffusion processes. These rates are then input into Kinetic Monte Carlo (KMC) at large (meso) scale simulations to obtain long time oxygen diffusivities and apparent activation energies. Since KMC method does not need energy evaluations, it is computationally inexpensive and allows treating millions of atoms explicitly. KMC approach can readily describe the macroscopic properties as a function of material morphology. In this contribution we report atomic scale study of BSCF electronic structure using plane wave pseudopotential DFT implemented in Quantum-ESPRESSO. We report cations are completely disordered, while oxygen vacancies exhibit a strong trend to from L-shaped trimers and tetramers, Löwdin population analysis of the spin density indicates that the cobalt cations shows Jahn-Teller distortion of octahedral coordination around Cobalt cations, both theoretically and experimentally and confirmed its intermediate spin state. We compute oxygen vacancy migration activation energy and find it to be in good agreement with experimental data.

1. Introduction

Defect chemistry and electronic structure of the cathode materials plays important role in electrical conductivity and ease of oxygen diffusion which is a key part of SOFC efficiency. In this study we employ plane wave density functional theory combined with Vanderbilt ultrasoft pseudopotentials in order to investigate the electronic structure of perfect BSCF, its oxygen vacant structure and the oxygen migration energetics in BSCF.

Our calculations are based on the DFT with the Perdew-Burke-Ernzerhof (PBE) exchange-correlation functional in the framework of Vanderbilt ultrasoft pseudopotentials [2] and plane wave basis set as it is implemented in Quantum-ESPRESSO program package [3]. The Brillouin-zone integrations were performed using Monkhorst-Pack grids using a 2×2×2 mesh for supercell calculations and 4×4×4 mesh for single unit. Spin polarized calculation with Marzari Vanderbilt smearing is used throughout. The geometry optimization was performed using Broyden-Fletcher-Goldfarb-Shanno algorithim. The wave function and electron density representation are limited by kinetic energies of 40 and 360 Rydberg respectively. We treated the Ba(5*s*,5*p*,*6s*), Sr(4*s*,4*p*,5*s*), Co(4*s*,3*d*), Fe(3*d*,4*s*) and O(2*s*,2*p*) electrons as valence states, while the remaining electrons were kept frozen as core states. For Co^{+4} we used low spin (LS), intermediate spin (IS) and high spin (HS) states (spin of S=1/2, S=3/2, and S=5/2); for Fe^{4+} cations LS and HS states (S=1 and S=2) were considered. The accuracy of pseudopotentials was validated by computing the equilibrium lattice parameters (a) are compared with experimental value and bulk moduli (B) is also compared with available experimental value.

2. Results and Discussion

Löwdin population analysis in BSCF supercell is presented in the Tab 1. It shows that the intermediate spin in Co and high spin states in Fe are most stable with Boltzmann factor 98%. After structural relaxation of BSCF supercell, we observed, tetragonal Jahn-Teller distorted Co (Fig. 1) since elongation and contraction both are observed in simultaneous fashion overall symmetry of the structure remains cubic, from the spin state configuration it can be inferred that the intermediate spin state only, can show the Jahn-Teller distortion. This theoretical evidence reinforced by Raman spectroscopic data (Fig. 2) where disappearance of peak with increase of temperature is observed.

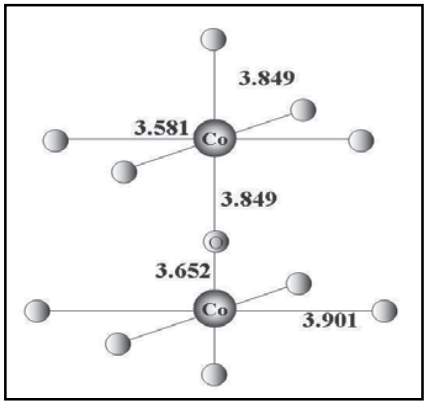

Figure 1. Jahn-Teller Distortion of the Co coordination sphere in BSCF

Table 1. Spin densitied on transition metal cations according to Lowdin population analysis for the different spin states of BSCF 2x2x2 superlattice, their relative energies and Boltzman factoirs

Multiplicity			Converted Lowdin polarization		ΔE kcal mol-^{1}	B factor (%)
Total	Fe^{+4} (d^4)	Co^{+4} (d^5)	Fe	Co		
23	2	3	3.61	2.59	9.66	2
27	4	3	3.62	3.12	0.00	98
35	2	5	4.31	4.16	35.23	0
39	4	5	4.6	4.58	101.37	0

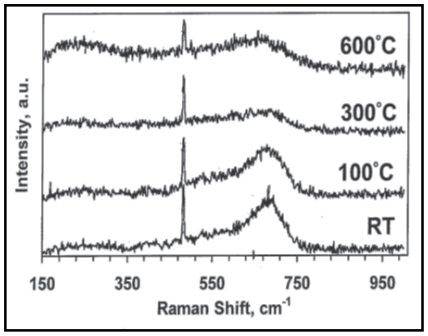

Figure 2. Raman Spectra of BSCF

For modeling the mixed perovskite $Ba_{0.5}Sr_{0.5}Fe_{0.2}Co_{0.8}O_3$ we used a 2×2×2 supercell [1]. One supercell has 4 Ba atoms, 4 Sr atoms, 2 Fe atoms and 6 Co atoms. For this structure all 9 possible symmetrically inequivalent arrangements of Fe^{4+} and Co^{4+} cations at the transition metal atoms positions as well as Ba/Sr ion positions were taken into consideration. All these structures and their relative stability are listed in Tab. 2. From the Boltzmann factor it is evident there is no preferred cation arrangement.

Table 2. Different cation distributions, their relative energies (ΔE) and Boltzman factors (B)

M	Fe		Ba				ΔE kcal mol^{-1}	B factor %
27	¼, ¼, ¼	¼, ¼, ¾	½, 0, 0	0, ½, 0	½, 0, ½	½, ½, ½	0.00	18
27	¼, ¼, ¼	¾, ¼, ¾	½, 0, 0	0, ½, 0	0,0, ½	½, ½, ½	0.10	18
27	¼, ¼, ¼	¾, ¾, ¾	½, 0, 0	0, ½, 0	0,0, ½	½, ½, ½	0.76	13
27	¼, ¼, ¼	¼, ¼, ¾	½, 0, 0	0, ½, 0	0,0, ½	½, 0, ½	1.42	10
27	¼, ¼, ¼	¾, ¼, ¾	½, 0, 0	0, ½, 0	0,0, ½	½, 0, ½	1.41	10

Next we calculate the relative stability of oxygen deficient supercell, with respect to different vacancy positions. From experiment [1], the molar fraction of oxygen vacancies at 1150°C is δ=0.38. Therefore we examined different structures with up to 4 oxygen vacancies per supercell. We removed one, two, three and four oxygen atoms from 2x2x2 supercell, which corresponds to stoichiometry of $Ba_{0.5}Sr_{0.5}Co_{0.8}Fe_{0.2}O_{3-\delta}$ (where δ = 0.125, 0.25, 0.375, 0.5). On the first step the simulation is performed for different ionic positions in stoichiometric (no defects) supercell (Tab. 2). On the second step we remove one oxygen atom from the most stable stoichiometric configuration and calculate relative energy of different multiplicities. The multiplicity with the lowest energy is used to optimize geometry of that particular configuration and Boltzmann factor is calculated to check the probability of the particular orientation. The same procedure is repeated for the oxygen vacant configurations. In order to determine the multiplicity of the stoichiometric supercell, one of two spin states for Fe^{4+} cation were combined with one of three spin states for Co^{+4}. As it is known from experiment the $SrFe_{1-x}Co_xO_3$ compound is antiferromagnetic for x<0.10-0.15 and becomes ferromagnetic for x≥0.2. Our calculations confirm these results [4].

We observe two vacancies in cis-position to the same Fe/Co ion (L-shape vacancy ordering) to be the most stable. This is in agreement with the experimental fact that the BSCF structure remains cubic in the observed oxygen deficiency range, while with similar compound with no Ba forms brownmillerite structure with linear vacancy ordering [5]. The relaxed geometry of BSCF with 2, 3, and 4 oxygen vacancies also changes the coordination of one, two, or four transition metal cations, adjacent to the vacancy, from ideal octahedron with two vertices missing to distorted tetrahedron (Fig 3).

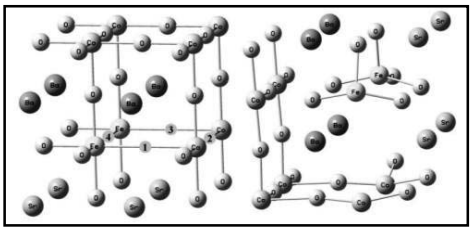

Figure 3. Four oxygen vacancies in BSCF

For activation energy calculation we use different distribution in supercell with one vacancy. We perform two structural relaxation calculations, one is for oxygen vacant cubic supercell, another one with oxygen ion in the middle of the XYX plane and angle OYZ is 45^0. Activation energies for different cation orientations are listed in Tab. 3. Our results are in good agreement with the

experimental value for activation energy of oxygen ion migration is c.a. 10.5 kcal/mol [1], except for one ion configuration, that has low Boltzman factor and is infrequent.

Table 3. Activation energies of different cation arrangement in BSCF supercell

Fe		Ba				Vacancy		ΔE kcal mol-1
¼, ¼, ¼	¾, ¾, ¾	½, 0, 0	0, ½, 0	0, 0, ½	½, ½, ½	½ ,¼, ¼	½, ¼, ¼	9.06
¼, ¼, ¼	¾, ¾, ¾	½, 0, 0	0, ½, 0	0, 0, ½	½, ½, ½	¼, ¾, ½	¼, ½, ¾	7.83
¼, ¼, ¼	¾, ¾, ¾	½, 0, 0	½, ½, 0	½, 0, ½	½, ½, ½	¼, ¾, ½	¼, ½, ¾	12.49
¼, ¾, ¼	¼, ¼ , ¾	0, ½, 0	½, ½, 0	0, 0, ½	½, 0, ½	¼, ¾, ½	¼, ½, ¾	4.83

3. Conclusion

The present study demonstrates how plane wave DFT calculation can be used successfully to predict the electronic structure and oxygen transport property of doped perovskite BSCF. Our calculations predict the intermediate spin state and Jahn-Teller distortion for cobalt ions, both in agreement with experiment. The preferential vacancy arrangement is predicted to be L-shaped (for trimer) and square (for tetramer vacancies). This is in contrast with linear vacancy arrangement and phase transition to brownmillerite type of structure for similar material containing no Ba ions. The activation energy of oxygen migration was found in the range of experimental data. The microscopic probabilities of oxygen migration, obtained in the present study will be used for the large scale simulation with kinetic Monte-Carlo method. This work is currently under way.

4. Acknowledgements

This work is supported, in part, by NASA SFTI grant to UCF. The authors are greateful to DOE NERSC, as well as I2lab and Institute for Simulation and Training (IST) at University of Central Florida and for the generous donation of computer time. TI is thankful to UCF NSTC and IST for additional support.

5. References

[1]. Z. P. Shao, and S. M. Haile "A high-performance cathode for the next generation of solid-oxide fuel cells." Nature, **431** 170 (2004)
[2]. D. Vanderbilt, “Soft Self-Consistent Pseudopotentials in a Generalized Eigenvalue Formalism." Physical Review B, **41**, 7892 (1990).
[3]. S. Baroni, *et al*. Quantum-ESPRESSO. Available at http://www.pwscf.org (2006).
[4]. I. R. Shein, K. I. Shein, et al. "Band structure and the magnetic and elastic properties of $SrFeO_3$ and $LaFeO_3$ perovskites." Physics of the Solid State, **47**: 2082 (2005).
[5]. S. J. McIntosh, F. Vente, et al. "Structure and oxygen stoichiometry of $SrCo_{0.8}Fe_{0.2}O_{3-\delta}$ and $Ba_{0.5}Sr_{0.5}Co_{0.8}Fe_{0.2}O_{3-\delta}$." Solid State Ionics, **177** 1737 (2006).

Electronic and Bonding Characteristics of (Ti,Mo)C

Tae-Eun Kim[1], Young-Su Lee[2], Woo-Sang Jung[2], Soon-Hyo Chung[2], Jae-Hyeok Shim[2], Jung-Hae Choi[1] and Seung-Cheol Lee[1]

[1] Korea Institute of Science and Technology, Seoul 136-791, Republic of Korea
[2]Materials Science and Technology Research Division, Korea Institute of Science and Technology, Seoul 136-791, Republic of Korea

ABSTRACT

Carbides or nitrides precipitates play an important role in strengthening of metals by blocking the movement of dislocations. It has been known that tensile strength of conventional high-strength low-alloy (HSLA) ferritic steel is ~600 MPa. Recently, an HSLA steel having much higher tensile strength of ~800MPa has been reported [1]. According to the study, nanometer-sized fine carbides whose diameter was approximately 3 nm were the main reason for the strengthening of the steels. They also reported that the highest tensile strength was obtained when the composition of Ti and Mo was approximately 1:1. However, mechanical and chemical properties of (Ti,Mo)C in ferrite matrix has not been known yet.

Understanding the mechanical and chemical characteristics of (Ti,Mo)C is essential to understand the stability and the strengthening mechanism. In order to understand those properties, the authors adopted first-principle calculation because experimental analysis is very limited. Using first principles calculation based on density functional theory, the authors attempted to understand the configuration of Ti and Mo in (Ti,Mo)C, effects of strain and tendency of segregation.

[1] Y. Funakawa, T. Shiozaki, K. Tomita, T. Yamamoto, and E. Maeda, “Development of High Strength Hot-rolled Sheet Steel Consisting of Ferrite and Nanometer-sized Carbides”, ISIJ International, **44,** 1945 (2004).

First Principles Study of Transition Metal Diatomics as the First Step in Multiscale Simulations of Carbon Nanotube Growth Process

Satyender Goel[†‡] and Artëm E. Masunov[†‡*]

† Nanoscience Technology Center, ‡ Department of Chemistry, * Department of Physics, University of Central Florida, 12424 Research parkway, Suite 400, Orlando, FL – 32826 (E-mail: amasunov@mail.ucf.edu)

ABSTRACT

Single wall carbon nanotubes (SWNT) are cylindrical molecules with unique properties that make them potentially useful in wide variety of applications, including nanoelectronics and photonics. However, these applications are feasible only if SWNTs have specific chirality. Much work remains to be done to gain control over selectivity of SWNT synthesis by chemical vapor deposition (CVD). One of the prime factors affecting the chirality of SWNT is the chemical nature and rate of carbon containing feed gas. Mechanistic kinetics study of CVD processes are gravely complicated by variety of the species involved and by the high temperatures of the reaction chamber. It is not probably feasible to extract the information on mechanism for SWNT synthesis from experimental data. The chemical origin of the reaction barriers and intermediates, however, could be analyzed using molecular simulations. High theory level can be used for di- and tri-atomic fragments, and generate parameters for bond order force field. In turn, force field simulations will be used to characterize intermediates and transition states, and calculate rate constants. Here we propose multiscale computer modeling of CVD process. Our approach is to extract the structure of the intermediates from molecular dynamics trajectories, conduct the transition state search, predict the free energy activation barriers and the rate constants, build the kinetic model of the growth process, and implement it in kinetic Monte Carlo algorithm to predict the optimal experimental conditions necessary to produce desired chirality of SWNT.

1. Introduction

Many potential applications have been proposed for carbon nanotubes, including conductive and high-strength composites; energy storage and energy conversion devices; sensors; field emission displays and radiation sources; hydrogen storage media; and nanometer-sized semiconductor devices, probes, and interconnects. Some of these applications are now realized in products. Others are demonstrated in early to advanced devices. One of the barriers for some applications of single-walled nanotubes is nanotube type (chirality).

There are successful attempts for selective synthesis of SWNT.[1] Lolli et. al. found that using a CoMo catalyst the (n,m) distribution of the SWNT product can be reproducibly altered by varying the reaction temperature, the gaseous feed, or the cluster surface morphology. Specifically, CO is compared with CH_4 as a feed over $CoMo/SiO_2$ catalysts, increasing the temperature results in increase in nanotube diameter, without a change in the chiral angle. By

contrast, by changing the support from SiO_2 to MgO, nanotubes with similar diameter but different chiral angles are obtained. Finally, keeping the same reaction conditions but varying the composition of the gaseous feed results in different (*n*,*m*) distribution. The clearly different distributions obtained when varying catalysts support and/or reaction conditions demonstrate that the (*n*,*m*) distribution is a result of differences in the growth kinetics, which in turn depends on the nanotube cap-metal cluster interaction.

The critical control parameters of individual carbon nanotubes are the nanotube diameter and chirality, while the packing density is important for nanotube arrays. There are presently many groups worldwide working to develop more efficient synthesis techniques for producing arrays of similar single-wall nanotubes, with a narrow diameter and chirality distribution, at a high production rate, and at a cheap cost. Further improvement is needed in synthesis capability and properties control for the single-wall nanotubes, by study of the growth conditions, such as temperature, pressure, and kinetics. Computer simulations are being actively employed to improve convergence of the experimental approaches. However, only a few examples are found in the literature that attempt to simulate the CNT growth.

Reactive empirical bond order (REBO) force field was employed to model the catalyzed growth of nanotubes by CVD and investigates nanotube stability as a function of nanotube type, length and diameter through molecular dynamics (MD) approach. The calculations show preferred type of nanotube change from SWNT to MWNT upon size increase.[2] Since REBO parameters are not available for metals, no catalyst nanoparticles were considered in this study.

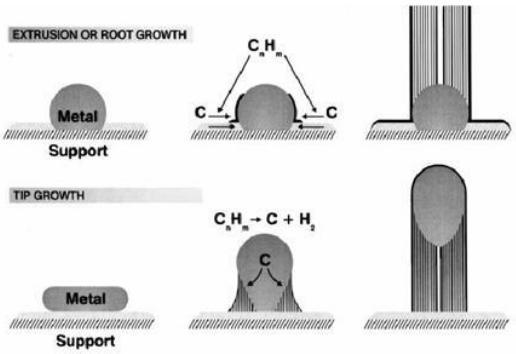

Figure 1: Visualization of a possible carbon nanotube growth mechanism

The only MD simulation of CNT/NP systems was done by using combination of Many body potentials for Fe-Fe, Brenner potential for precipitated atoms and Johnson potential for Fe-C interactions. The effect of iron cluster size on the structure defects and diameter of the SWNT

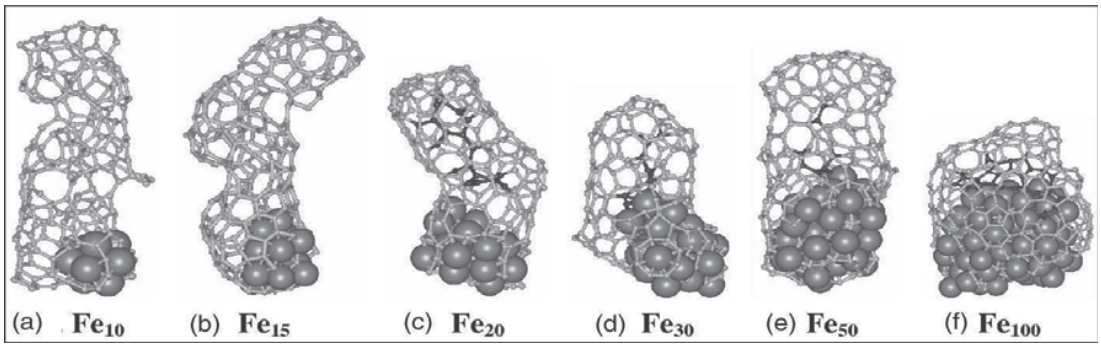

Figure 2: Dependence of the SWNT structure and diameter on cluster size. Panels (a) – (f) show typical structures that were obtained from clusters containing 10, 15, 20, 30, 50, and 100 Fe atoms, respectively. (adapted from Ref 3)

was reported.[3] Specifically, the study showed that for large particles, containing at least 20 Fe atoms, the caps grow in diameter until they have the same diameter as the cluster.

2. Project Goals

To fully control nanotube synthesis, one needs guidelines for optimizing the catalyst structure and experimental conditions. These guidelines are difficult to obtain without the detailed knowledge of the mechanism for SWNT catalytic synthesis. The studies done in past were insufficient to develop a comprehensive description of SWNT growth mechanism. Although nucleation of carbon polycyclic structures had been observed in *ab initio* MD simulations of carbon/metal nanoclusters, short simulation times did not allow nanotubes to form. Semiempirical MD simulations of SWNT growth did not include catalytic nanoparticle.[4] Force field simulations including catalyst had been published, but artificially fast growth rate resulted in formation of extremely defective nanotubes.[3] Therefore, it is of interest to simulate catalytic SWNT growth mechanisms directly. The chemical origin of the reaction barriers and intermediates needs to be analyzed using quantum chemical methods to determine the effect of catalyst structure on SWNT morphology.

Here we propose to use multiscale simulation approach. Hybrid DFT will be used for di- and tri-atomic fragments, and generate parameters for bond order force field. At short time scale, we will use molecular dynamics with REBO force field, implemented in code GULP to study SWNT growth. At the next step we will construct SWNT/nanocluster systems, perform geometry optimization for initial and final structures for different steps of SWNT growth. These structures will be used in MD simulations and additional reaction intermediates will be identified. All the intermediates found will be used in the gradient minimization search for transition states between intermediates and free energies for intermediates and transition states will be tabulated. By using the free energies of the intermediates the kinetic model for catalytic growth can be developed and implemented in Kinetic Monte-Carlo code. Kinetic Monte Carlo (KMC) is using goal function based on empirical rates[5] of each elementary step and is computationally efficient alternative to MD in describing dynamics of a large molecular system.

Finally, the resultant growth rates obtained from kinetic Monte-Carlo simulations will be obtained for SWNT of different chirality. The developed protocol will be used to study SWNT growth with different catalysts under different temperature and feed rate conditions. The specific combinations of these conditions optimized for maximum selectivity will be suggested for experimental verification.

3. Results and Discussion

We investigate bond energetics, electronic structures, dipole moments, and ionization potentials in gas-phase neutral hydrides, formed by *3d*-transition metals from Sc to Cu. Broken-symmetry approach was adapted in order to get the qualitatively correct description of the bond dissociation. BMK gives the

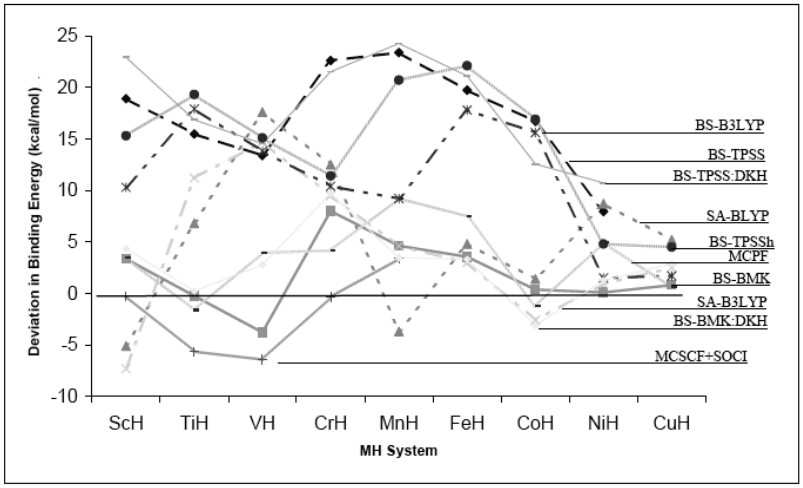

Figure 3: Deviations in Binding Energies from experimental data for neutral MH with various DFT and WFT methods.

best agreement with experiment, followed by two WFT methods. The other DFT methods range as follows. Among broken symmetry methods, the accuracy quickly deteriorates as the fraction of HF exchange decreases from BMK (42%) to B3LYP (20%) to TPSSh (10%) to TPSS (0%). Spin adapted (SA) formalism on the other hand, show only marginal improvement from pure BLYP to hybrid DFT (B3LYP). SA-B3LYP gives 80% lower rms value than BS-B3LYP but it is still twice less accurate than BS-BMK.

The individual values of deviations are plotted on Fig 3. One can see that BMK values are within 4 kcal/mol of experimental ones for almost all the systems (8 kcal/mol for CrH). Scalar relativistic correction does not improve the energies and deviations are similar to the one observed in non-relativistic BMK.

4. Conclusion

We report BMK dissociation energies that are in better agreement with experiment than those obtained with high level wavefunction theory methods, published previously. This agreement with experiment deteriorates quickly when the fraction of the Hartree-Fock exchange in DFT functional is decreased. This benchmark study can be used to analyse di- and tri-atomic fragments, and generate parameters for bond order force field.

5. Acknowledgements

This work is supported in part by UCF start up grant. SG gratefully acknowledges I2lab fellowship. The computer time was generously provided by DOE NERSC and UCF I2lab. The authors are grateful to Annie Wu and Lee Chow for many useful discussions.

6. References

[1] G. Lolli, et al., "Tailoring (n,m) structure of single-walled carbon nanotubes by modifying reaction conditions and the nature of the support of CoMo catalysts," Journal of Physical Chemistry B,**110**, 2108-2115, (2006).

[2] S. B. Sinnott, et al., "Model of carbon nanotube growth through chemical vapor deposition," Chemical Physics Letters,**315**, 25-30, (1999).

[3] F. Ding, et al., "Molecular dynamics study of the catalyst particle size dependence on carbon nanotube growth," Journal of Chemical Physics,**121**, 2775-2779, (2004).

[4] Y. Kumeda, et al., "Direct trajectory simulation on the growth of carbon nanotubes," Chemical Physics Letters,**360**, 149-154, (2002).

[5] A. Maiti, et al., "Theory of Carbon Nanotube Growth," Physical Review B,**52**, 14850-14858, (1995).

Modeling Boring Operation in Machining of Microalloyed and Heat-Treated Alloy Steels for Study of Machinability at Different Cutting Condition

Ali Ebrahimi, Sirous Jvadpour

Department of Materials Science and engineering, School of Engineering, Zand street, Shiraz, Fars -1681958111
(E-mails: aliebrahimii@yahoo.com, sirous_javadpour@yahoo.com)

ABSTRACT

This paper presents a finite element modeling for evaluation machinability of different alloy steels. This comparison was carried out between microalloyed steel (38MnVS5) and heat-treated alloy steels (AISI 1045 & AISI 5140) in boring operation at identical cutting condition. Orthogonal cutting experiments were used with FEM simulation of the cutting process. These data were used in modeling of boring with cutting tools where the cutting forces, tool stresses, and temperatures were predicted in the cutting edge. Since, heat generation and cutting force affect tool life, tool wear and quality of machined parts, thus modeling of these parameters in machining process can help to evaluation machinability of different materials and decrease the cost of machining. Therefore, study was carried out for evaluation machinability of microalloyed steel, and quenched-tempered steels in boring operation by simulation of process and comparison the results for these steels. Modeling results and experimental data showed that the machinability of microalloyed steel is better than heat-treated alloy steels in form of cutting forces and heat generation.

Electronic Structure and EFG Calculation of CeIn3 Under Pressure

Mansoure Ilkhani[1], Mohamad Reza Abolhassani, Saeid Jalali Asadabadi

[1]#191, Nabard_e_shomali, St., Piroozi Ave., Tehran, Iran
(E-mails: ilkhaniirn@yahoo.com, taher40@yahoo.com, sjalali@phys.ui.ac.ir)

ABSTRACT

Electric field gradients (EFG's) at In and Ce sites, electronic specific heat, spin magnetic moments at Ce site and bulk modulus were calculated for the case of CeIn3.The calculations were performed by increasing pressure gradually from -5 GPa to +22 GPa, within the density functional theory (DFT) using the augmented plane waves plus local orbital (APW+lo) method employing the so-called PBE-GGA+U and WC-GGA+U schemes. The results show almost a linear reduction of spin magnetic moments of Ce by increasing the pressure from -5 GPa to 22 GPa. However, one observes from these results that the calculated EFG's at the In site are growing up by the imposing the pressure. We have compared the EFG's at zero pressure with the theoretical and experimental results. This comparison shows that our EFG's are close to the results of the other groups and in good agreement with experiment results at ambient pressure. Our results show that Cerium f states move away from the Fermi level into the conduction band and cause the suppressing of the spin magnetic moments in the vicinity of some quantum critical point. The calculated bulk modules have good agreement with the experimental data. Key words: density functional calculations, electronic density of states, bulk modulus, electronic specific heat, electric field gradient